

**Final Report**

*entitled*

**Fracture Mechanics Assessment of the Nine Mile  
Point Unit 1 Shroud H4 Weld**

*Prepared for:*

**Niagara Mohawk Power Corporation  
300 Erie Boulevard West  
Syracuse, New York 13202**

*by:*

**MPM Research & Consulting  
P.O. Box 840, 915 Pike Street  
Lemont, PA 16851-0840**

**October, 1994**

©Copyright 1994 M.P. Manahan, Sr.  
All Rights Reserved

9411160244 941104  
PDR ADDCK 05000220  
P PDR



## Executive Summary

Niagara Mohawk Power Corporation (NMPC) submitted their response to the Nuclear Regulatory Commission (NRC) Generic Letter 94-03 on August 23, 1994 which contained analysis results pertinent to the issue of shroud cracking at Nine Mile Point Unit 1 (NMP-1). Subsequent to the NMPC submittal, GPU Nuclear Corporation (GPUNC) completed the Oyster Creek shroud inspection and found significant cracking on both the inner diameter (ID) and outer diameter (OD) surfaces of weld H4. The ID cracks were observed both on the top and bottom of the weld, but the OD cracks were only found on the bottom side of the weld. The weld H4 indications at Oyster Creek were the only significant indications found in any of the shroud welds which were inspected. As a result of these findings, and in light of the fact that the Oyster Creek reactor design is similar to that of NMP-1, the NRC has requested that NMPC submit a revised response to the Generic Letter 94-03.

In support of the preparation of a response to the NRC request, MPM Research & Consulting has performed a fracture mechanics assessment of the NMP-1 shroud H4 weld to determine whether or not throughwall cracking is expected before the end of cycle 11. This assessment included a finite element weld pass simulation to determine the residual stress distribution present after welding. Circumferential variations in the axial stresses were also estimated to account for differences in weld shrinkage due to, for example, weld starting and stopping, variations in weld groove width, and weld repairs. Calculations were also performed to determine the effects of ovality and postulated jacking to correct for out-of-round conditions during welding of the top and bottom cylinders at H4. The calculated stresses were used to determine the applied stress intensity ( $K_I$ ) which was compared to the threshold stress intensity factor ( $K_{ISCC}$ ) to see if crack initiation is expected. Since the result of these calculations showed that it is possible that crack initiation has occurred on the ID surface of the H4 weld, crack growth simulations were performed. There is no doubt that any cracks which initiate on the ID surface of weld H4 will arrest before propagating throughwall. For NMP-1, the depth of an ID initiated crack was estimated to be ~0.4 in.. This conclusion holds for conservatively postulated stresses and for conservative crack growth models. It is possible that localized flaw growth could exceed 0.4 in. if localized weld repair or other local stresses exceed those calculated in the model.

The applied  $K_I$  at the OD surface of NMP-1 weld H4 is ~4.7 ksi  $\sqrt{\text{in.}}$  for a postulated 0.010 in. flaw. The stress intensity at the surface is low because the welding procedure which was followed results in very low OD residual surface stresses. The weld passes for the double-J groove weld at H4 were completed at the ID first, followed by welding at the OD. The radial weld shrinkage during the final passes results in a substantial lowering of the OD surface stresses. Since a dye penetrant inspection was performed, the postulated 0.010 in. flaw is considered to be an upper bound. Although initiation is unlikely for the fabrication and operating stresses considered, it is possible that initiation could occur if localized stresses were induced, for example by a weld repair, or if a deeper flaw than has been postulated was not detected during construction. Accordingly, crack growth calculations for OD initiated cracks were also performed.



The OD initiated crack growth simulation showed small crack depths through the end of cycle 11 when only the weld residual and operating stresses were applied. However, there is a probability of localized throughwall cracking when the circumferential variation and out-of-round stresses are added to the welding residual and operating stresses. For the case where an elliptical surface crack with small surface length (L) to depth (a) ratio is used in the crack growth simulation ( $L/a=2$ ), the postulated OD flaw requires a full 11 fuel cycles to grow throughwall (assuming an arrested ID crack of 0.4 in. deep opposite the OD flaw). However, for an L/a ratio of 5, localized throughwall penetration results after about 35,000 hours of hot operation, thus allowing time for circumferential crack growth to occur. In order to characterize the effects of localized throughwall penetration, a model was developed to conservatively account for the circumferential crack propagation which would follow radial throughwall cracking. The model, which includes a 0.4 in. deep 360 degree ID crack, conservatively shows that 41% of the section would remain uncracked at the end of cycle 11.

Based on the shroud fabrication records, plant operating experience, and the fracture mechanics assessment of weld H4 reported herein, MPM Research & Consulting has concluded that there are adequate margins of safety through the end of cycle 11 to ensure continued safe operation at NMP-1.



. . . . .  
 . . . . .  
 . . . . .  
 . . . . .  
 . . . . .

. . . . .

.

.

.

.

## Table of Contents

Executive Summary .....	i
Table of Contents .....	iii
List of Figures .....	v
List of Tables .....	ix
<b>1.0 Introduction .....</b>	<b>1</b>
<b>2.0 Stress Field Characterization .....</b>	<b>2</b>
2.1 Welding Simulation .....	2
2.1.1 Axisymmetric Finite Element Model .....	3
2.1.2 Material Properties .....	4
2.1.3 Welding Procedure .....	4
2.1.4 Welding Heat Transfer Simulations .....	5
2.1.5 Welding Stress and Deformation Simulations .....	6
2.1.6 Sensitivity Studies .....	7
2.1.7 Welding Residual Stress Mechanisms .....	8
2.2 Operating Stresses .....	9
2.3 Non-Axisymmetric Weld Effects .....	9
2.3.1 The 3D Finite Element Model .....	10
2.3.2 Verification of the 3D Model .....	11
2.3.3 Solutions for Non-Axisymmetric Weld Shrinkage .....	11
2.3.4 Ovality Effects .....	12
2.4 Stress Intensity Factor Calculations .....	15
2.4.1 Method .....	15
2.4.2 Comparison of Finite Element Stress Intensity Factors to Handbook Values .....	17
2.4.3 Stress Intensity Factor Solutions for the H4 Weld at Operating Conditions .....	17
<b>3.0 Crack Initiation Analysis .....</b>	<b>46</b>
3.1 Threshold Stress Intensity Factor ( $K_{ISCC}$ ) .....	46
3.2 Comparison of Applied Stress Intensity ( $K_I$ ) to $K_{ISCC}$ .....	46



1. The first part of the document discusses the importance of maintaining accurate records of all transactions and activities. It emphasizes the need for transparency and accountability in all financial dealings.

2. The second part of the document outlines the various methods and techniques used to collect and analyze data. It provides a detailed overview of the research methodology and the tools used for data collection and analysis.



## Table of Contents (cont'd)

4.0	Fluence at H4 Weld .....	53
4.1	Fluence Characterization .....	53
4.2	Fluence Effects on Crack Behavior .....	53
5.0	Crack Growth Calculations .....	63
5.1	Plant-Specific Crack Growth Rate Model .....	63
5.2	Crack Growth Simulation at ID Surface of H4 .....	65
5.3	Comparison with Observation at Other BWRs .....	65
5.3.1	Characterization of the Oyster Creek and Brunswick Unit 2 Cracking .....	65
5.3.2	Fabrication History .....	66
5.3.3	Qualitative Interpretation of Oyster Creek OD Cracking .....	66
5.4	NMP-1 OD Crack Growth Calculations .....	68
5.5	NMP-1 Worst Case Cracking Behavior .....	68
6.0	Summary and Conclusions .....	90
7.0	References .....	93
8.0	Nomenclature .....	96

## Appendix

Appendix A	Example Isotherm Plots .....	98
------------	------------------------------	----



## List of Figures

### Section 2

2-1	The 2D Axisymmetric Finite Element Grid .....	24
2-2	The Assumed Weld Passes and Welding Sequence for the H4 Weld Simulation .....	25
2-3	The Deformed Shape of the H4 Weld Region Predicted by the WELD3 Simulation (Deformation Exaggerated by a Factor of 20) .....	26
2-4	The Predicted Welding Residual Stresses in the Heat Affected Zones of the H4 Weld at 70°F .....	27
2-5	Predicted and Measured Throughwall Welding Residual Stresses in a 26 inch Diameter Pipe With a 1.3 Inch Wall Thickness .....	28
2-6	Measured Throughwall Axial Welding Residual Stress Distributions From Various Pipes With Wall Thicknesses Greater Than One Inch .....	29
2-7	Predicted Axial Shrinkages for Weld H4 Both With and Without Use of the Artificial 3D Constraint Option of WELD3 .....	30
2-8	Predicted Welding Residual Stresses With Operating Loads and at an Operating Temperature of 550°F .....	31
2-9	Axial Stress Contours in the H4 Weld Region for Operating Conditions .....	32
2-10	Hoop Stress Contours in the H4 Weld Region for Operating Conditions .....	33
2-11	The 3D Finite Element Grid Used for the Axial Shrinkage Variation and Radial Mismatch (Ovality) Simulations .....	34
2-12	A Perspective Plot of the 3D Finite Element Grid Used for the Axial Shrinkage Variation and Radial Mismatch (Ovality) Simulations .....	35
2-13	Example Deformed Shape Plots Showing the Radial Displacements at the H4 Weld for Two Sinusoidal Axial Shrinkage Variations .....	36
2-14	Example Axial Stress Contour Plots at the H4 Weld for Two Sinusoidal Axial Shrinkage Variations .....	37



## List of Figures (cont'd)

2-15	Summary of the Axial Stresses Induced by Several Assumed Circumferential Variations in the Axial Weld Shrinkage at the H4 Weld .....	38
2-16	Example Deformed Shape Plots Showing the Radial Displacements Across the H4 Weld for Two Sinusoidal Radial Mismatch Variations .....	39
2-17	Example Axial Stress Contour Plots at the H4 Weld for Two Assumed Sinusoidal Radial Mismatch Variations .....	40
2-18	Summary of the Axial Stresses Induced by Several Assumed Circumferential Variations in the Initial Radial Mismatch at the H4 Weld .....	41
2-19	Illustration of the Accuracy That Can be Obtained Using the Finite Element Node Force Based Crack Closure Integral Method for Computing Stress Intensity Factors .....	42
2-20	Comparison of the Finite Element Stress Intensity Factor Solution for an Outer Surface Crack at the H4 Weld With Standard Handbook Type Solutions .....	43
2-21	The Stress Intensity Factor Solution for an OD Crack Growing in the H4 Weld HAZ With the Axisymmetric Welding Residual Stresses and Operating Conditions .....	44
2-22	The Stress Intensity Factor Solution for an ID Crack Growing in the H4 Weld HAZ With the Axisymmetric Welding Residual Stresses and Operating Conditions .....	45

### Section 3

3-1	Effect of Stress Intensity of Stress Corrosion Cracking (SCC) Velocity for Solution Annealed and Sensitized Type 304 SS in 22% NaCl Solution at 105°C .....	50
3-2	Load and ZRA Current Versus Time for Multiple Loading/Unloading Cycles to Various $K_I$ Levels .....	51
3-3	Comparison of Applied $K_I$ to $K_{ISCC} = 10 \text{ ksi} \sqrt{\text{in.}}$ for ID and OD of Weld H4 Assuming Upper Bound Stresses .....	52

1

2

3

4

5

6

7

8

9



## List of Figures (cont'd)

### Section 4

4-1	Nine Mile Point Unit 1 Internal Vessel Structures and Vessel Wall Geometry Used in Neutron Transport Calculation . . . . .	57
4-2	Oyster Creek Internal Vessel Structures and Vessel Wall Geometry Used in Neutron Transport Calculation . . . . .	58
4-3	Flux at Pressure Vessel Inner Wall Surface as a Function of Azimuthal Angle for Nine Mile Point Unit 1 and Oyster Creek . . . . .	59
4-4	Azimuthal Variation of Flux at NMP-1 Shroud Weld H4 . . . . .	60
4-5	Azimuthal Variation of Fluence at NMP-1 Shroud Weld H4 . . . . .	61
4-6	Dependence of IASCC on Fast Neutron Fluence for Creviced Control-Blade Sheath in High Conductivity BWRs and as Measured in Slow-Strain-Rate Tests at $3.7 \times 10^{-7}$ /s on Pre-Irradiated Type 304 SS in 288°C (550°F) Water . . . . .	62

### Section 5

5-1	Plot of NRC Crack Growth Rate Model and 304 SS Data . . . . .	77
5-2	Sensitized Type 304 SS in NMP-1 Recirculation Water Piping . . . . .	78
5-3	Observed vs. Theoretical Predicted Crack Growth Rates for Sensitized Stainless Steel Sensors . . . . .	79
5-4	Sensitized Type 304 SS in NMP-1 Core . . . . .	80
5-5	Location of the NMP-1 In-Core Stress Corrosion Monitor . . . . .	81
5-6	Electrochemical Corrosion Potential as a Function of Feedwater Hydrogen Concentration for NMP-1 . . . . .	82
5-7	Plant-Specific Crack Growth Rate Model for NMP-1 Weld H4 . . . . .	83
5-8	Schematic Representation of Peak Stress Field at ID Surface of Weld H4 . . . . .	84
5-9	Calculated Crack Length as a Function of Operating Time to the End of Cycle 11—Crack From ID Surface of Weld H4—Initial Flaw Size of 0.01 in. . . . .	85



List of Figures (cont'd)

5-10	Brunswick Unit 2 H4 Weld Cracking Map Showing Deepest Detected Flaws as a Function of Azimuthal Angle .....	86
5-11	Oyster Creek H4 Weld Circumferential Cracking Map Showing Deepest Detected Flaws as a Function of Azimuthal Angle .....	87
5-12	Welding Residual Stress Field (With Operating Loads) and Best Estimate Weld Variation and Out-of-Round Induced Stresses for Oyster Creek Crack OD Growth Analysis .....	88
5-13	Stress Distributions Used for NMP-1 Bounding OD Crack Growth Simulation .....	89



## List of Tables

### Section 2

2-1	Temperature Dependent Mechanical Properties for Type 304 SS Base Metal and Type 308 SS Weld Metal .....	19
2-2	Heat Transfer Material Properties for Stainless Steel Base and Weld Metals .....	20
2-3	Characterization of the Radial Mismatch Induced Axial Stress Distributions .....	21
2-4	Distances of Peak Stresses From the Inflection Point and Computed $\beta$ 's .....	22
2-5	Summary of HAZ Positions Relative to the Inflection Point and Estimated HAZ Stresses for a 0.5 in. Radial Mismatch .....	23

### Section 3

3-1	Weld H4 HAZ Surface Stresses .....	49
-----	------------------------------------	----

### Section 4

4-1	Flux and Fluence at the End of Cycle 11 at NMP-1 Shroud Weld H4 .....	55
4-2	Flux Distribution Through Shroud Weld H4 at Peak Flux Azimuthal Position .....	56

### Section 5

5-1	NMP-1 Recirculation Line Water Chemistry and Fluence .....	70
5-2	Crack Growth Rate as a Function of ECP for Nine Mile Point Unit 1 .....	71
5-3	Stress Intensity Factors for Crack Growth From the ID Surface of H4 .....	72
5-4	Comparison of Shroud Fabrication Details for NMP-1, Oyster Creek, and Brunswick Unit 2 .....	73
5-5	Crack Growth Simulation for Oyster Creek Weld H4 OD Cracking .....	74



List of Tables (cont'd)

5-6 NMP-1 Bounding Crack Growth Calculations ..... 75

5-7 Worst Case Cracking Behavior Summary ..... 76



## 1.0 Introduction

The Nuclear Regulatory Commission (NRC) issued Generic Letter 94-03 [NRC94] on July 25, 1994 and requested utilities to inspect core shrouds in their Boiling Water Reactor (BWR) plants no later than the next scheduled refueling outage and to perform an appropriate evaluation and/or repair based on the results from the inspection. The Generic Letter 94-03 also requested that plant owners perform a safety analysis supporting continued operation until the inspections are performed. Niagara Mohawk Power Corporation (NMPC) submitted their response to the Generic Letter 94-03 on August 23, 1994 [Te94] and concluded that based on the BWR Owners Group (BWROG) Shroud Cracking Generic Assessment and the results of the safety assessment for Nine Mile Point Unit 1 (NMP-1), continued operation of NMP-1 is justified until the inspection of the core shroud scheduled for the February, 1995 refueling outage.

Subsequent to the submission of the response to Generic Letter 94-03, the Oyster Creek shroud inspection was completed. No significant indications were found in any of the shroud welds which were inspected except for weld H4. Significant inner diameter (ID) and outer diameter (OD) cracking was found along the fusion line at weld H4. The ID cracks were observed both on the top and bottom of the weld, but the OD cracks were only seen on the bottom of the weld. As a result of the cracking observed at Oyster Creek, the NRC requested that NMPC perform additional analyses for the H4 weld at NMP-1 and that NMPC submit a revised response to the Generic Letter 94-03.

In response to the NRC's recent request, MPM Research & Consulting has performed a fracture mechanics assessment of the H4 weld at NMP-1. This assessment included a weld pass simulation to determine the stresses present in the H4 weld after fabrication. The P.F. Avery fabrication records provided detailed information on the weld design, materials, heat input, and welding procedure. As a result, an accurate representation of the weld residual stress field after welding, and during plant operation, could be obtained. In addition, estimates of the circumferential variation in stress due to differences in weld shrinkage were also calculated. Finally, the effects of ovality and jacking to correct for out-of-round conditions in the top and bottom cylinders prior to performing the H4 weld were calculated. The calculated stresses were used to determine the peak applied stress intensity ( $K_I$ ) which was compared to the stress corrosion cracking (SCC) threshold stress intensity factor ( $K_{ISCC}$ ). Since it was determined that ID crack initiation and growth is expected to occur, crack growth calculations were performed to determine the maximum extent of cracking. Finally, the model was applied in a qualitative manner to explain the observed cracking at Oyster Creek and Brunswick Unit 2.



## 2.0 Stress Field Characterization

This section describes the calculations for characterizing the stress fields that affect potential cracking in the sensitized heat affected zones (HAZs) of the H4 circumferential shroud weld known as H4. The H4 weld joins the type 304 stainless steel (SS) central upper and central mid cylinders using type 308 SS weld filler metal and the submerged arc process. At the time the H4 weld was made, both the upper and lower shroud assemblies were largely completed, making H4 the last major weld in the shroud fabrication process.

Since the applied loads for the shroud are quite small, the welding residual stresses are the most significant component of the stress fields that affect potential cracking in the H4 HAZs. The characterization of the welding residual stresses in this study was done using two types of simulations. The first type of simulation assumed axisymmetric behavior and used a two-dimensional (2D) elastic-plastic finite element model (FEM) to simulate the weld pass by weld pass weld metal deposition sequence. This simulation provided what is believed to be a very representative distribution of the welding induced residual stresses. However, in recognition of the fact that non-axisymmetric features of the welding process (starts and stops, weld repairs, and fit-up variations, etc.) may have resulted in some non-axisymmetric perturbation of the idealized axisymmetric fields, a three-dimensional (3D) linear elastic finite element model was used to determine the magnitudes and distributions of stresses associated with a series of non-axisymmetric weld shrinkage and fit-up assumptions.

## 2.1 Welding Simulation

The welding simulation methods that were used in this study were developed over the past sixteen years beginning with NRC and Electric Power Research Institute (EPRI) supported work at the Battelle Memorial Institute and then continuing through direct industry support through consultation and analysis services provided by Computational Mechanics, Inc.. Because welding simulation involves modeling complex material and geometric behaviors such as high temperature plasticity, annealing, and material deposition, welding simulation with common commercial finite element packages is difficult. As a result, the proprietary WELD3 [WEL3] software package was developed for doing welding simulations. Although using WELD3 software tends to simplify the process of doing welding simulations, there is more to welding simulation than using the correct software. Studies have shown that simplifications that are sometimes used by novice weld simulators lead to unrealistic residual stress predictions. Perhaps the most common and probably the worst mistake that one can make is to try to simulate a weld with numerous layers of weld passes as if all of the weld metal is deposited at one time. This type of so-called weld simulation leads to totally unrealistic residual stress magnitudes and distributions. Welding induces stresses through several simple mechanisms. If a welding simulation is approached as a means to understanding how these mechanisms interact in a given weld geometry, for a given welding sequence, and for a given set of welding parameters; and due attention is given to studying the effects of assumptions made in the modeling process, then there is no more reason for a welding simulation to provide misleading predictions than any other finite element simulation.



The circumferential nature of the H4 weld makes it natural to assume that the welding induced residual stresses will be axisymmetric and that the welding process can be simulated using a 2D axisymmetric model. Previous work has shown that using an axisymmetric model provides reasonable residual stress predictions in pipe girth butt welds for various sizes of pipes and sizes of welds [WELV]. There is no reason to believe that the assumption of axisymmetry is any less representative for the shroud geometry. In fact, the larger size of the shroud tends to make the axisymmetric assumption even more appropriate since the size of the weld induced thermal transients are smaller compared to other dimensions of the geometry.

Although stresses from axisymmetric simulations tend to be representative of actual component stresses, the differences between an axisymmetric weld simulation and the actual 3D welding process leads to the axisymmetric model generally predicting smaller shrinkages than actually occur. The basic reason is that in the axisymmetric model, the entire circumference of the model is essentially being welded simultaneously. The relative size of the hot region in the axisymmetric model is therefore much larger than in the actual case. This leads to the model thermally expanding during the time that heat is being input to the model to a larger extent than occurs in the real 3D geometry. In the real 3D geometry, cool material surrounds the weld region and therefore the initial thermal expansion of the weld region is largely restrained. The contraction behavior during cooling is reasonably well represented by the axisymmetric model because temperature gradients in the circumferential direction for the cooling material tend to be small compared to gradients in the radial and axial directions. However, since the thermal contraction is starting from a more thermally expanded geometry than in the real 3D case, the predicted net welding induced shrinkage is less than in the actual 3D geometry. Since the cooling process is mostly responsible for the creation of the residual stresses and is well represented by the axisymmetric model, the welding residual stresses from the axisymmetric simulations are generally good approximations to those in the 3D geometry.

WELD3 incorporates a special option for exploring the effect that the axisymmetric assumption may have on the predicted shrinkages and stresses. The option attempts to introduce artificial 3D constraint on the weld region during the times when it is increasing in temperature. Past experience with the use of this option shows that it has a much more pronounced effect on predicted displacements and shrinkages than on predicted stresses [WELV]. The effect on the shrinkage predictions is geometry dependent. When the weld is on a relatively thin component that requires only a few weld passes, the predicted shrinkages can be nearly doubled by using this option. For thicker sections requiring more passes, the effect is generally less. This is because even in the axisymmetric model, the cooler material tends to restrain thermal expansion of the weld region and therefore the axisymmetric model tends to be a better approximation for simulating welds in thicker sections.

### 2.1.1 Axisymmetric Finite Element Model

Since only the stresses in the H4 weld region were of interest, only portions of the upper shroud assembly and the central mid cylinder within about  $3\sqrt{R/t}$  were included in the axisymmetric model of the H4 weld. The 2D axisymmetric finite element grid is shown in Figure 2-1. The radial offset above the H4 weld is the central ring. This grid has 1463 nodes and 1292 four-noded isoparametric elements. The grid contains two sections for simulating the growth of cracks. These sections follow the weld HAZs above and below the weld. At these



sections two sets of nodes are defined. One set is attached to the elements below the section and the other set is attached to the elements above the section. When no crack is being modeled, the corresponding nodes are coupled using coupling elements. When a crack is to be simulated (used to calculate stress intensity factors for the computed stresses), one or more of these coupling elements are deactivated.

### 2.1.2 Material Properties

The shroud base metal is type 304 SS. The weld metal is type 308 SS. The material properties used in this study are summarized in Tables 2-1 and 2-2. Table 2-1 summarizes the elastic and elastic-plastic mechanical properties. These properties are used as functions of temperature in the finite element simulations. The properties for type 304 SS were taken from Reference [Int] except for the coefficient of thermal expansion which was taken from Reference [Aero]. The properties at the higher temperatures of these tables are often not reported and must be estimated. The elastic and plastic moduli at 2100°F reflect the fact that the material cannot sustain much stress at temperatures in this range and are not based on measured values. The material properties for these very high temperatures are not critical to the calculation of residual stresses at temperatures of practical interest because the yield stress, and hence the stresses, are very low at these high temperatures.

The material properties used for the type 308 SS weld metal are assumed to be the same as for the type 304 SS base metal except for the yield stress. The yield stress of the weld metal is assumed to be 1.25 times the yield stress of the base metal. Although it is generally believed that the type 308 SS yield stress is above that of type 304 SS, yield stress data tends to be very inconsistent. The factor of 1.25 is believed to be a reasonable estimate and is not expected to have a large effect on the axial residual stresses in the HAZ. The coefficients of thermal expansion (CTE) for the two materials appear to be different in these tables. The difference, however, is in the reference temperature. Since the weld metal initially starts in a molten state, a reference temperature of 2100°F is used instead of 70°F. Both tables reflect the same material behavior. The heat transfer analysis used in this study was based on an analytical solution for moving point heat sources. This solution does not permit temperature dependent properties to be used. The properties in Table 2-2 therefore represent average heat transfer properties over the range of temperatures experienced during welding.

### 2.1.3 Welding Procedure

The weld procedure for H4 was reasonably well documented in the P. F. Avery weld procedure sketches and welder records attached to [GE771]. The weld was a submerged arc weld. The weld groove was a symmetric (equal depth from inner and outer surfaces) double J type. The sides of the grooves were 22.5 degrees and both root regions had a 0.25 in. radius. A minimum preheat temperature of 60°F and a maximum interpass temperature of 350°F was specified. Welding was done in the "flat" position. The specified welding parameters were as follows:

<u>Pass no.</u>	<u>Amps</u>	<u>Volts</u>	<u>Travel</u>	<u>Filler Dia.</u>
1-12	240-325	25-31	10-20 ipm	5/64"
BALANCE	475-550	28-32	16-20 ipm	5/32"



11

12

13



14

15

16



Although the welding sequence was not specified, the actual sequence could be discerned from the welder records. Passes 1-6 were root pass welds done at the inner surface. Passes 7-12 were root pass welds done at the outer surface. Weld pass 7, however, did not immediately follow weld pass 6. Instead, the entire inner weld groove was filled before back chipping and welding the outer surface root passes. There is no record of the number of passes required to finish the inner and outer surface welds after the root passes were completed.

#### 2.1.4 Welding Heat Transfer Simulations

The WELD3 module called PLTTMP was used to perform the heat transfer calculations. PLTTMP provides the finite element temperatures used in the thermal elastic-plastic stress calculations. PLTTMP uses an analytical solution to the problem of a constant velocity point heat source in a plate. In this model, the surfaces of the plate are treated as insulated. The PLTTMP calculations use the temperature independent conductivity and heat capacity values given in Table 2-2.

The mid range values of the specified weld parameter ranges were used in the weld pass thermal simulation. This resulted in a heat input rate of 32 kJ/in for the root passes and a heat input rate of 51 kJ/in for the fill passes. Since the analytical thermal model simulates the actual movement of the arc, and since the material properties were input in terms of BTU's and seconds these heat input rates were converted to

<u>Pass</u>	<u>Heat Input (BTU/sec)</u>	<u>Travel (ips)</u>
root passes	7.5	0.25
fill passes	14.6	0.30

The submerged arc weld process is a very efficient process in the sense that nearly 100% of the electrical input energy gets into the weld as heat. A 100% efficiency was therefore assumed in this simulation.

Since the number of passes actually used to fill the weld grooves was not provided in the available H4 documentation, PLTTMP was used to determine the minimum number of passes that could be reasonably used in the simulation for the heat input rates resulting from the mid range welding parameters. Since previous experience has shown that combining passes of a weld layer into one modeled pass provides reasonable stress predictions, and since there was no way to know the order in which passes of a weld layer were actually deposited, the procedure was to model passes as though they extended across the entire weld groove width. PLTTMP allows heat input to be spread over an entire weld layer by dividing the total heat input among several point sources distributed across the weld groove.

With the heat input rates and travel speeds that were specified, it was found that each weld groove could be reasonably simulated as being completed with four weld passes. This was based on the fact that with this assumption the predicted temperatures for each pass results in the new pass material starting at a temperature that is well above the temperature at which the material can bear substantial stress. If more passes were simulated, these high heat inputs would cause substantial portions of the previous pass to be heated to the temperature range in which stresses are totally relieved. This would not be expected to lead to substantially different residual



1. The first part of the document discusses the importance of maintaining accurate records of all transactions and activities. It emphasizes the need for transparency and accountability in financial reporting.

2. The second part of the document outlines the various methods and techniques used to collect and analyze data. It includes a detailed description of the experimental procedures and the statistical tools employed.

3. The third part of the document presents the results of the study, showing the trends and patterns observed in the data. It includes several tables and graphs to illustrate the findings.

4. The fourth part of the document discusses the implications of the study and the conclusions drawn from the results. It highlights the significance of the findings and their potential applications.

5. The fifth part of the document provides a summary of the key points and a final conclusion. It reiterates the main findings and the overall objectives of the study.



stress predictions from those obtained using four passes on each side. However, weld shrinkages tend to be more affected by the number of weld passes than the stresses, and therefore predicted weld shrinkages could be smaller than actual shrinkages to the extent that the model used fewer passes than were actually applied. Figure 2-2 shows the manner in which the finite elements in the weld region were divided into a total of eight weld passes. The numbers indicate the order in which the weld passes were deposited in the simulation.

A temperature history for each finite element of the axisymmetric model for each weld pass deposition was computed by PLTTMP. In this analysis, an initial temperature of 70°F was assumed and it was assumed that the weld region cools to 70°F before the next weld is deposited. There is nothing in the weld documentation that provides any information on these initial and interpass temperatures other than the minimum and maximum values of 60°F and 350°F. The results of this study are not believed to be sensitive to any reasonable variations from these assumed values.

The temperature history for each finite element is approximated in a piece-wise linear way by computing temperatures at specific times using PLTTMP and then allowing the WELD3 elastic-plastic stress calculation module (STRESS2D) to linearly interpolate between these distributions for any other times that temperatures may be required. In this study, the temperature history for each pass was defined in terms of temperatures at five times. The first time was 1.5 seconds after the arc passes. The second, third, and fourth times were for when the new weld pass cooled to 1500°F, 1000°F, and 500°F. The final time was for when the entire weld region cooled to 70°F. Appendix A contains a number of temperature contour plots (isotherms) which illustrate these five temperature distributions. The distributions are referred to by the pass number plus one of the letters A, B, C, D, or E. Distribution 3A is the distribution for pass 3 at 1.5 seconds. Distribution 3C is the pass 3 distribution when the weld has cooled to 1000°F, etc.

### 2.1.5 Welding Stress and Deformation Simulations

Having the finite element temperature histories defined by PLTTMP, the elastic-plastic finite element calculation for the welding simulation was done. The WELD3 module for this step in the analysis is STRESS2D. The temperature dependent properties of Table 2-1 are used in the STRESS2D calculations.

The final deformed shape predicted by the welding simulation is shown in Figure 2-3. It can be seen that axial shrinkage is predicted as well as radial shrinkage. It can also be seen that the model is sufficiently long that the deformations at the ends of the model are a pure axial shrinkage. It can be seen from this deformed shape plot that the central ring is within the region of influence of the weld. The axial and hoop stresses in the weld region were found to be almost perfectly symmetric with respect to the weld centerline. That is, the welding residual stresses in the top HAZ are essentially identical to those in the lower HAZ. Although it was anticipated that these stresses would be very similar, it was expected that the central ring would induce more nonsymmetry than it did.

Figure 2-4 shows the predicted weld induced axial and hoop residual stresses in the HAZs of the H4 weld at 70°F. The stresses are plotted as a function of distance from the inner shroud



*[Faint, illegible text scattered across the page, possibly bleed-through from the reverse side.]*



surface. The distance is the radial distance and is not measured along the 22.5 degree path of the HAZ. The inside shroud surface is at the left side of the plots and the outside is at the right side. Since it is the axial stress component that would drive circumferential cracks in the HAZ, these are the stresses of most interest. The hoop stresses are shown for completeness. From Figure 2-4 it can be seen that the hoop stresses are tensile at all points through the thickness with the outer surface being at the tensile yield stress level of the weld material.

The axial stresses of Figure 2-4 show several interesting behaviors. First, the axial stresses at the outer surface are substantially below the yield level that might be expected for the material in the last pass. Second, although the outer surface is not strongly tensile, there are significantly tensile axial stresses just below the outer surface. Third, although the inner half of the wall thickness tends to be in strong compression, the inner surface has significantly tensile axial stresses. The reasons (i.e., mechanisms) behind this axial stress behavior can be discerned from the simulation and will be discussed below.

The distribution of axial residual stress seen in Figure 2-4 is similar to the distributions that have been measured and predicted by welding simulations for large diameter pipes with wall thicknesses greater than one inch [EP1743]. Figure 2-5, taken from [EP1743], shows both residual stress data and the results of a weld simulation for a 26 inch pipe with a 1.3 inch wall thickness. The axial stresses from the simulations are in good agreement with the data, and both show a through wall distribution that is very similar to that predicted for the shroud H4 weld in this study. It can be seen that the hoop or circumferential stresses are at tensile yield in the pipe but that they are not tensile at all points through the wall. This points out the fact that while the axial residual stresses for the two geometries are similar, the large difference in the radius to thickness ratio ( $R/t$ ) does lead to differences in behavior. It is also worth noting here that the pipe weld was a single sided weld and that while welding a 26 inch pipe from the inside would probably not be a reasonable approach, there is no inherent reason why the shroud weld could not be welded first on the outside and then finished by welding the inside. Reversing the weld sequence in the shroud would be expected to result in a much different axial distribution from that obtained above.

The data of Figure 2-5 represents two pipes. Similar data has been obtained and compiled for other pipes and has been presented in Appendix A of [NUREG0313]. Figure 2-6 is a reproduction of Figure 3 from this appendix. It can be seen that the data show a trend that is very similar to that of the axial stress predictions for the H4 weld.

#### 2.1.6 Sensitivity Studies

It was described previously that the WELD3 software offers an option which is intended to introduce into the axisymmetric model some of the constraint that would be operative in the real 3D geometry. Since this constraint is introduced without actually introducing restraining forces in the model, this constraint is referred to as artificial 3D constraint. Comparing the solutions in Figure 2-4, it can be seen that the effect on stresses of including the artificial constraint is not large. However, since the stresses from the analysis with constraint were judged to be more severe in terms of crack growth behavior, they were selected for use in all subsequent analyses.



•(•)•

Figure 2-7 shows the axial shrinkage behavior from the welding simulation. Each point on the curves corresponds to one of the five times used in computing the finite element temperature histories. One curve is from the solution without artificial 3D constraint and the other is from the solution with artificial constraint. It can be seen that the addition of the constraint increases the level of shrinkage by 68%. Although the added constraint reduces the expansion during the initial heating phase of each pass, it can be seen that there is still substantial expansion. If all of the positive expansion increments are subtracted from the final 0.06 in. predicted shrinkage, the result would be a shrinkage of about 0.12 inches. This should be an upper bound on the possible effect of 3D constraint (for the assumed eight pass weld). The predicted shrinkage of 0.06 inches is about 7% of the initial weld groove width. A 0.12 inch shrinkage would be 14% of the initial groove width.

The welding simulation was repeated wherein the number of times used for the piece-wise linear temperature history was increased from five to seven. The HAZ stresses were essentially unaffected by this change. The number of increments used in the welding simulation was decreased from 480 to 240 in another simulation. The HAZ results were again essentially unaffected although the hoop stress distributions in the region of the last pass were not as smooth as those shown in Figure 2-4.

#### 2.1.7 Welding Residual Stress Mechanisms

Probably the most interesting aspect of the predicted axial residual stress distribution shown in Figure 2-4 is the tendency for low stresses at the outer surface. The two fundamental driving forces for welding residual stress and deformation are shrinkage and shrinkage. The first shrinkage is the shrinkage parallel to the welding direction (circumferential) and the second shrinkage is shrinkage transverse to the welding direction (axial). In axisymmetric geometries the circumferential shrinkage gives rise to yet a third shrinkage and that is radial shrinkage.

The transverse shrinkage gives rise to axial stresses if the wall thickness is large enough that significant through wall temperature gradients can exist. This is clearly the case for the shroud. The transverse shrinkage tends to result in tension in the newly deposited material and compression in the material beneath the newly deposited material. Basically the hotter material wants to shrink but cannot shrink as much as it would like because the cooler material does not want to shrink. This puts the hotter material in tension and the cooler material in compression. Unless there is a some external restraint, the axial tension at the section must balance the axial compression. This basically explains the tendency for axial compression over the inner half wall thickness at H4 and the tendency for axial tension over the outer half wall thickness.

The large yield level hoop stresses in the most recently deposited pass can be thought of as a band being shrunk onto the shroud at the weld region. This band causes an inward deflection of the wall at the band (i.e., weld). This inward deflection induces bending in the wall which affects the axial stresses in the weld region. This bending that is induced during weld cooling tends to induce tensile axial stresses at the ID and compressive axial stresses at the OD. This behavior, when combined with the above transverse shrinkage behavior, therefore explains not only the reduced tension levels at the OD but also the large tension stresses at the ID.



It is perhaps worth adding that axial shrinkage can also contribute to the creation of the bending type of deformation in the weld region that leads to increased ID tension and reduced OD tension. This bending results from the axial shrinkage behavior not being symmetric with respect to the mid wall. The nonsymmetry results from the hotter outer surface wanting to contract in the axial direction more than the cooler inner surface.

## 2.2 Operating Stresses

Operating conditions for the H4 region consist of a 6 psi outward pressure, an upward axial force due to the same 6 psi pressure acting on the shroud head, and a downward axial force due to the deadweight of the upper portion of the shroud. The 6 psi head load results in a net upward force of 163 kips. The deadweight load is downward with a magnitude of 130 kips. The net force is therefore 33 kips upward. This force results in a net axial stress in the section above the central ring of 37 psi tension. The 6 psi outward pressure induces hoop stresses in the wall of about 350 psi. It can be seen therefore that the stresses due to the mechanical loads are quite small.

The most significant aspect of applying the operating conditions is the increase in temperature to 550°F. Although this temperature change induces no stresses due to differential thermal expansion, the decrease in yield stress does impact the predicted residual stresses. This is illustrated in Figure 2-8. The largest change in stress is seen in the hoop stresses at the outer side of the weld. This is expected since this is the stress component that was causing most of the plastic behavior during the final stages of weld cooling. Although the axial stresses at 70°F were already at or below the uniaxial yield at 550°F, the axial stress magnitudes are also reduced by the heating to 550°F. This is believed to be primarily a Poisson ratio type effect driven by the hoop stress reduction.

Figures 2-9 and 2-10 contain contour plots of the axial and hoop stresses at operating conditions. These plots allow stresses at locations other than the HAZ to be examined. It can be seen from the axial stress contours that the through thickness HAZ stress plots that have been presented to this point would not change substantially by selecting a slightly different section through the HAZ. The locations that would be most affected by a shift would be the surface points. At the inner surface, a shift to the weld fusion line would tend to increase the inner surface stress. At the outer surface, shifting to the weld fusion line would decrease the surface stress.

Although the stress information from Figure 2-8 was used as the basis for subsequent cracking studies, the element stresses of this plot were conservatively extrapolated to the inner surface so that a surface stress of 24 ksi was assumed. This is consistent with the peak HAZ value from Figure 2-9. At the outer surface, extrapolation would have resulted in a stress reduction, and therefore, it was conservative to not use an extrapolated value.

## 2.3 Non-Axisymmetric Weld Effects

The residual stresses predicted by the axisymmetric welding simulation are believed to be reasonable approximations of the average stress behavior for the H4 shroud weld. The



100

100

100

100

100



axisymmetric model cannot, however, account for 3D effects such as weld starting and stopping, localized weld repair operations, changes in welding parameters, or circumferential variations in the weld groove fit-up. The axial stresses from the axisymmetric model result in a net zero axial force across the weld HAZ at all points on the circumference. In the real 3D structure, the net axial force across the entire circumferential weld must be zero, but at any given location on the circumference it is possible that the average axial stress may not be zero. Equilibrium only requires that every location with net axial tension be offset by some location having net axial compression.

The actual 3D residual stress state may be thought of as the axisymmetric stresses from the 2D axisymmetric simulation plus some non-axisymmetric stress field representing the variations from the axisymmetric baseline field. The purpose of the analyses of this section was to estimate the magnitudes and distributions of stresses that one might expect for the non-axisymmetric component of the stress field.

Two types of non-axisymmetric effects were considered in this study. The first effect is based on the assumption that the transverse weld shrinkage (i.e., axial weld shrinkage) will not be the same at all points around the circumference. The second effect is based on the assumption that the top and bottom portions of the shroud did not match perfectly at the H4 weld joint and therefore required some form of fixturing to align the joint prior to welding. The first effect is referred to as a non-axisymmetric axial shrinkage effect and the second is referred to as an ovality effect or a radial mismatch effect.

Since little if any data on actual axial shrinkage variations or pre-weld radial mismatch was available, it was necessary to assume both the magnitude and the distribution of the assumed axial shrinkage and radial mismatch variations. To keep the analysis as simple as possible, the circumferential variations were modeled as being sinusoidal. The results are expected to be useful for assessing the effects of less regular variations. Since the analyses of this study on 3D effects assumed linear elastic material behavior, the results are scalable.

Since it was clear that the stresses from these circumferential variations would depend on the frequency of the assumed circumferential variations, a series of analyses were performed. The lowest frequency resulted in two complete cycles of variation around the circumference. For the axial shrinkage case this means that a net tension exists at 0 and 180 degrees and a net compression exists at 90 and 270. For the radial mismatch case, the two cycle case corresponds to both upper and lower H4 weld prep regions being elliptical before welding and the major axis of the top being aligned with the minor axis of the bottom. The case of one cycle is of no interest in either case because this results in only a relative rigid body rotation (axial shrinkage case) or displacement (radial mismatch case) between the upper and lower portions of the shroud and therefore would not create stresses at the weld. Three cases were considered in addition to the two cycle case. These cases considered four, eight, and sixteen complete cycles of axial shrinkage variation or radial mismatch variation around the circumference.

### 2.3.1 The 3D Finite Element Model

The 3D finite element grid used in this study is a 45 degree sector of the total shroud assembly. The cross section of the finite element grid is shown in Figure 2-11 along with the



basic shroud dimensions. The grid consists of 3792 eight-noded isoparametric elements and 6075 nodes. Twenty-four planes of elements were used in the circumferential direction. The finite element program used for these 3D calculations is called ALT3D [ALT3D]. The ALT3D element formulation used in this calculation includes extra incompatible shape functions which allow the elements to accurately represent bending behavior with only a single element representing the entire wall thickness. Two elements were used through the wall in the model primarily to improve the quality of stress contour plots. A double noded plane was introduced at the location of the H4 weld to facilitate the simulation of various shrinkage and misfit situations. Figure 2-12 shows a perspective plot of the 3D grid.

### 2.3.2 Verification of the 3D Model

A check calculation was run to test the accuracy of the ALT3D program and the 3D grid. Since the bottom portion of the shroud is greater than  $3\sqrt{Rt}$  in axial length, it provided an opportunity to solve a problem that has solutions readily available in handbooks. The problem is that of a very long thin walled cylinder with a uniform (axisymmetric) bending moment applied around the circumference at one end. With the current 3D grid, the upper shroud was disconnected from the lower shroud at the H4 interface and the axisymmetric moment applied to the upper edge of the lower shroud assembly. The analytical solution provides both the radial displacement and the rotation of the edge where the moment is applied. The ALT3D solution was 1.2% below the analytical solution for the rotation and 1.7% below the analytical solution for the radial displacement.

### 2.3.3 Solutions for Non-Axisymmetric Weld Shrinkage

The desired sinusoidal variation in axial weld shrinkage was introduced to the 3D model as a relative axial displacement between the associated pairs of nodes at the H4 interface of the 3D model. While the axial displacements were forced to differ by the amount specified by the sinusoidal shrinkage variation and thus were discontinuous across the interface, the radial and circumferential displacements were required to be identical at the associated node pairs and were therefore continuous across the interface. Since no external forces were applied to the model the resulting stress fields necessarily satisfied all equilibrium requirements at the weld interface.

The introduction of the axial shrinkage variation resulted in bending in the shroud which induced axial stress variations (i.e., bending stress) across the wall thickness in addition to the anticipated net axial force (i.e., membrane stress). This bending shows up in a deformed shape plot of the H4 region as shown in Figure 2-13. The radial displacement magnitudes are exaggerated here for clarity and are representative of an axial shrinkage variation of plus and minus 1.0 inch. Therefore, it can be seen that the radial displacements at the weld are similar in magnitude to the applied axial shrinkage variation. It can also be seen that the deformation behavior has the same sinusoidal variation as the applied shrinkage variation.

The axial stress behavior at the H4 weld ( $\sigma_{yy}$  in the 3D model coordinates) is shown in Figure 2-14. Again, the behavior is sinusoidal. The stresses in this plot correspond to an axial shrinkage variation magnitude of 0.01 inch. To relate these sinusoidal variations to lengths of variations in the real weld, where sinusoidal variations would not generally be expected, a parameter L is defined and illustrated in Figure 2-14. The parameter L is the circumferential



1000  
1000  
1000



1000  
1000



distance over which the assumed axial shrinkage variation goes from zero to a peak value and back to zero. The variation lengths considered in this study, corresponding to the 2, 4, 8, and 16 cycle cases, were 139, 70, 35, and 17 inches. It can be seen that the axial stresses at all locations on the circumference have a membrane stress component and a bending stress component.

The absolute magnitude of the membrane and bending stress components induced by the shrinkage variation and their relative magnitudes depend on the length of the assumed axial shrinkage variation. For the two cycle ( $L=139$  in.) and four cycle ( $L=70$  in.) variations, the bending stress components are larger than the membrane stress components. For the 8 cycle case ( $L=35$  in.), the two components are about equal in magnitude. For higher cycles (shorter lengths), the membrane component is the larger.

The stress effects of the axial shrinkage variation simulations are summarized in Figure 2-15. In this plot, the length of the variation is divided by the shroud circumference to provide a better perspective on the size of the variation with respect to the length of the weld. For this plot, a peak axial shrinkage variation magnitude of 0.006 in. is assumed. Since the analysis is linear, these results scale with the assumed peak shrinkage. The 0.006 in. shrinkage assumed here is 10% of the total transverse weld shrinkage that was computed in the axisymmetric welding simulation. This value is believed to be a conservative estimate of the variation that could reasonably be expected in the H4 weld for the lengths of variations being considered here (17 in. to 139 inch). However, no data appears to be available to support this estimate. For the shorter variation lengths considered here, and for even shorter lengths than those which were considered, it seems that a 10% variation may be overly conservative. This is because it becomes more difficult to create a variation of a fixed magnitude over shorter and shorter lengths (as evidenced by the larger axial stresses).

Three key behaviors can be seen in Figure 2-15.

1. For a given shrinkage variation magnitude, the induced axial stresses increase as the variation length decreases.
2. The membrane component is smaller than the bending component for large variation lengths, but becomes smaller than the membrane component for smaller lengths.
3. The membrane and bending components always combine so that the magnitude of the combined stress is larger at the inner surface.

It should be kept in mind that the peak tensile stresses shown in Figure 2-15 are accompanied by their compressive counterpart. For every tensile region there is a compressive region at some other location on the circumference.

#### 2.3.4 Ovality Effects

The desired sinusoidal variation in radial mismatch at the H4 weld was introduced in the 3D model as a relative radial displacement between the associated pairs of nodes at the H4

Faint, illegible text, possibly a header or introductory paragraph.

**Table**  
Faint text, possibly a table or list of items.

interface of the 3D model. While the radial displacements were forced to differ by the amount specified by the sinusoidal mismatch variation, and thus were discontinuous across the interface, the axial and circumferential displacements were required to be identical at the associated node pairs and were therefore continuous across the interface. Since no external forces were applied to the model, the resulting stress fields necessarily satisfied all equilibrium requirements at the weld interface.

The form of the initial radial mismatch is illustrated in the deformed shape plot of Figure 2-16. In this plot the shroud is inverted so that the top of the plot corresponds to the bottom of the shroud. The peak radial mismatch at the H4 weld is 1.0 inch and occurs at the section depicted in this figure. It should be noted that though the analysis calculates the stresses in going from the initial, perfect, undeformed geometry to the deformed shape depicted in this figure, these stresses are exactly the same except for a sign change as the stresses that would be produced in going from a geometry that is initially stress free in the shape of the deformed mesh in Figure 2-16 and that ends up in the perfectly cylindrical shape of the undeformed mesh.

It is clear from the deformed shape of Figure 2-16 that bending stresses will be created above and below the H4 weld plane. It can also be seen that if the ID axial stresses are tensile above the weld, then the ID axial stresses below the weld will be compressive. This change in sign of the axial stresses on opposite sides of the weld indicates that somewhere in the vicinity of the weld there must be an inflection point (i.e., a point where curvature of the wall is zero, thus leading to zero bending stresses). The axial stress contour plots of Figure 2-17 show the stresses for the two cycle and sixteen cycle cases. The bending inflection point is clear in these plots.

Figure 2-18 summarizes the peak axial stresses that result from an assumed maximum radial mismatch of 0.5 in. Note that these are not HAZ stresses. These stresses occur at least several inches from either HAZ. It can be seen that the peak bending stress does not change much in going from 2 cycles ( $L = 139$  in.) to 8 cycles ( $L = 35$  in.). However, there is a large change in going from the 8 cycle case to the 16 cycle ( $L = 17$  in.) case. The radial mismatch magnitude for these stresses was based on the General Electric (GE) specified tolerance for the shroud of 176 in. diameter  $\pm 0.5$  in. While this is clearly a reasonable and conservative value for the lower cycle cases, it seems that as higher cycle cases are considered, a lower peak radial mismatch would be more reasonable. Again, there is no data to guide the selection of radial mismatch magnitudes or frequencies.

It can be seen from Figure 2-17 that the bending inflection point is very near to the H4 weld. If the top and bottom shroud assemblies had the same stiffness (i.e., a radial shear load induces equal radial displacements and rotations for both assemblies), this inflection point would be exactly centered on the weld. Since the top and bottom assemblies have different stiffnesses, the inflection point tends to be shifted above the H4 weld (below H4 in the inverted plots). It can also be seen from Figure 2-17 that the distance from the inflection point to the section with the peak bending stresses depends on the length of the mismatch (i.e., number of cycles) and that the distances to the peak locations above and below H4 are different. Table 2-3 summarizes the locations of the peak axial stresses and the inflection points relative to the center of the H4 weld. Resolution is limited to 0.5 inches in this table due to the relative coarseness of the finite element grid.



Since estimates were desired for the H4 weld HAZ axial stresses due to radial mismatch, and since getting these from the finite element grid would be prone to large errors due to the lack of grid refinement, the following approach was used. For the axisymmetric problem of a uniformly distributed radial shear force applied to the end of a long cylinder, the axial stresses are related to the peak axial stress as follows:

$$\frac{\sigma(x)}{\sigma_{\max}} = \frac{e^{-\lambda x} \sin \lambda x}{0.3225}$$

where  $x$  is the distance from the end of the cylinder and

$$\lambda = \left[ \frac{3(1-\nu^2)}{R^2 t^2} \right]^{\frac{1}{4}}$$

Note that the axial stress is zero at the end thus making the end of the cylinder an inflection point. The above stress relation does not apply directly to the current cases because the radial shear force at our inflection point is not axisymmetric. However, if we replace  $\lambda$  with a parameter  $\beta$ , we can use our finite element based information on peak stress magnitude and distance to determine an appropriate  $\beta$  for each of our four cases. Note that since the distances are different for stress peaks above and below the weld, a total of 8  $\beta$ 's are involved. Knowing  $\beta$ , the peak stress magnitude, and the distance of the HAZs from the inflection point, we can then estimate the bending stress in each HAZ for each of the four circumferential variation cases.

This method for obtaining the HAZ stresses has two main benefits compared to the direct use of the finite element results. The first is that the positions tabulated in Table 2-3 benefited to some degree from the fact that a trend with respect to the number of cycles could be used to smooth the distances taken from the finite element contour plots. Second, the only measurements required are those in Table 2-3. In spite of these advantages, the 0.5 inch accuracy of these measurements can lead to significant inaccuracies in the estimated HAZ stresses. However, since the actual shroud HAZ stresses are also very sensitive to the position of the inflection point, and since small variations from the assumed sinusoidal distribution would probably lead to significant shifts in the inflection point position, obtaining more accurate HAZ stresses for the idealized sinusoidal variation is probably not justified.

The distances from the inflection point to the peak stress locations ( $x_{\max}$ ) and the resulting  $\beta$ 's are tabulated in Table 2-4. To calculate the HAZ stresses then involves computing the distances of the HAZ's from the inflection points for each case and using the analytical stress relationship with the appropriate  $\beta$ 's.

The final results of the process to estimate axial stresses in the HAZ's due to radial mismatch are given in Table 2-5. The stresses in Table 2-5 are again based on an assumed peak radial mismatch of 0.5 in. (based on the GE specified tolerance of 176 in. dia  $\pm 0.5$  in. and the



1. The first part of the document discusses the importance of maintaining accurate records of all transactions. It emphasizes that this is crucial for ensuring the integrity of the financial statements and for providing a clear audit trail. The text also mentions that proper record-keeping is essential for identifying and correcting errors in a timely manner.



2. The second part of the document focuses on the role of internal controls in preventing fraud and misstatements. It highlights that a strong internal control system is necessary to ensure that all transactions are properly authorized, recorded, and reviewed. The text also discusses the importance of segregation of duties and the need for regular monitoring and evaluation of the internal control system.



further assumption that the top and bottom are aligned so that the maximum radial mismatch occurs across the weld).

There are three main conclusions that can be made based on the results of this radial mismatch analysis:

1. Radial mismatch can induce very large stresses.
2. The largest stresses due to mismatch do not occur in the HAZ because there is a bending inflection near the weld region.
3. Because the bending inflection tends to be slightly above H4, the radial mismatch tends to induce much larger stresses in the lower HAZ than in the upper HAZ.

## 2.4 Stress Intensity Factor Calculations

The prediction of stress corrosion cracking behavior at the H4 weld requires that the stress intensity factor be known as a function of crack depth for the operating steady state condition. Since a handbook solution applicable to the large R/t ratio of the shroud was not found, it was judged necessary to compute stress intensity factors using the finite element model. If the finite element results showed that a handbook solution for a similar geometry (e.g., smaller R/t) would be reasonably accurate for cracking at H4, then subsequent calculations could use the handbook solution.

### 2.4.1 Method

The method used for computing stress intensity factors with the finite element model is based on the concept of energy release rate, the relationship between energy release rate and the stress intensity factor, and the crack closure integral method [IRW57] for computing crack energy release rates. The crack closure integral allows the energy release rate for a cracked body to be determined from the stress in the vicinity of the crack tip just prior to some small crack extension ( $\Delta a$ ) and the crack opening displacements after this small extension. Basically, the energy release rate is equal to the work that must be done to close the crack over the distance  $\Delta a$  (thus restoring the crack to the state that existed before the increment in crack size) divided by the change in crack area. For a finite element model, this integral is most conveniently formulated in terms of the nodal forces at the coupled crack tip nodes prior to a crack extension and the opening displacement between these nodes after they are uncoupled and the crack is allowed to extend by one element. The work done to reattach the nodes is  $f\delta/2$ , where  $f$  is the node force before the nodes are released, and  $\delta$  is the opening between the nodes after release. Since the energy release rate calculation involves an increment in crack growth, the resulting energy release rate and stress intensity factor are assumed to be most representative of the average crack size during the crack size increment.

Figure 2-19 compares a finite element  $K_I$  computation [RYB81] using the above calculation method with an exact solution [TPI73]. The grid used in [RYB81] had 20 elements



The first part of the document discusses the importance of maintaining accurate records of all transactions. It emphasizes that proper record-keeping is essential for ensuring the integrity and reliability of financial data. This section also outlines the various methods and tools used to collect and analyze financial information, highlighting the need for consistency and transparency in the reporting process.



In addition, the document addresses the challenges associated with data collection and analysis, particularly in the context of large-scale operations. It discusses the potential for errors and biases in data collection and provides strategies to minimize these risks. The text also touches upon the importance of data security and the need to implement robust safeguards to protect sensitive information from unauthorized access and disclosure.

Finally, the document concludes by reiterating the significance of accurate financial reporting and the role of the accounting profession in ensuring the accuracy and reliability of financial statements. It encourages stakeholders to remain vigilant and committed to the highest standards of professional conduct and ethical behavior in all financial transactions.



through the thickness. It can be seen that the method provides a quite accurate solution without special methods for modeling crack tip singularities, etc. The accuracy of the method depends on the degree of grid refinement (i.e., the number of elements along the crack path) and on the crack size relative to the grid refinement. Accuracy improves as the crack depth increases from one to three or four elements and begins to decrease when the uncracked ligament is represented by less than four elements.

The crack closure integral method can be used to compute Mode I ( $K_I$ ) and Mode II ( $K_{II}$ ) stress intensity factors. The energy due to crack plane normal node forces and displacements leads to the Mode I energy release rate ( $G_I$ ) and the energy due to the crack plane parallel node forces and displacements leads to the Mode II energy release rate ( $G_{II}$ ). For plane strain conditions (which are applicable to the axisymmetric geometry), these energy release rates are related to  $K_I$  and  $K_{II}$  by:

$$G_I = \frac{(1-\nu^2)}{E} K_I^2 \text{ and } G_{II} = \frac{(1-\nu^2)}{E} K_{II}^2$$

Since cracks tend to grow in the direction that maximizes the Mode I energy release rate (consequently minimizing the Mode II energy release rate), the Mode II energy release rate is often small compared to the Mode I value. Therefore, it is rare that Mode II energy release rates or stress intensity factors are used in crack growth models.

In the present stress intensity factor calculations, the Mode II energy release rates are generally small compared to the Mode I values. However, rather than ignore the energy release that is associated with the Mode II behavior, the following conservative procedure was adopted. The Mode I and Mode II energy release rates were added together, and then used to compute an "effective" stress intensity factor:

$$(K_I)_{\text{effective}} = \sqrt{\frac{E}{(1-\nu^2)} (G_I + G_{II})}$$

Since the Mode II energy release rates were generally small compared to the Mode I values, this method resulted in small increases in the computed stress intensity factors compared to those that would have been computed if the Mode II energy release rate had been ignored.

In this study, the crack growth is assumed to follow the HAZ. This results in the cracks growing at an angle to the surface of the shroud. In computing the energy release rates, the actual new crack surface area is computed based on the angled crack plane. However, when the  $K_I$  solutions are plotted as a function of crack size, the crack sizes are measured perpendicular to the shroud surfaces rather than along the angled crack path.



[The page contains extremely faint and illegible text, likely bleed-through from the reverse side of the document. The text is scattered across the page and does not form any recognizable words or sentences.]

#### 2.4.2 Comparison of Finite Element Stress Intensity Factors to Handbook Values

To check that the finite element stress intensity factor solutions were reasonable, they were compared to solutions for several similar and bounding geometries. In doing this exercise, the pc-CRACK software [PCCRACK] was used for the so-called handbook calculations. The stresses used in this comparison were the stresses due to the axisymmetric weld simulation at operating conditions, but without including the artificial 3D constraint. The finite element  $K_I$  solutions were compared to pc-CRACK solutions based on the single edge crack (SEC) geometry, the crack in a half space geometry, and two cracked cylinder geometries. The cylinders had  $R/t$ 's of 10 and 5, and were intended for cracks growing from the inner surface. The shroud  $R/t$  is about 59 and the finite element model was used to grow the crack from the outer surface.

The results of this  $K_I$  comparison are shown in Figure 2-20. It can be seen that all of the solutions tend to be in agreement for small crack sizes. This reflects the fact that  $K_I$  for these crack depths is largely unaffected by all aspects of the geometry except the crack depth. As expected, the SEC geometry provides an upper bound on the behavior of the shroud for larger crack sizes, and the half space geometry provides a lower bound. However, neither would be satisfactory for computations with crack sizes greater than about 0.4 inches. The two handbook cylinder geometries on the other hand tend to be in reasonable agreement with the finite element solution for crack sizes up to about 0.7 in.

It is apparent from Figure 2-20 that the finite element solution tends to be below the handbook solutions in the small crack size range. The explanation for this is believed to be the fact that the finite element crack path follows the HAZ rather than a radial crack path. By forcing the crack to grow at an angle, we are not allowing it to release the maximum amount of energy. A reduced energy release leads to a reduced  $K_I$ . This effect would be even larger if the mode I and mode II energies were not combined in computing an effective  $K_I$  as described above.

#### 2.4.3 Stress Intensity Factor Solutions for the H4 Weld at Operating Conditions

The stress intensity factor solutions for a crack growing in the HAZ of the H4 weld under operating conditions are shown in Figures 2-21 and 2-22. Figure 2-21 shows the solution for a crack growing from the outer surface while Figure 2-22 shows the solution for a crack growing from the inner surface. Since the computed  $K_I$  from the first finite element node release is not as accurate as can be computed by hand using the surface stress and the half space solution ( $K_I = 1.12\sigma\sqrt{\pi a}$ ), this approach was used for computing  $K_I$  for crack sizes less than 0.05 inches.

Comparing the solution in Figure 2-21 to that in Figure 2-20, it can be seen that there is some difference. The difference is that the solution in Figure 2-21 was obtained using the welding residual stresses computed with artificial 3D constraint while that in Figure 2-20 used welding residual stresses computed without artificial 3D constraint. Clearly, using the solution obtained with the constraint will lead to more conservative crack growth estimates for cracks growing from the OD surface.

The  $K_I$  solution of Figure 2-21 shows that the stress state will not tend to arrest a crack that initiates at the OD. On the other hand, the  $K_I$  solution of Figure 2-22 shows that a crack



that grows from the inner surface will arrest after about 0.2 inches of crack growth. That is, once  $K_I$  becomes negative, further crack growth is not possible. It should be noted that the  $K_I$  solutions of Figures 2-21 and 2-22 do not include any effect of non-axisymmetric axial weld shrinkage or radial mismatch. The effects of these additional stresses are addressed in the crack growth analysis section of this report.

For linear elastic fracture mechanics (LEFM), it is often beneficial to compute stress intensity factors for each type of loading rather than to superimpose the stresses and then compute a stress intensity factor solution for the combined stresses. By getting the  $K_I$  solutions for the separate load cases, it is then possible to scale the individual load cases and combine the resulting scaled stress intensity factor solutions; thus eliminating the need to obtain a new stress intensity factor solution for each load combination of interest. This is the approach used in the subsequent crack growth studies.

In the present study, the welding residual stresses are the primary loading. Therefore using the more accurate finite element stress intensity factor solutions for this load component is justified. However, since the axial shrinkage variation and radial mismatch stresses are generally introduced for the purpose of sensitivity studies, using the more accurate finite element approach for these load cases was judged unnecessary. Therefore, the stress intensity factor solutions for these load cases are based on the  $R/t = 10$  handbook solution of pc-CRACK.



*[Faint, illegible text, possibly bleed-through from the reverse side of the page.]*



**Table 2-1 Temperature Dependent Mechanical Properties for Type 304 SS Base Metal and Type 308 SS Weld Metal**

**MATERIAL 1  
SS 304 BASE**

Temperature	Elastic Modulus (psi)	Poissons Ratio	Mean Thermal Expansion Coefficient ( $^{\circ}\text{F}^{-1}$ ) (70 $^{\circ}\text{F}$ Reference Temperature)	Hardening Modulus (psi)	Yield Strength (psi)
50.	28700000.	0.26	.0000086	539700.	36000.
300.	27100000.	0.28	.0000090	452300.	31100.
550.	25800000.	0.31	.0000095	364800.	25900.
750.	24200000.	0.32	.0000098	296300.	22300.
1000.	22500000.	0.30	.0000102	217900.	18500.
1300.	20200000.	0.28	.0000105	139000.	14900.
1600.	16000000.	0.24	.0000108	79600.	10200.
2100.	10000.	0.22	.0000113	1000.	1000.

**MATERIAL 2  
SS 308 WELD**

Temperature	Elastic Modulus (psi)	Poissons Ratio	Mean Thermal Expansion Coefficient ( $^{\circ}\text{F}^{-1}$ ) (2100 $^{\circ}\text{F}$ Reference Temperature)	Hardening Modulus (psi)	Yield Strength (psi)
50.	28700000.	0.26	.0000113	539700.	45000.
300.	27100000.	0.28	.0000116	452300.	38900.
550.	25800000.	0.31	.0000119	364800.	32400.
750.	24200000.	0.32	.0000121	296300.	27900.
1000.	22500000.	0.30	.0000122	217900.	23100.
1300.	20200000.	0.28	.0000125	139000.	18600.
1600.	16000000.	0.24	.0000128	79600.	12800.
2100.	10000.	0.22	.0000133	1000.	1000.



**Table 2-2 Heat Transfer Material Properties for Stainless Steel Base and Weld Metals**

Conductivity: 0.000266 BTU/in/sec/F

Heat Capacity: 0.0381 BTU/in<sup>3</sup>/F



**Table 2-3 Characterization of the Radial Mismatch Induced Axial Stress Distributions**

Case	Distance From the Center of H4 to the Peak Stress Location (in.)		Inflection Point Distance Above H4 (in.)
	Bottom	Top	
2 cycle	8.5	7.0	0.5
4 cycle	7.5	6.5	1.0
8 cycle	5.5	6.0	1.5
16 cycle	3.5	3.0	1.5



Table 2-4 Distances of Peak Stresses From the Inflection Point and Computed  $\beta$ 's

Case	$X_{\max}$ (in.)		$\beta$ (in <sup>-1</sup> )	
	Bottom	Top	Bottom	Top
2 cycle	9.0	6.5	0.0872	0.121
4 cycle	8.5	5.5	0.0924	0.143
8 cycle	7.0	4.5	0.112	0.175
16 cycle	5.0	1.5	0.157	0.524



**Table 2-5 Summary of HAZ Positions Relative to the Inflection Point and Estimated HAZ Stresses for a 0.5 in. Radial Mismatch**

Case	H4 HAZ	x (in.)	Axial Stress (ksi)
2	top	0.0	0.0
	bottom	1.0	11.4
4	top	0.5	6.6
	bottom	1.5	18.0
8	top	1.0	15.4
	bottom	2.0	27.6
16	top	1.0	33.2
	bottom	2.0	56.0



*[Faint, illegible text or markings in the center of the page, possibly bleed-through from the reverse side.]*



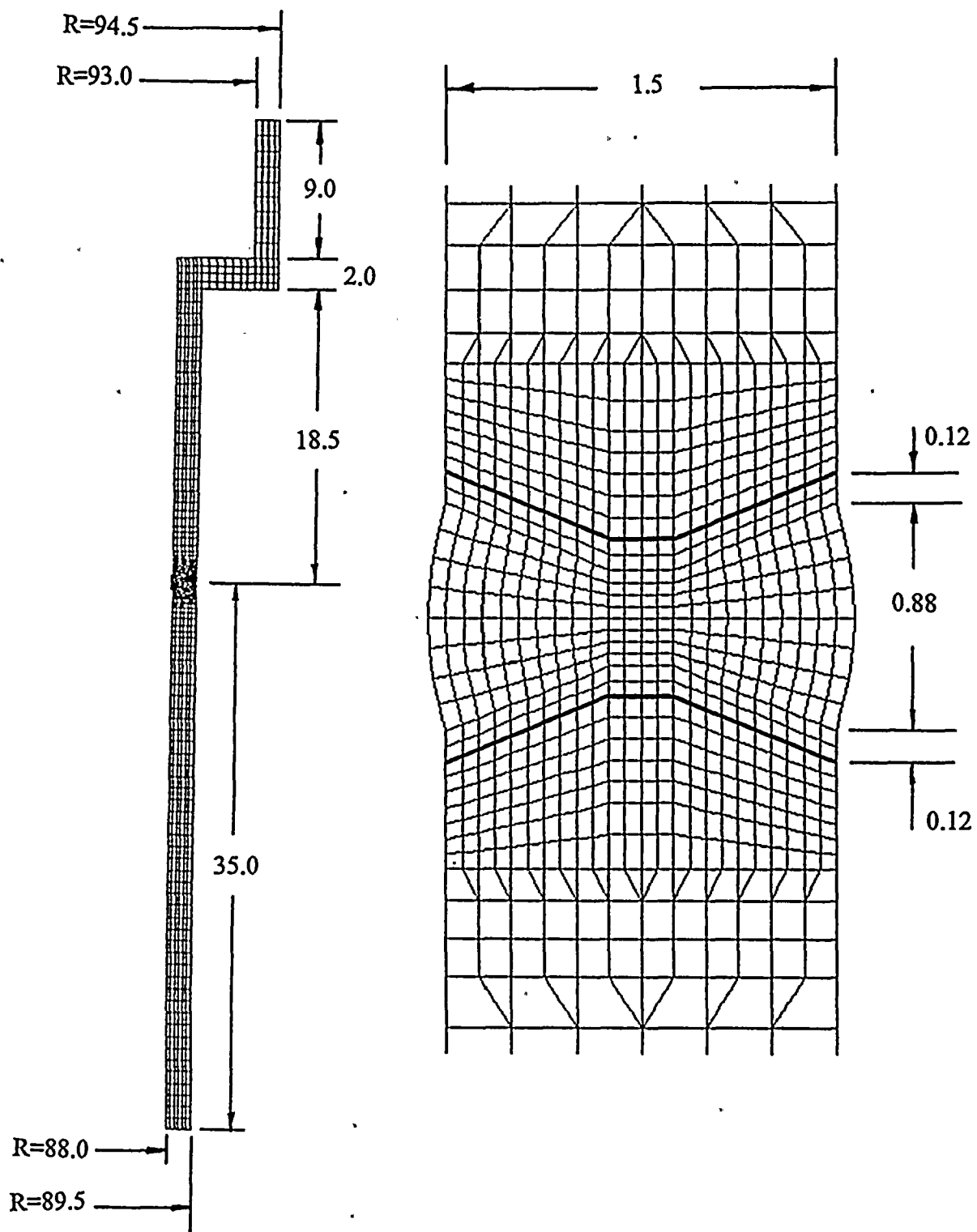


Figure 2-1 The 2D Axisymmetric Finite Element Grid



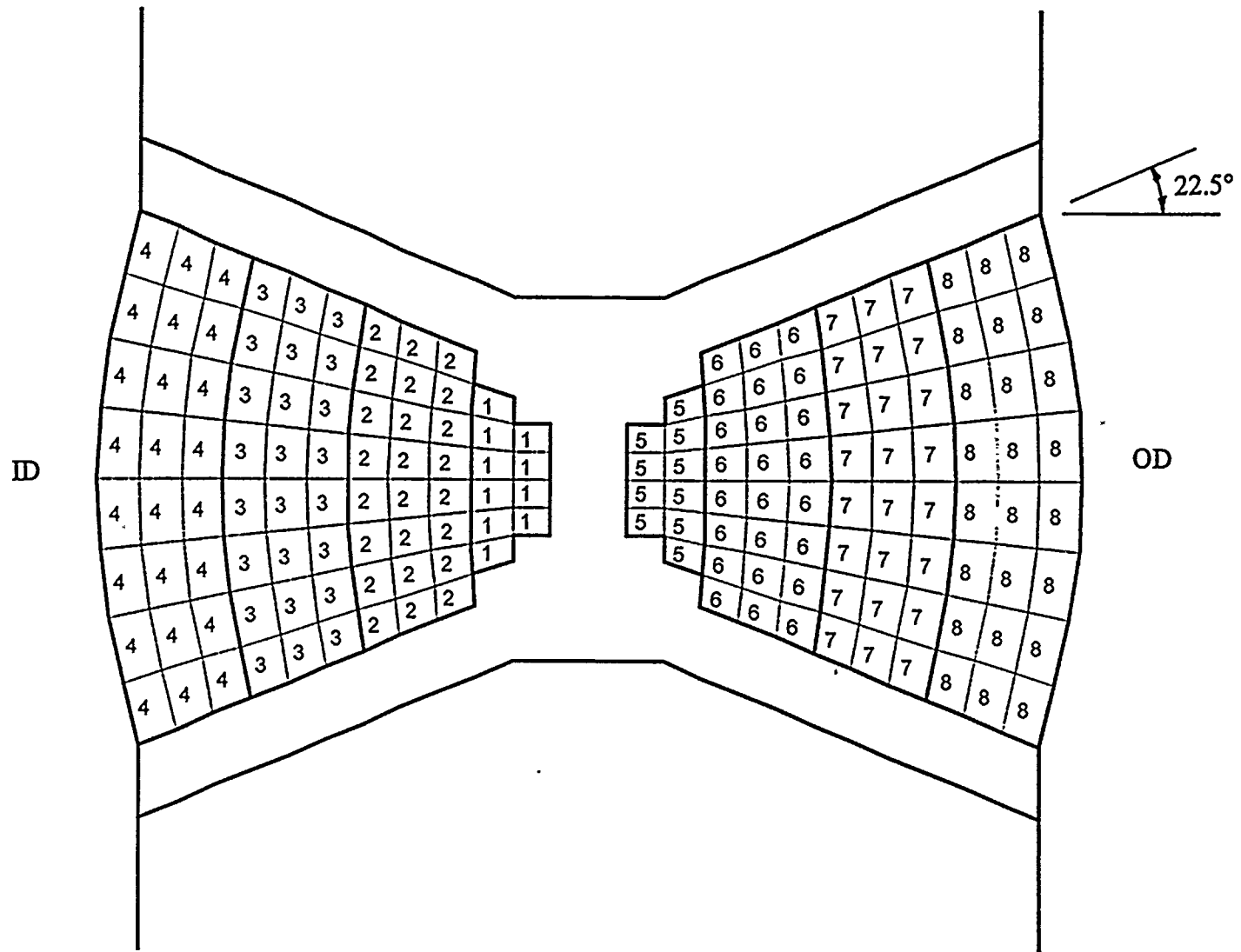
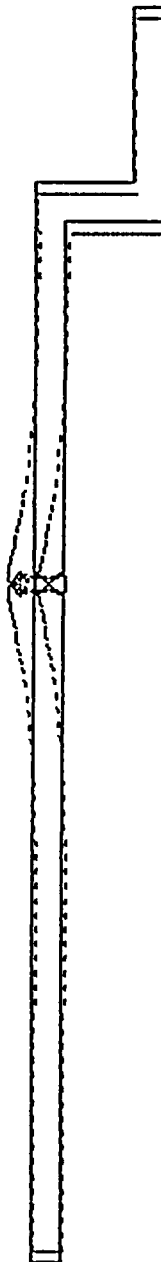


Figure 2-2 The Assumed Weld Passes and Welding Sequence for the H4 Weld Simulation



(x20)



H4 Weld Completed (70 F / with 3D constraint)

Figure 2-3 The Deformed Shape of the H4 Weld Region Predicted by the WELD3 Simulation (Deformation Exaggerated by a Factor of 20)



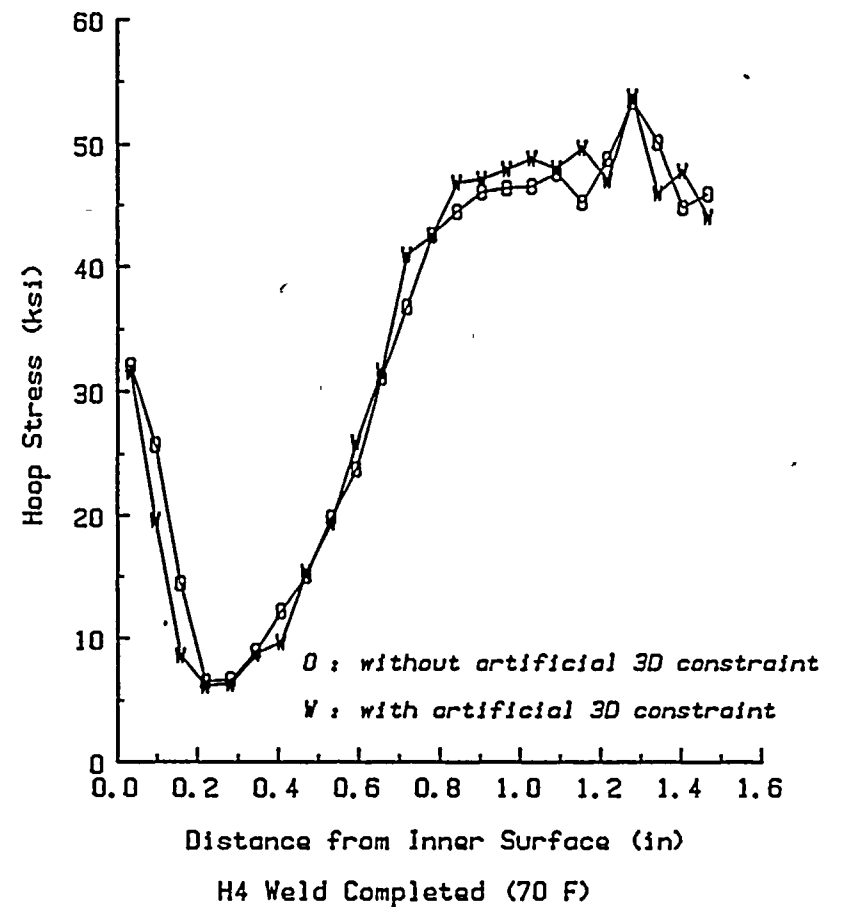
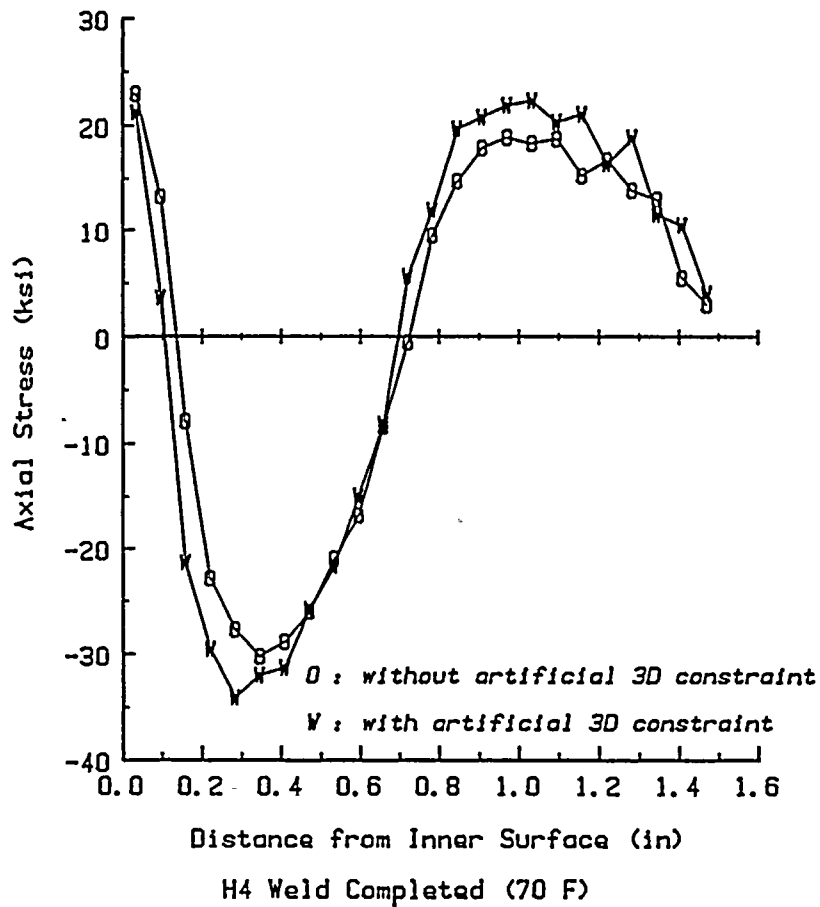


Figure 2-4 The Predicted Welding Residual Stresses in the Heat Affected Zones of the H4 Weld at 70°F



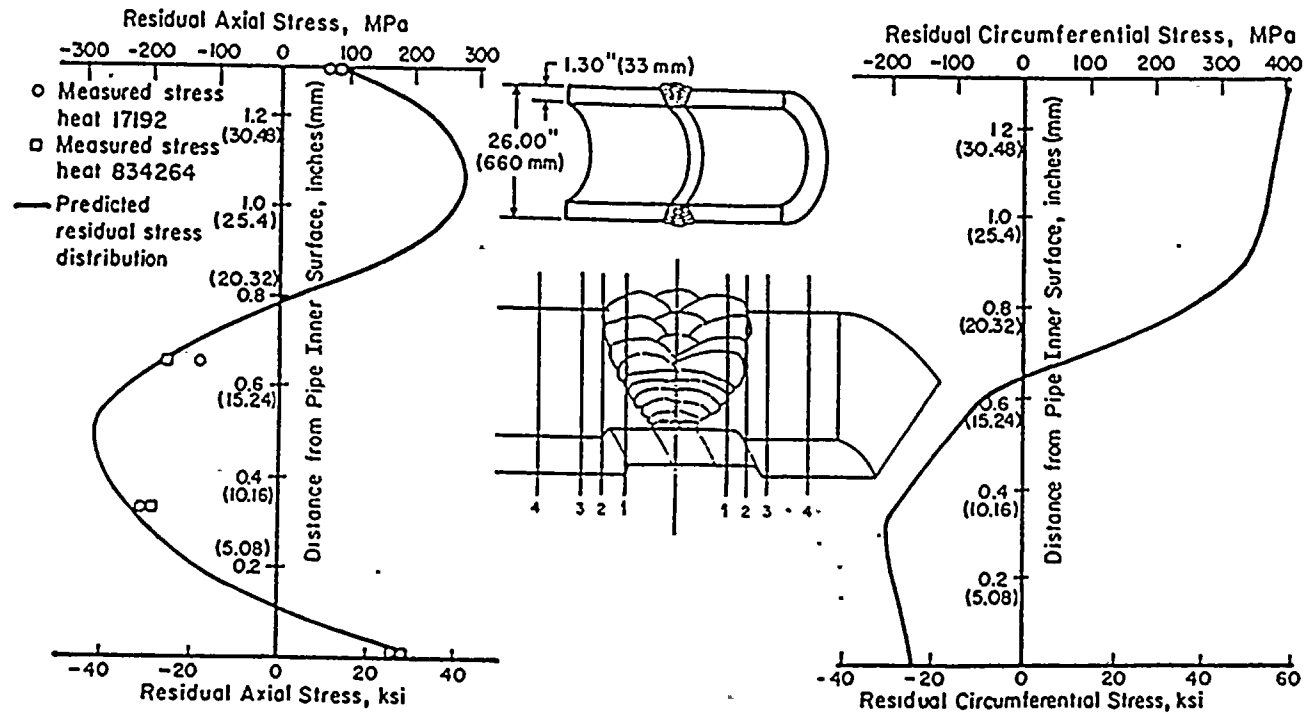


Figure 2-5 Predicted and Measured Throughwall Welding Residual Stresses in a 26 inch Diameter Pipe With a 1.3 inch Wall Thickness [EP1743]



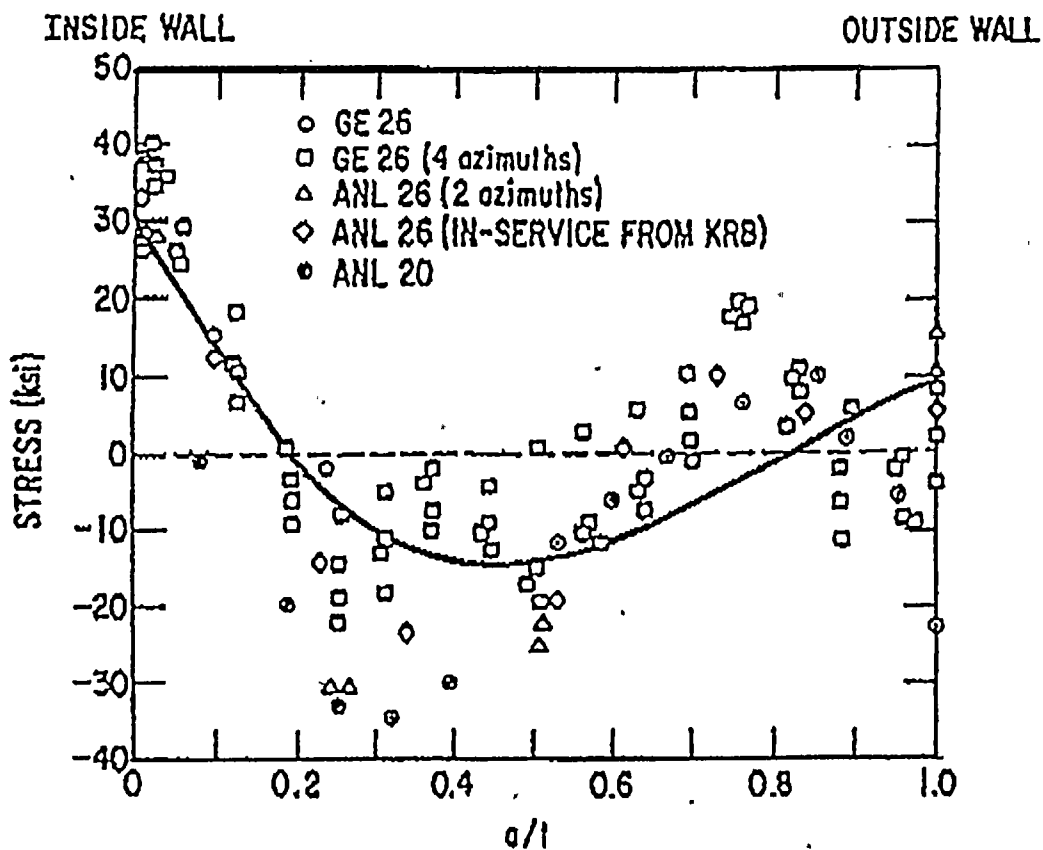


Figure 3  
Through-wall Distribution of Axial Residual  
Stress in Large-Diameter Pipes ( $t \geq 1$  in.)

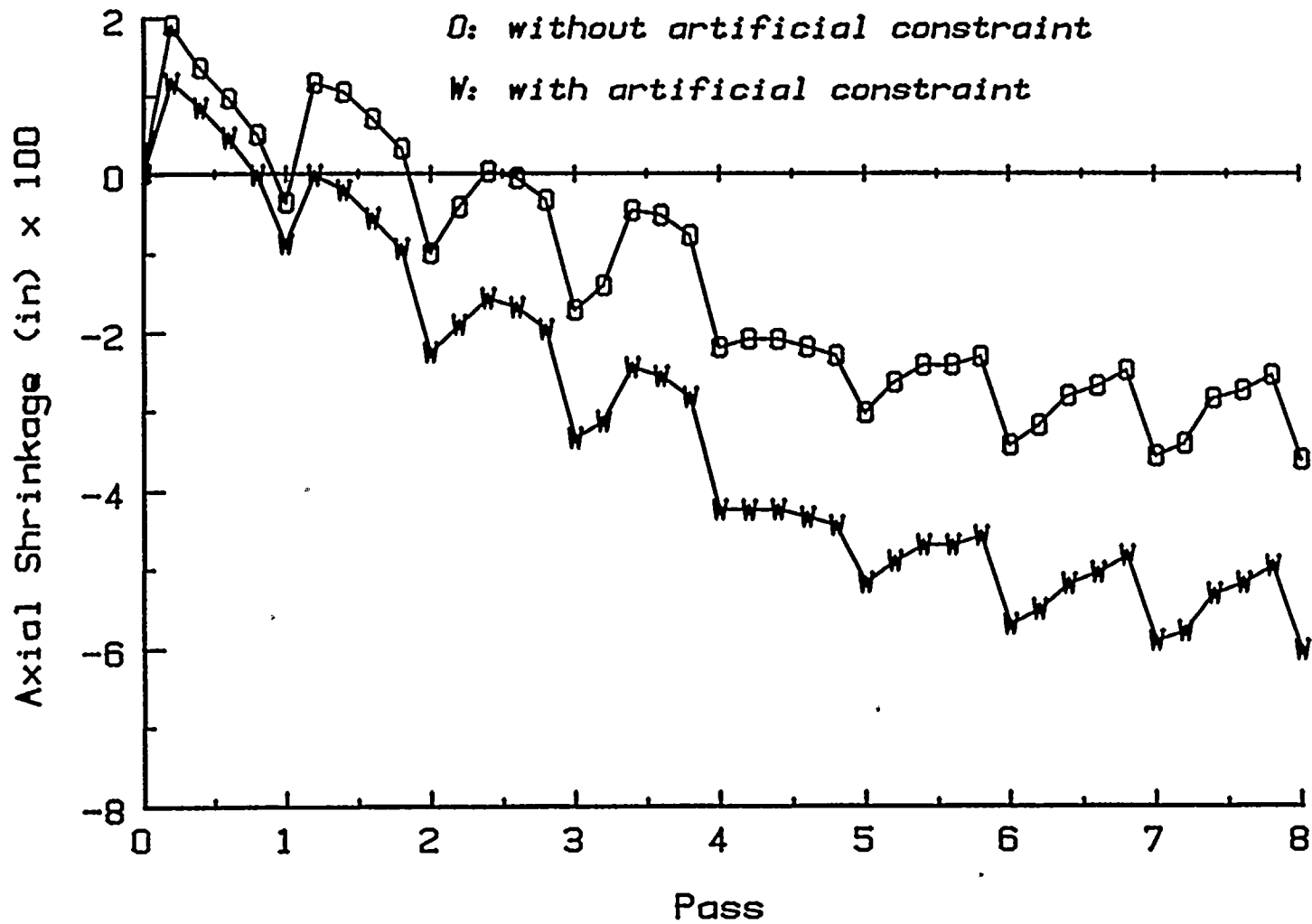
Figure 2-6 Measured Throughwall Axial Welding Residual Stress  
Distributions From Various Pipes With Wall Thicknesses  
Greater Than One Inch.



1  
 2  
 3  
 4  
 5  
 6  
 7  
 8  
 9  
 10  
 11  
 12  
 13  
 14  
 15  
 16  
 17  
 18  
 19  
 20  
 21  
 22  
 23  
 24  
 25  
 26  
 27  
 28  
 29  
 30  
 31  
 32  
 33  
 34  
 35  
 36  
 37  
 38  
 39  
 40  
 41  
 42  
 43  
 44  
 45  
 46  
 47  
 48  
 49  
 50  
 51  
 52  
 53  
 54  
 55  
 56  
 57  
 58  
 59  
 60  
 61  
 62  
 63  
 64  
 65  
 66  
 67  
 68  
 69  
 70  
 71  
 72  
 73  
 74  
 75  
 76  
 77  
 78  
 79  
 80  
 81  
 82  
 83  
 84  
 85  
 86  
 87  
 88  
 89  
 90  
 91  
 92  
 93  
 94  
 95  
 96  
 97  
 98  
 99  
 100

1  
 2  
 3  
 4  
 5  
 6  
 7  
 8  
 9  
 10  
 11  
 12  
 13  
 14  
 15  
 16  
 17  
 18  
 19  
 20  
 21  
 22  
 23  
 24  
 25  
 26  
 27  
 28  
 29  
 30  
 31  
 32  
 33  
 34  
 35  
 36  
 37  
 38  
 39  
 40  
 41  
 42  
 43  
 44  
 45  
 46  
 47  
 48  
 49  
 50  
 51  
 52  
 53  
 54  
 55  
 56  
 57  
 58  
 59  
 60  
 61  
 62  
 63  
 64  
 65  
 66  
 67  
 68  
 69  
 70  
 71  
 72  
 73  
 74  
 75  
 76  
 77  
 78  
 79  
 80  
 81  
 82  
 83  
 84  
 85  
 86  
 87  
 88  
 89  
 90  
 91  
 92  
 93  
 94  
 95  
 96  
 97  
 98  
 99  
 100

1  
 2  
 3  
 4  
 5  
 6  
 7  
 8  
 9  
 10  
 11  
 12  
 13  
 14  
 15  
 16  
 17  
 18  
 19  
 20  
 21  
 22  
 23  
 24  
 25  
 26  
 27  
 28  
 29  
 30  
 31  
 32  
 33  
 34  
 35  
 36  
 37  
 38  
 39  
 40  
 41  
 42  
 43  
 44  
 45  
 46  
 47  
 48  
 49  
 50  
 51  
 52  
 53  
 54  
 55  
 56  
 57  
 58  
 59  
 60  
 61  
 62  
 63  
 64  
 65  
 66  
 67  
 68  
 69  
 70  
 71  
 72  
 73  
 74  
 75  
 76  
 77  
 78  
 79  
 80  
 81  
 82  
 83  
 84  
 85  
 86  
 87  
 88  
 89  
 90  
 91  
 92  
 93  
 94  
 95  
 96  
 97  
 98  
 99  
 100



Predicted Axial Weld Shrinkage Behavior for H4

Figure 2-7 Predicted Axial Shrinkages for Weld H4 Both With and Without Use of the Artificial 3D Constraint Option of WELD3



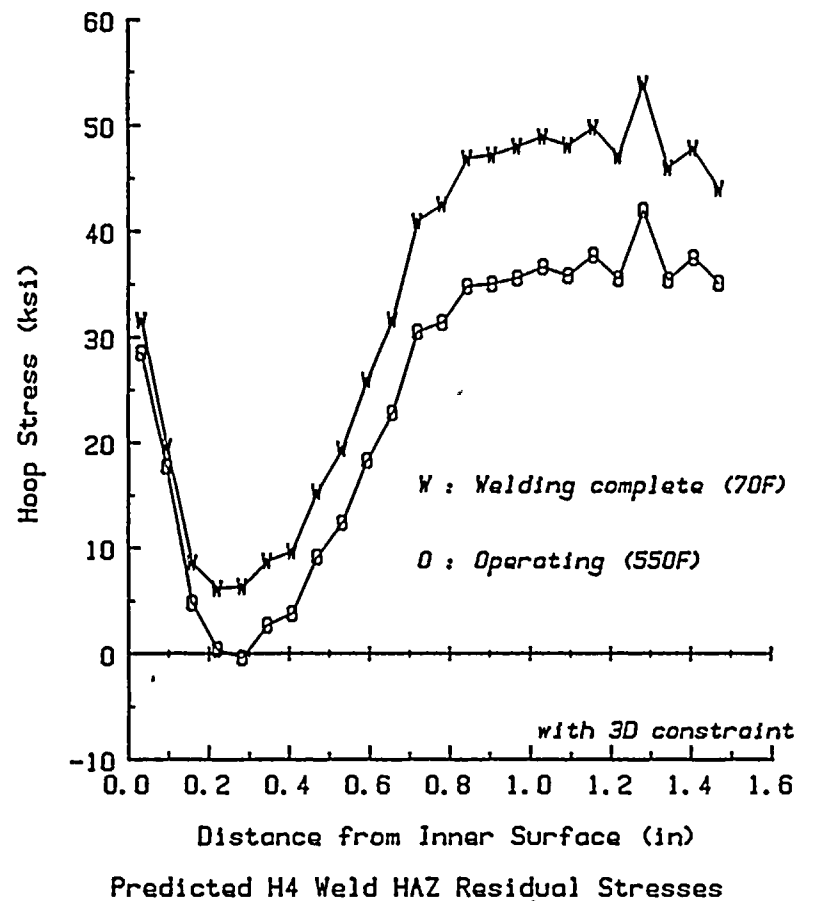
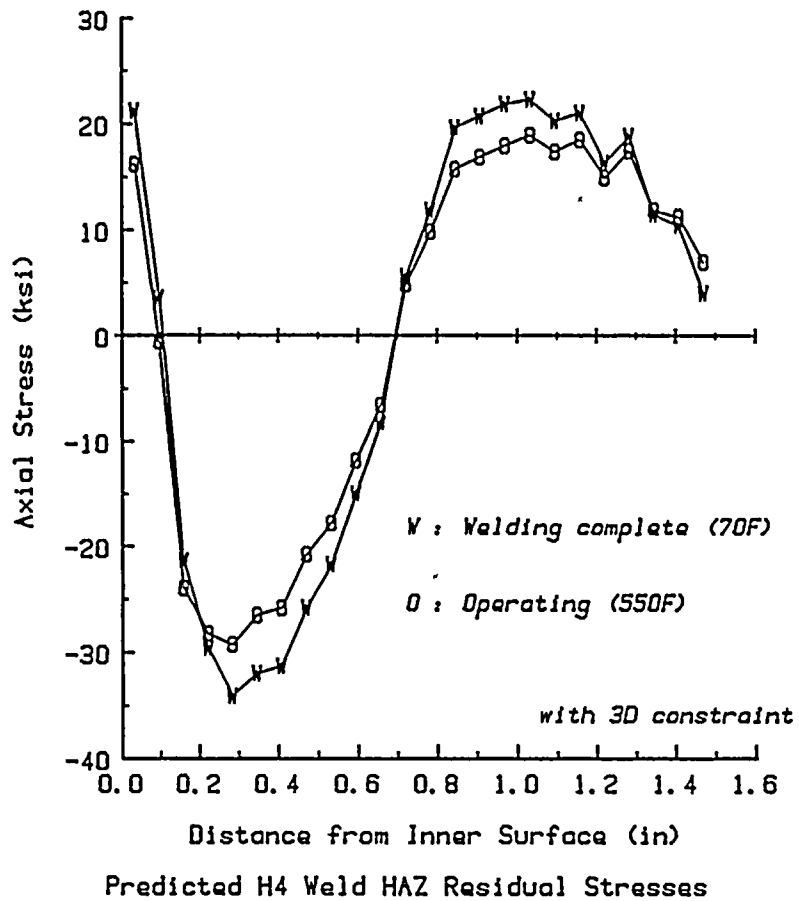
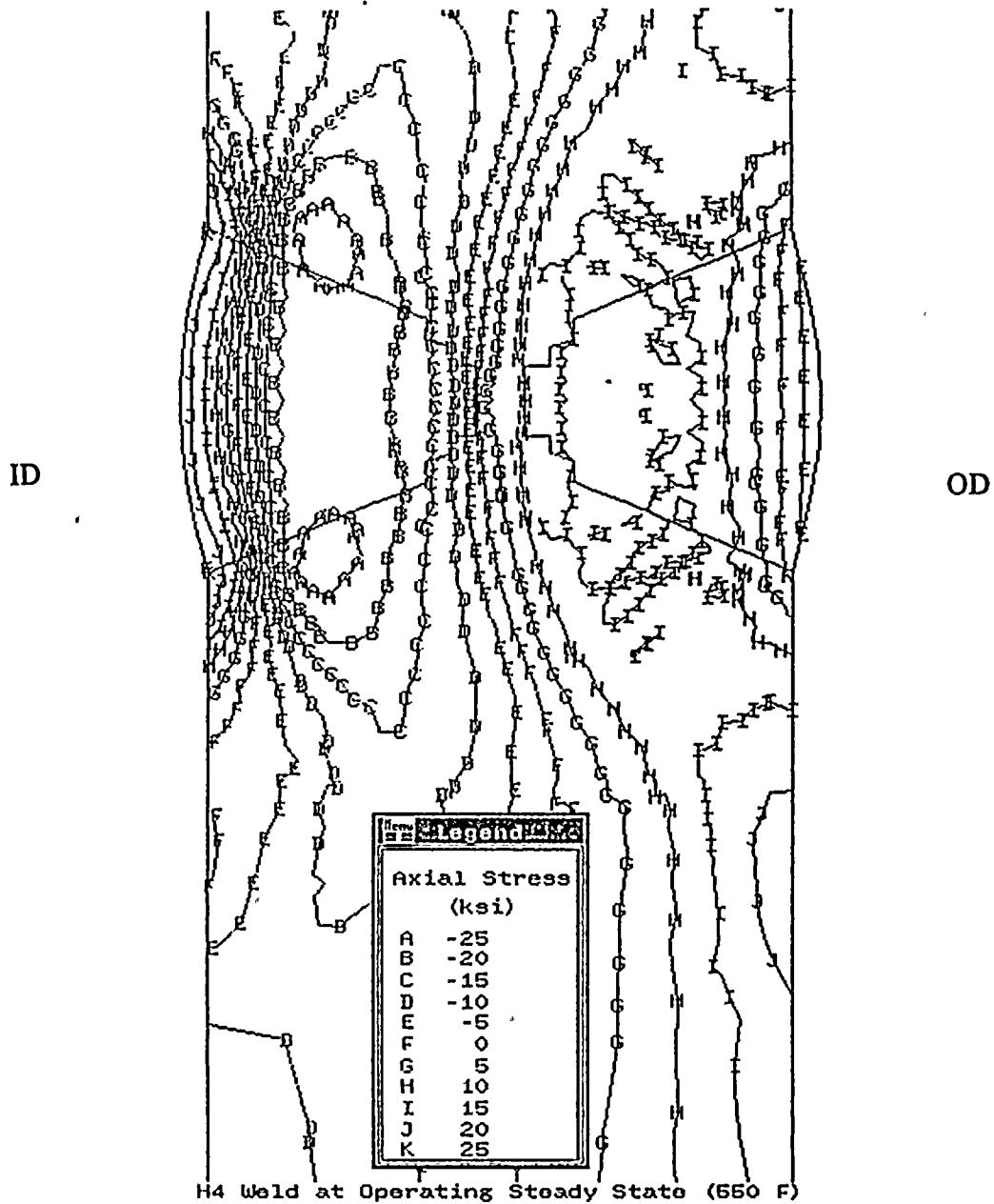


Figure 2-8 Predicted Welding Residual Stresses With Operating Loads and at an Operating Temperature of 550°F



1  
2  
3  
4  
5  
6  
7  
8  
9  
10  
11  
12  
13  
14  
15  
16  
17  
18  
19  
20  
21  
22  
23  
24  
25  
26  
27  
28  
29  
30  
31  
32  
33  
34  
35  
36  
37  
38  
39  
40  
41  
42  
43  
44  
45  
46  
47  
48  
49  
50  
51  
52  
53  
54  
55  
56  
57  
58  
59  
60  
61  
62  
63  
64  
65  
66  
67  
68  
69  
70  
71  
72  
73  
74  
75  
76  
77  
78  
79  
80  
81  
82  
83  
84  
85  
86  
87  
88  
89  
90  
91  
92  
93  
94  
95  
96  
97  
98  
99  
100





**Figure 2-9 Axial Stress Contours in the H4 Weld Region for Operating Conditions**



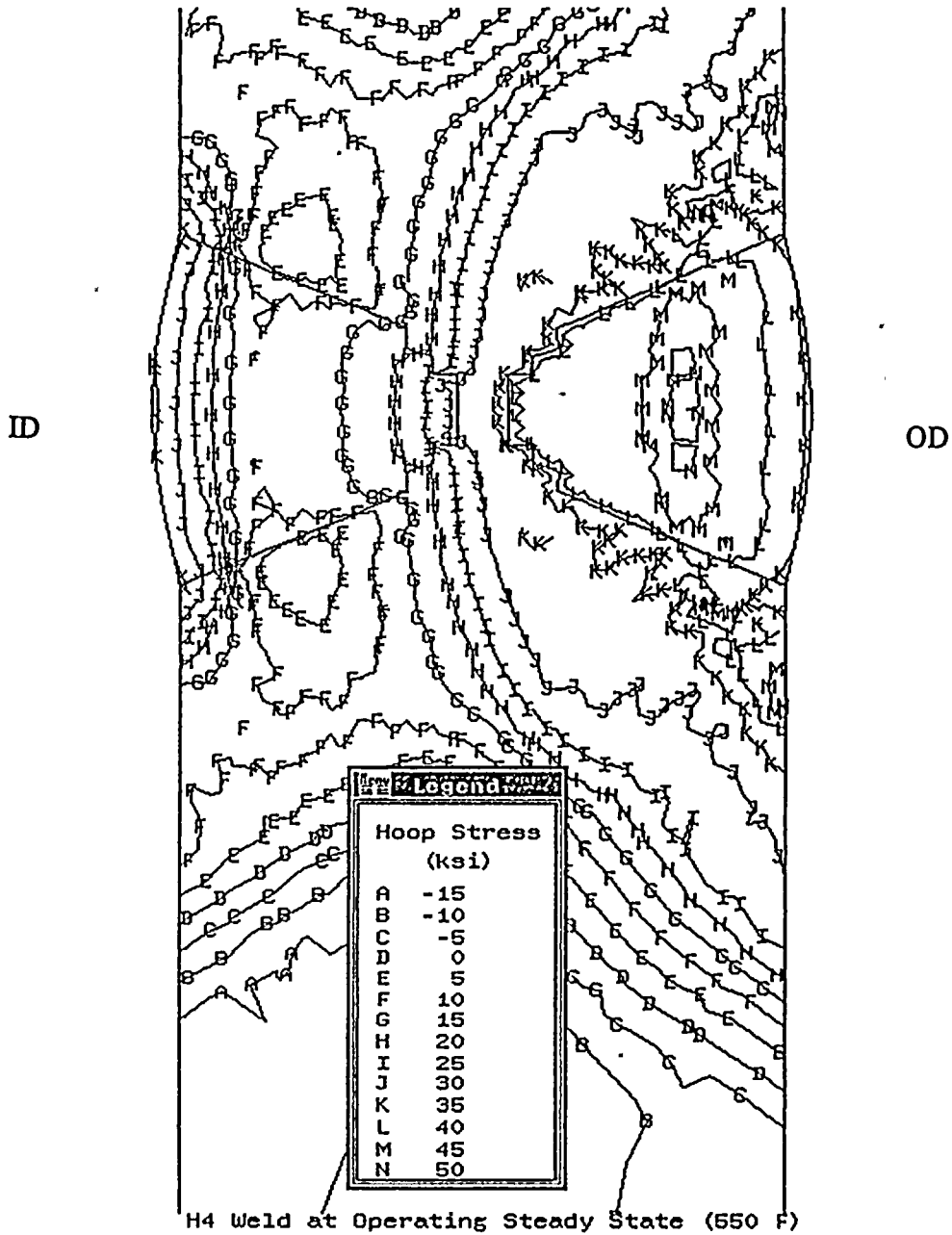


Figure 2-10 Hoop Stress Contours in the H4 Weld Region for Operating Conditions



1  
2  
3  
4  
5  
6  
7  
8  
9  
10  
11  
12  
13  
14  
15  
16  
17  
18  
19  
20  
21  
22  
23  
24  
25  
26  
27  
28  
29  
30  
31  
32  
33  
34  
35  
36  
37  
38  
39  
40  
41  
42  
43  
44  
45  
46  
47  
48  
49  
50  
51  
52  
53  
54  
55  
56  
57  
58  
59  
60  
61  
62  
63  
64  
65  
66  
67  
68  
69  
70  
71  
72  
73  
74  
75  
76  
77  
78  
79  
80  
81  
82  
83  
84  
85  
86  
87  
88  
89  
90  
91  
92  
93  
94  
95  
96  
97  
98  
99  
100



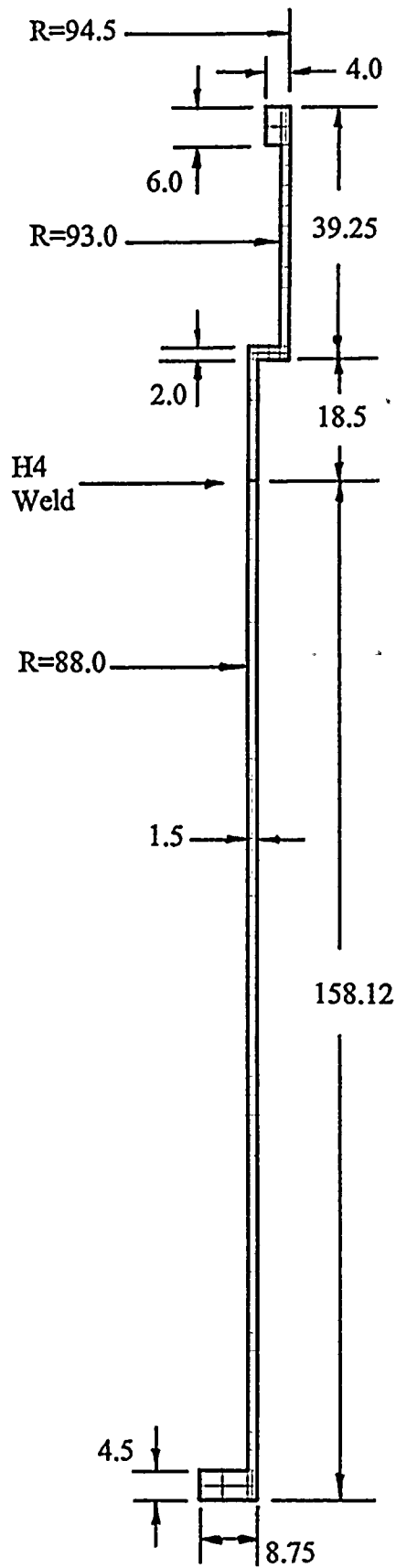
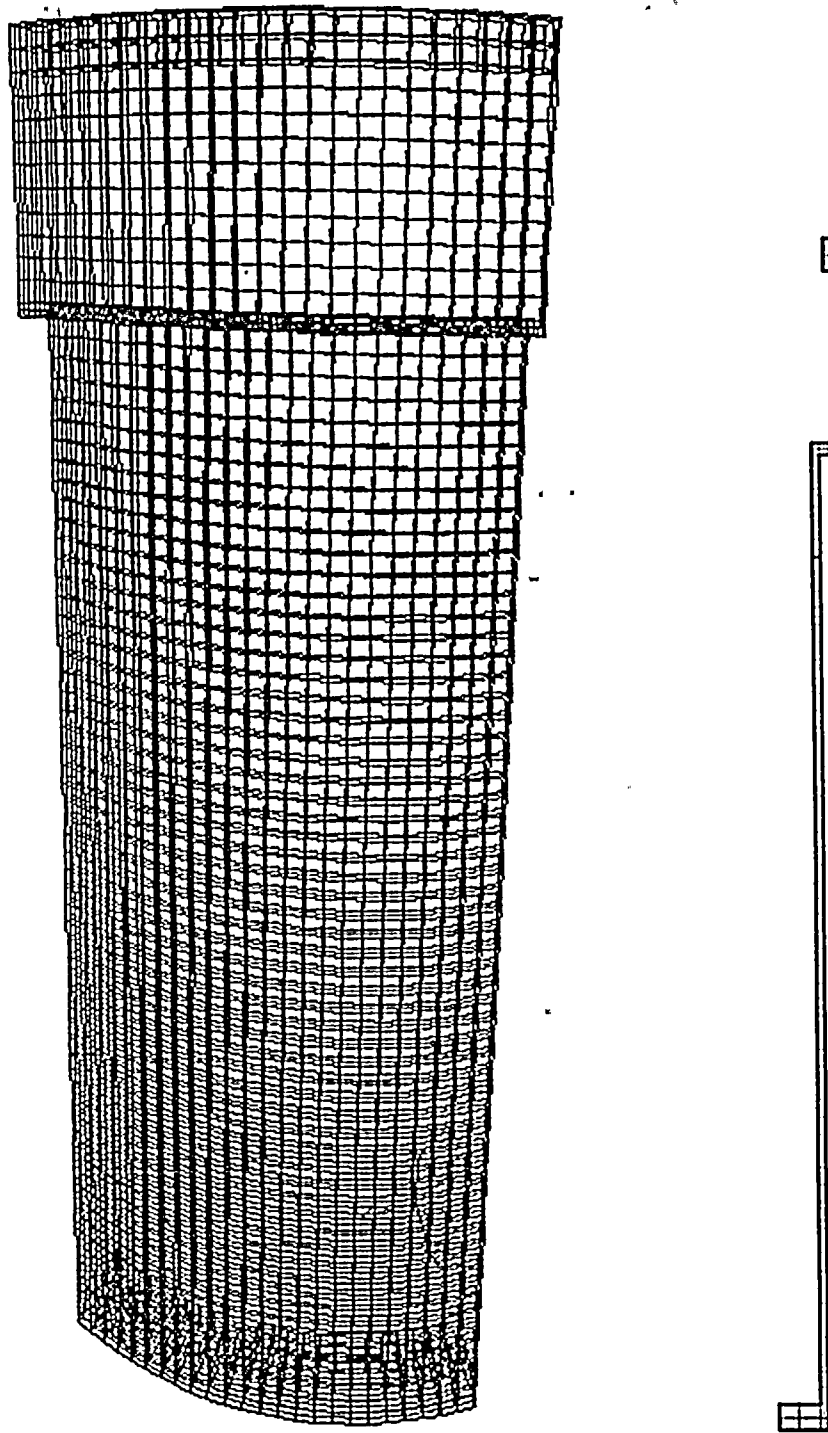


Figure 2-11 The 3D Finite Element Grid Used for the Axial Shrinkage Variation and Radial Mismatch (Ovality) Simulations





**Figure 2-12** A Perspective Plot of the 3D Finite Element Grid Used for the Axial Shrinkage Variation and Radial Mismatch (Ovality) Simulations



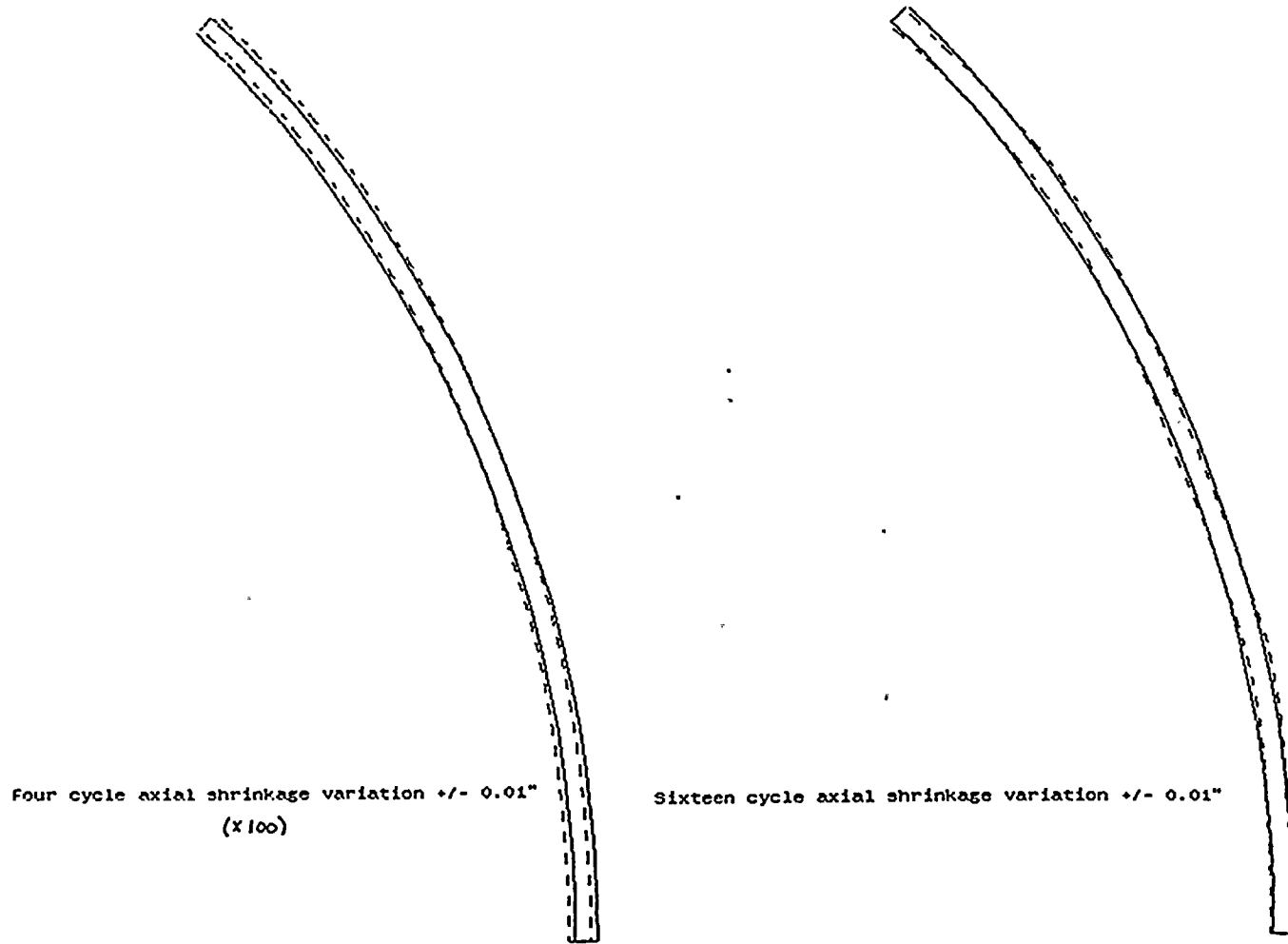
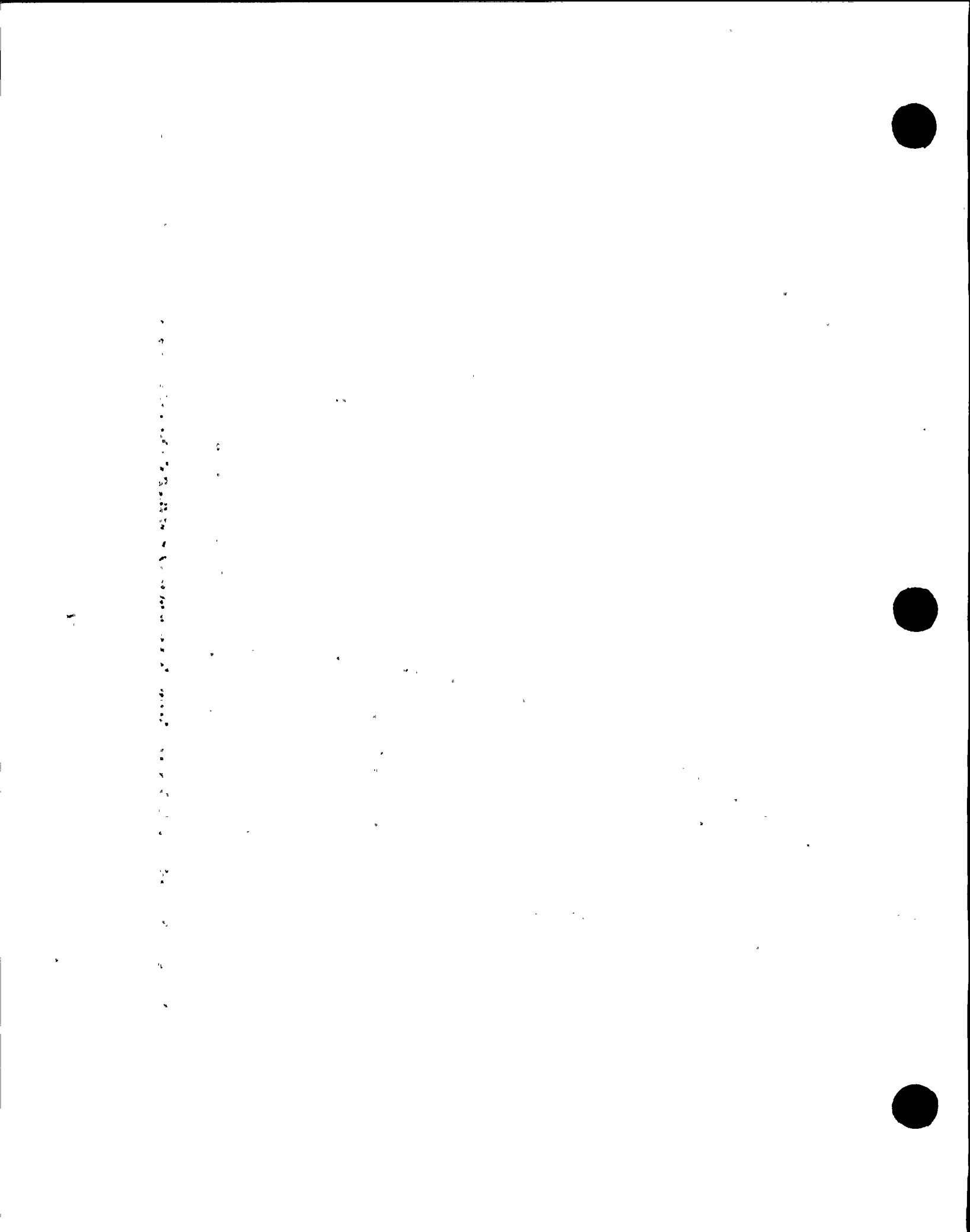


Figure 2-13 Example Deformed Shape Plots Showing the Radial Displacements at the H4 Weld for Two Sinusoidal Axial Shrinkage Variations



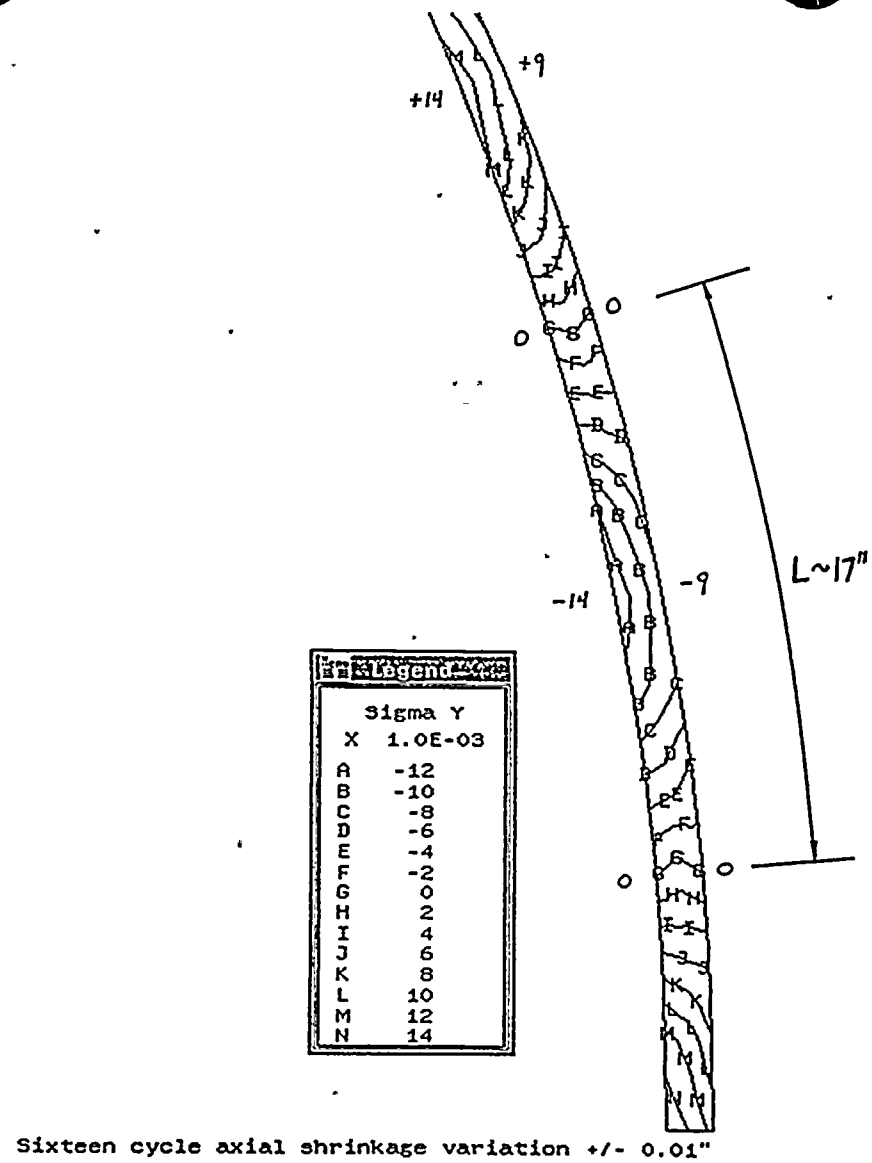
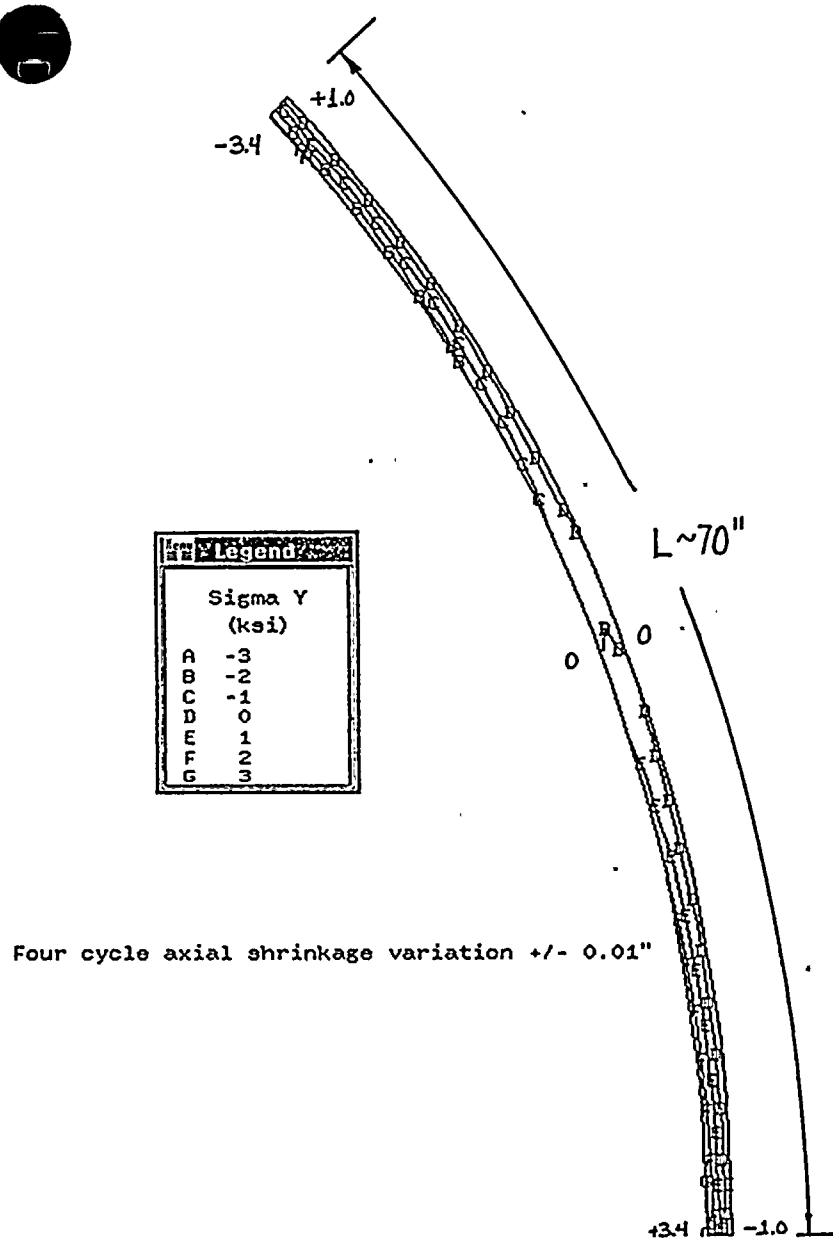
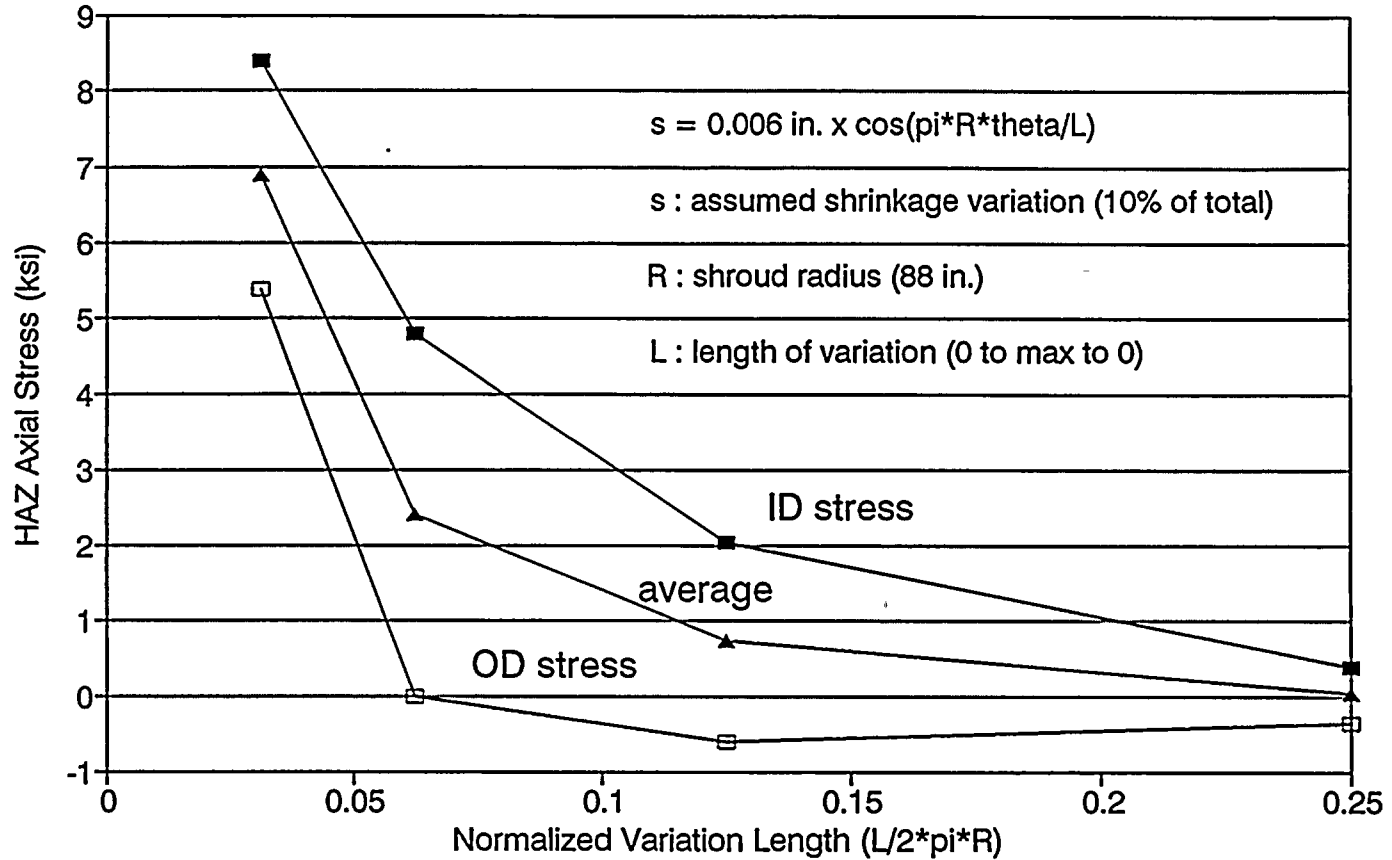


Figure 2-14 Example Axial Stress Contour Plots at the H4 Weld for Two Sinusoidal Axial Shrinkage Variations



## Effect of Variations in Weld Shrinkage on H4 HAZ Axial Stresses



**Figure 2-15 Summary of the Axial Stresses Induced by Several Assumed Circumferential Variations in the Axial Weld Shrinkage at the H4 Weld**



Vertical text or markings on the left side of the page, possibly bleed-through from the reverse side. The text is extremely faint and illegible.

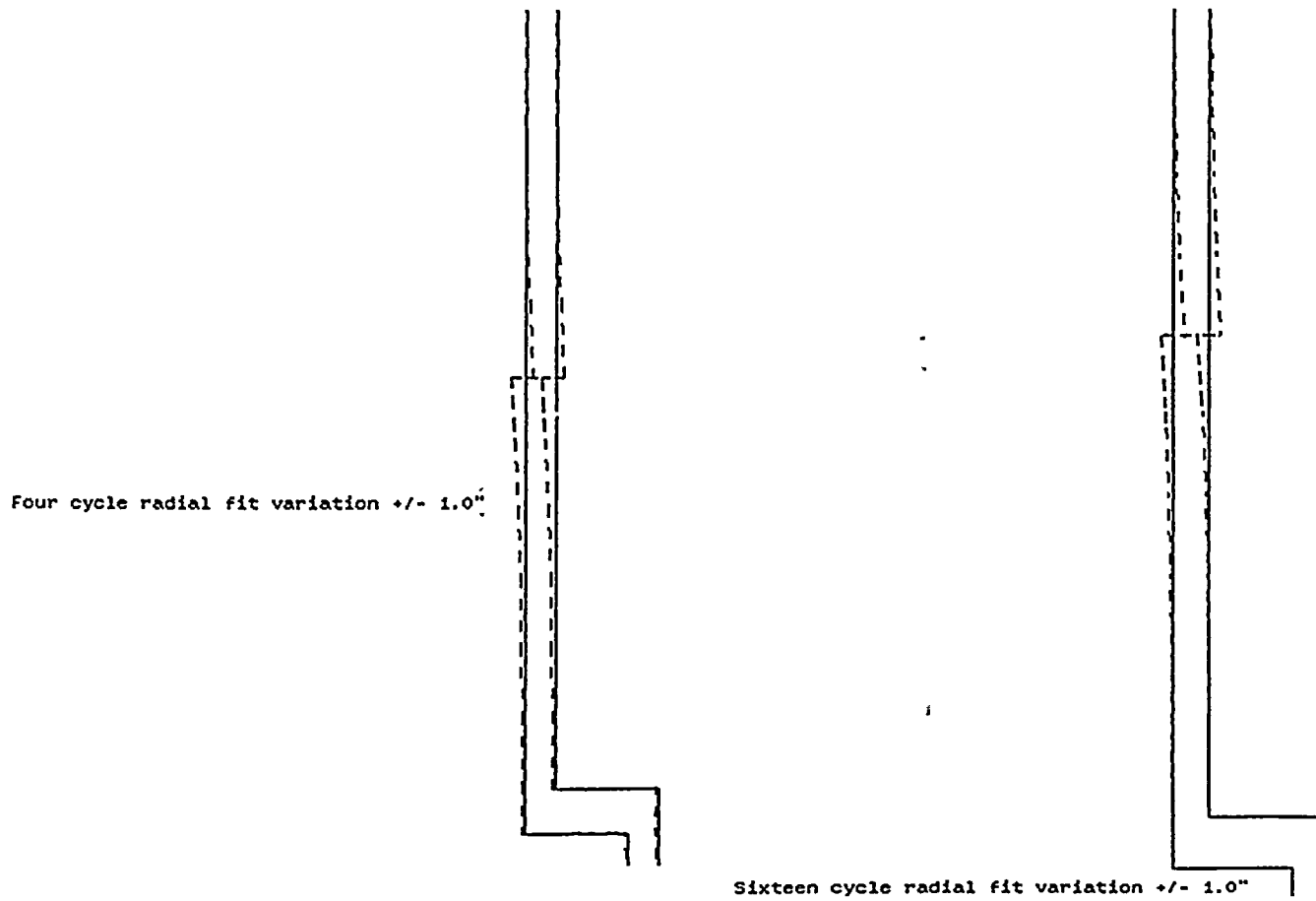


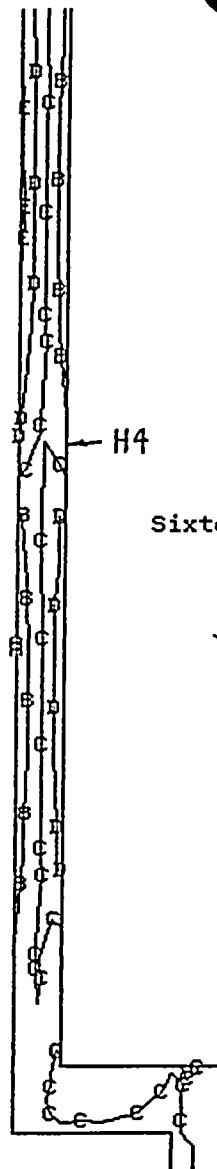
**Figure 2-16 Example Deformed Shape Plots Showing the Radial Displacements Across the H4 Weld for Two Sinusoidal Radial Mismatch Variations**



Vertical text or markings on the left side of the page, possibly bleed-through from the reverse side.

Four cycle radial fit variation +/- 1.0"

Legend	
Sigma Y (ksi)	
A	-80
B	-40
C	0
D	40
E	80



Sixteen cycle radial fit variation +/- 1.0"

Legend	
Sigma Y (ksi)	
A	-120
B	-80
C	-40
D	0
E	40
F	80
G	120

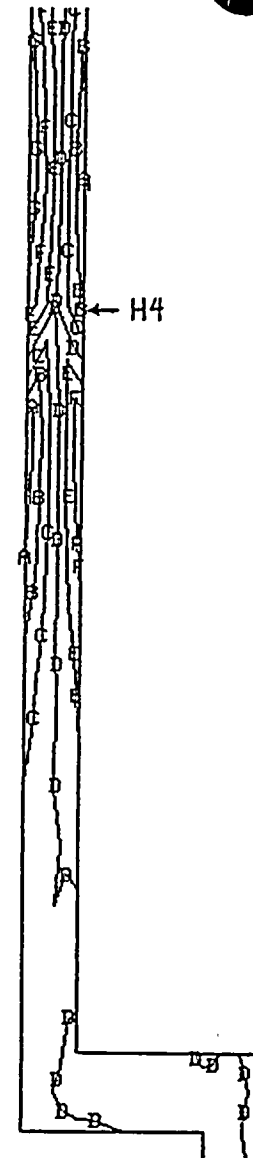


Figure 2-17 Example Axial Stress Contour Plots at the H4 Weld for Two Assumed Sinusoidal Radial Mismatch Variations



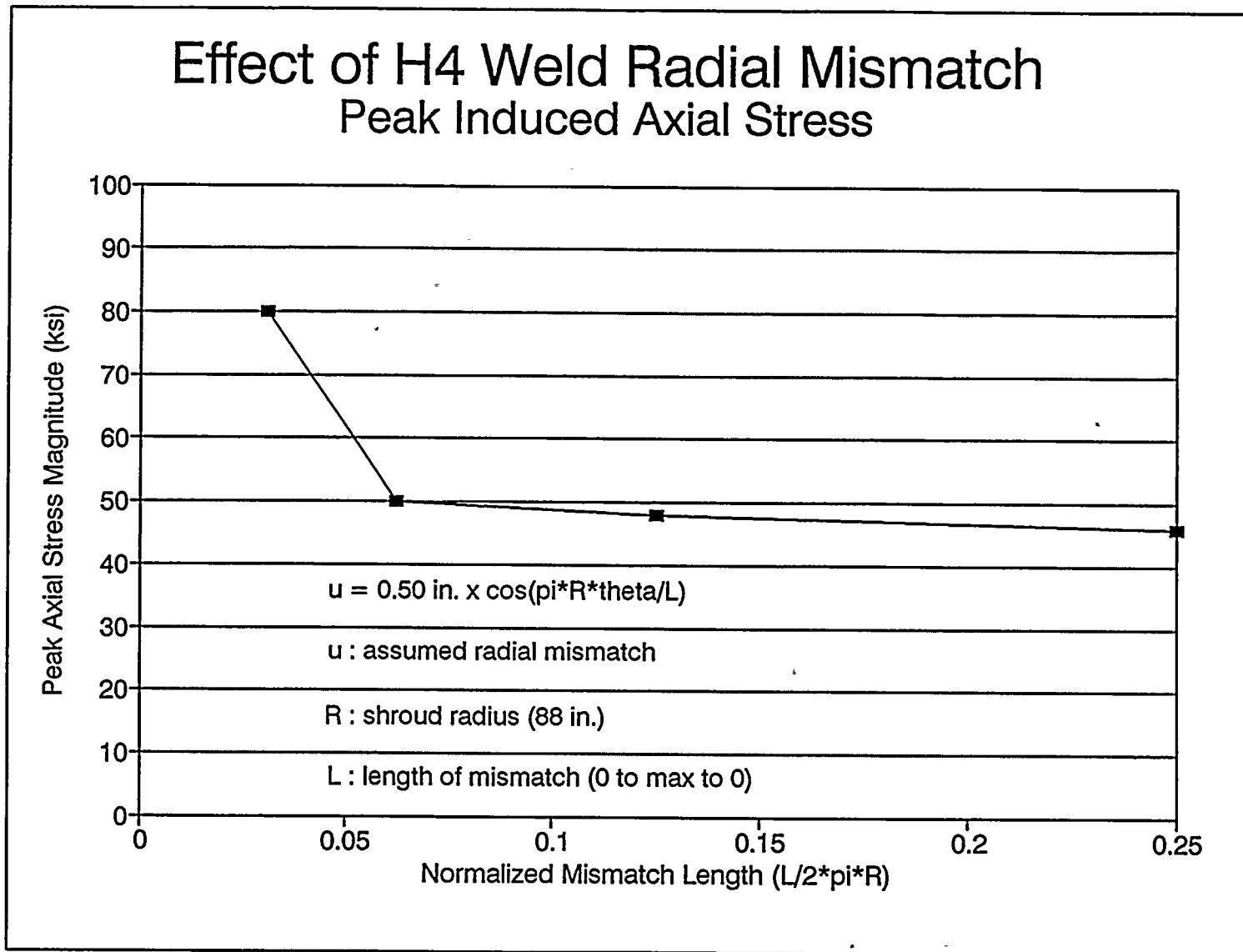


Figure 2-18 Summary of the Axial Stresses Induced by Several Assumed Circumferential Variations in the Initial Radial Mismatch at the H4 Weld



1  
2  
3  
4  
5  
6  
7  
8  
9  
10  
11  
12  
13  
14  
15  
16  
17  
18  
19  
20  
21  
22  
23  
24  
25  
26  
27  
28  
29  
30  
31  
32  
33  
34  
35  
36  
37  
38  
39  
40  
41  
42  
43  
44  
45  
46  
47  
48  
49  
50  
51  
52  
53  
54  
55  
56  
57  
58  
59  
60  
61  
62  
63  
64  
65  
66  
67  
68  
69  
70  
71  
72  
73  
74  
75  
76  
77  
78  
79  
80  
81  
82  
83  
84  
85  
86  
87  
88  
89  
90  
91  
92  
93  
94  
95  
96  
97  
98  
99  
100



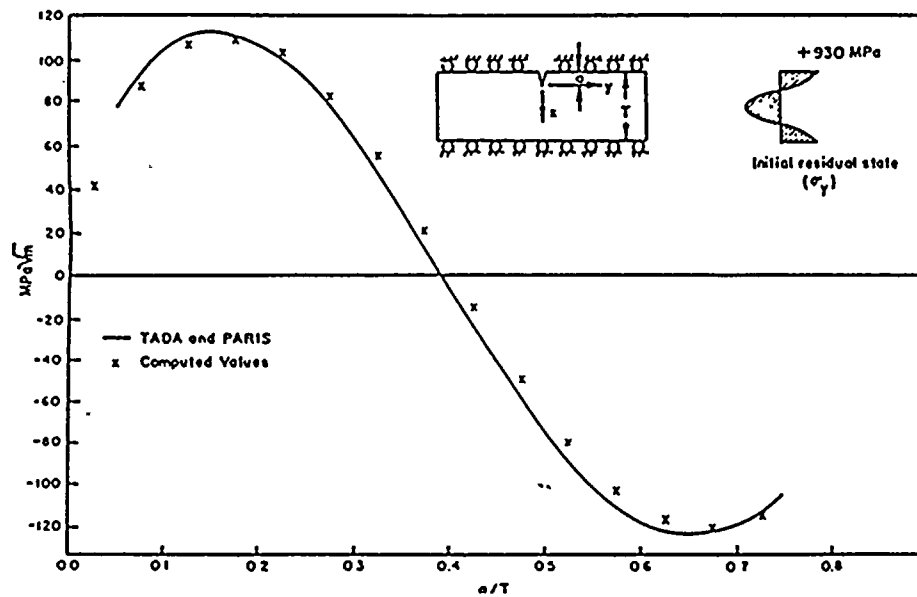
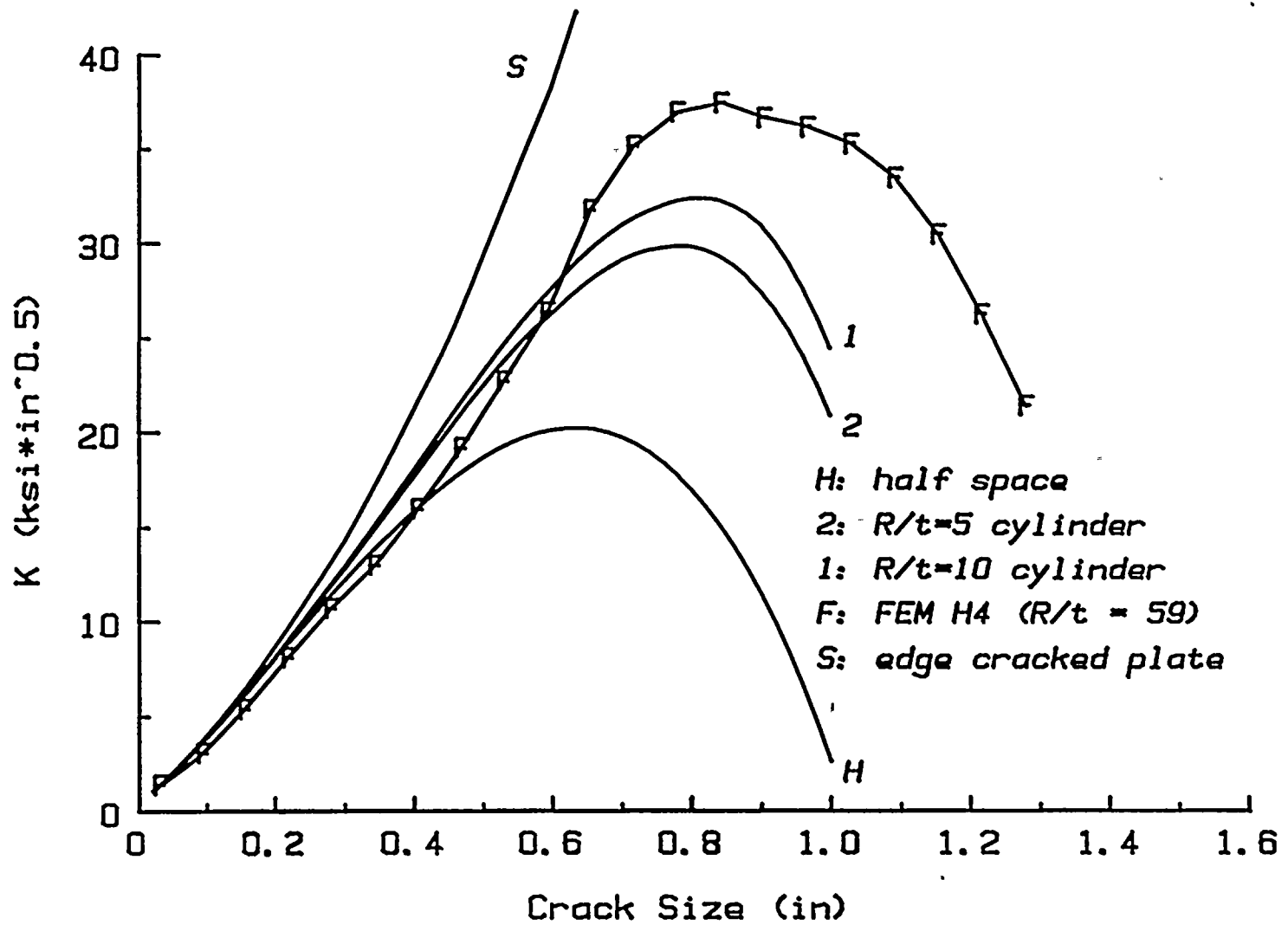


Figure 2-19 Illustration of the Accuracy That Can be Obtained Using the Finite Element Node Force Based Crack Closure Integral Method for Computing Stress Intensity Factors





Comparison of Geometries with H4 Operating Stresses

Figure 2-20 Comparison of the Finite Element Stress Intensity Factor Solution for an Outer Surface Crack at the H4 Weld With Standard Handbook Type Solutions



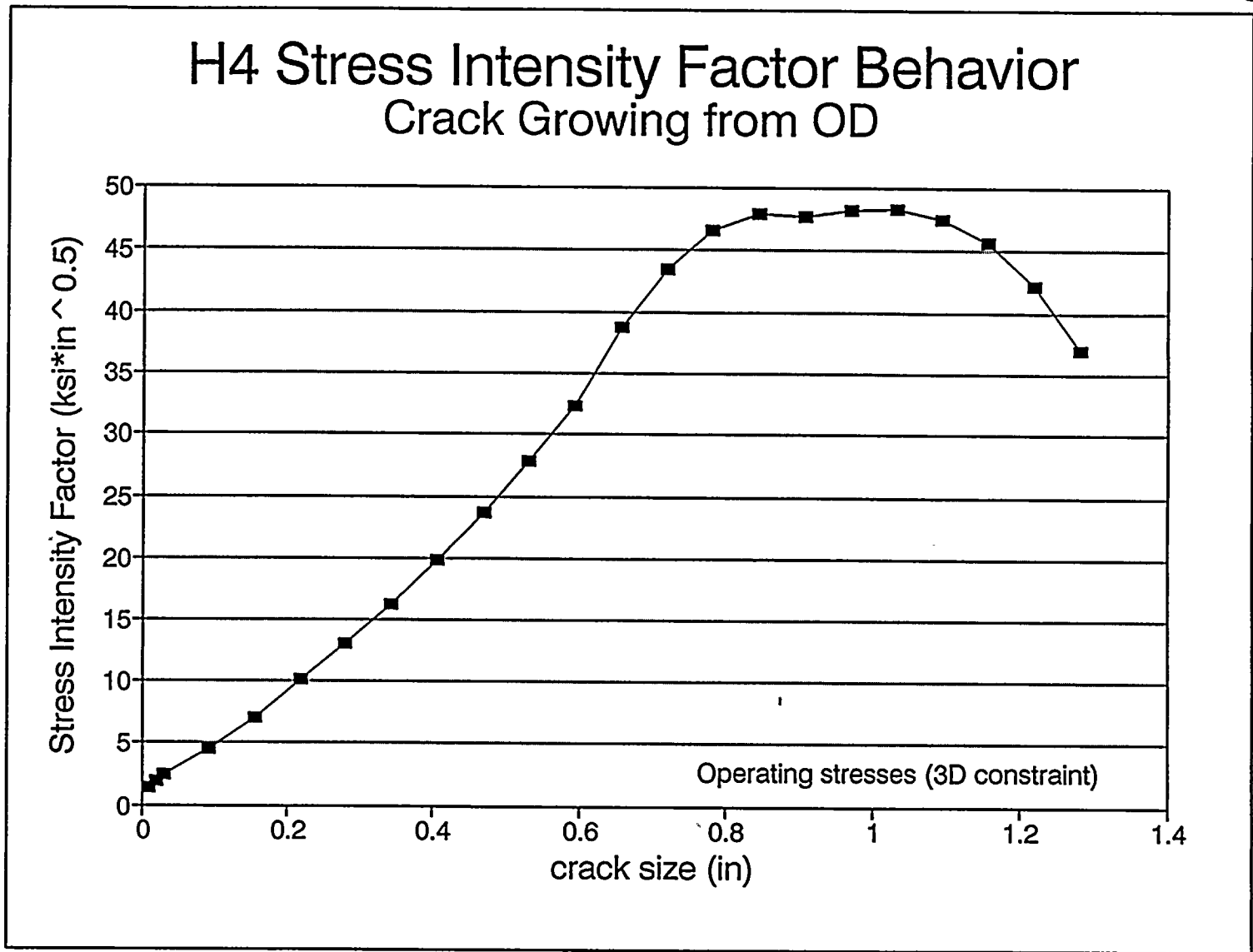


**Figure 2-21 The Stress Intensity Factor Solution for an OD Crack Growing in the H4 Weld HAZ With the Axisymmetric Welding Residual Stresses and Operating Conditions**



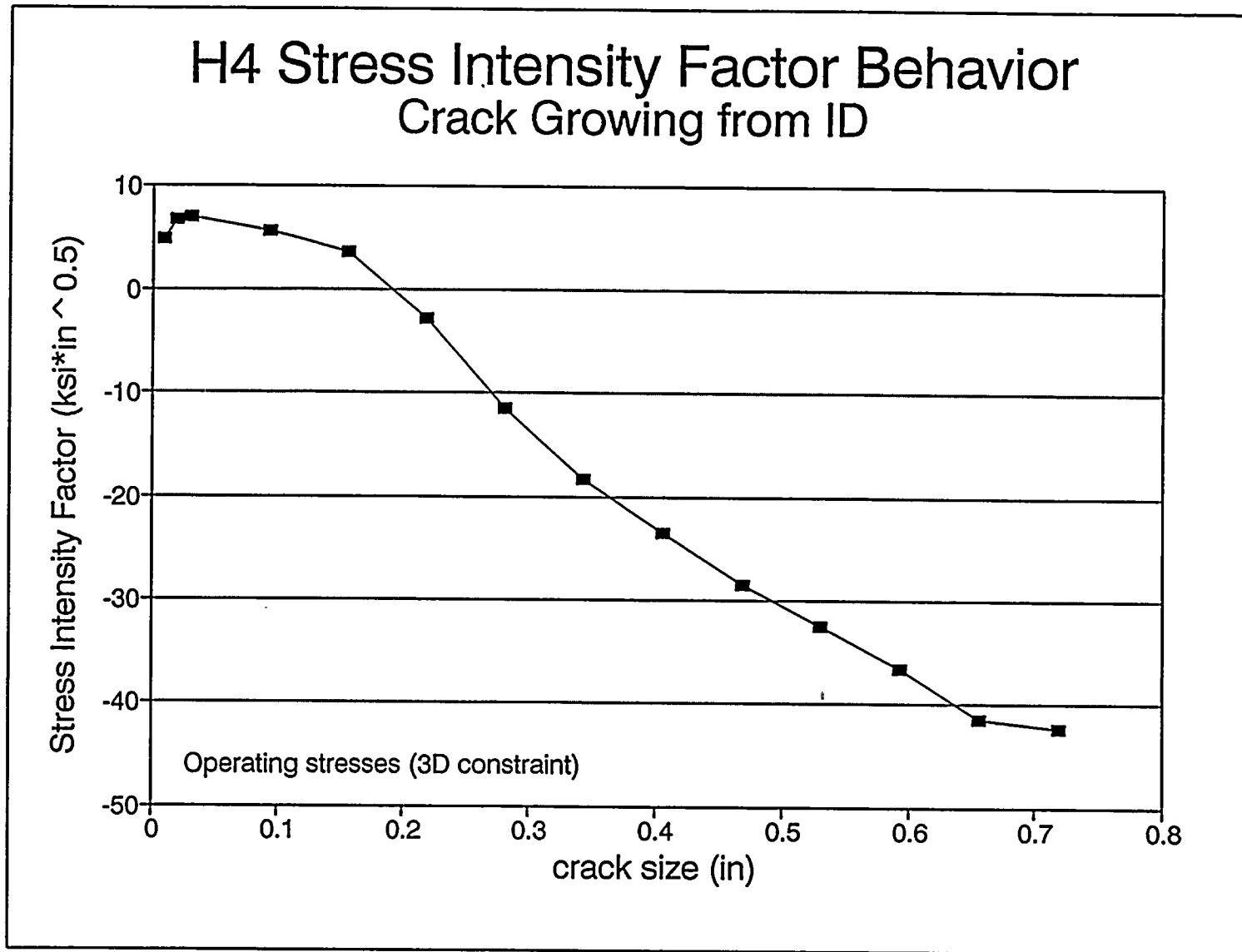


**Figure 2-22 The Stress Intensity Factor Solution for an ID Crack Growing in the H4 Weld HAZ With the Axisymmetric Welding Residual Stresses and Operating Conditions**



### 3.0 Crack Initiation Analysis

Analyses were performed to assess whether a postulated circumferentially oriented flaw (cracking in the R-θ plane) in the NMP-1 H4 weld is likely to initiate. The stress fields which were calculated and reported in Section 2 were used to calculate the applied stress intensity which was compared to the SCC threshold stress intensity factor ( $K_{ISCC}$ ).

#### 3.1 Threshold Stress Intensity Factor ( $K_{ISCC}$ )

There are numerous examples of  $K_{ISCC}$  measurements in aggressive water environments in the open literature. An example is given in Figure 3-1 which shows  $K_{ISCC}$  to be in the 8-10 ksi  $\sqrt{\text{in.}}$  range. However, few measurements of  $K_{ISCC}$  in typical BWR primary system water are available. Reference [Ma94] reports on measurements of  $K_{ISCC}$  for furnace sensitized 304 SS (649°C for 24 hours) which was tested in oxygenated water (4 ppm) at temperatures ranging from 252°C to 288°C. The conductivity ranged from 0.5  $\mu\text{S/cm}$  to 1.3  $\mu\text{S/cm}$  during these experiments. Experiments were conducted which made use of compact type specimens C(T) that had been modified to provide external surfaces that are isolated from the specimen, so that the current flowing between the crack and the external cathode could be readily monitored. This was done by coating the C(T) specimens with baked-on polytetrafluoroethylene (PTFE) so that only the crack (after fatigue precracking) was exposed to the environment. Cathodes were then mounted on the sides of the C(T) specimen and the current was monitored, using a zero resistance ammeter (ZRA) of conventional design, as the stress intensity and water chemistry were varied. Typical results are shown in Figure 3-2 which suggests that  $K_{ISCC}$  is between 10 ksi  $\sqrt{\text{in.}}$  and 20 ksi  $\sqrt{\text{in.}}$ . Based on the literature data, and the data given in Figure 3-2, we have taken  $K_{ISCC}$  to be 10 ksi  $\sqrt{\text{in.}}$ .

#### 3.2 Comparison of Applied Stress Intensity ( $K_I$ ) to $K_{ISCC}$

For the purpose of comparing the applied stress intensity ( $K_I$ ) to  $K_{ISCC}$  for shallow initial flaw depths, the half space solution was used:

$$K_I = 1.12 \sigma \sqrt{\pi a}$$

where

$\sigma$  = applied stress (ksi)  
 $a$  = flaw depth (in.)

Since the assumed initial flaw depths are small, the half space solution is judged to be a reasonable approximation for  $K_I$  near the ID and OD surfaces. As described in Section 2, the surface stresses at the ID and OD of H4 are:

	<u>Upper Bound</u>	<u>Best Estimate</u>
ID of H4	$\sigma_{ID} = 43.8 \text{ ksi}$	$\sigma_{ID} = 24 \pm 19.8$
OD of H4	$\sigma_{OD} = 23.7 \text{ ksi}$	$\sigma_{OD} = 6.9 \pm 16.8$



1. The first part of the document discusses the importance of maintaining accurate records of all transactions. This is essential for ensuring the integrity of the financial data and for providing a clear audit trail. The records should be kept in a secure and accessible location, and should be updated regularly to reflect any changes in the data.

2. The second part of the document describes the various methods used to collect and analyze the data. This includes the use of statistical techniques to identify trends and patterns in the data, as well as the use of computer software to automate the data collection and analysis process. The results of the analysis are then used to inform decision-making and to develop strategies for improving the organization's performance.

3. The third part of the document discusses the challenges faced in the process of data collection and analysis. These include the need for high-quality data, the complexity of the data, and the time and resources required to collect and analyze the data. Despite these challenges, the benefits of data collection and analysis are significant, and it is essential to overcome these challenges in order to realize the full potential of the data.



The components of the total surface stresses are shown in Table 3-1. The stresses after welding at operating temperature were calculated using an axisymmetric FEM model with 3D constraint to account for the fact that expansion of the weld region as the arc passes is more constrained in the actual 3D weld geometry than in the axisymmetric model. These stresses represent the best estimate of the mean stresses after welding. However, an important practical consideration is the circumferential variation due to non-axisymmetric aspects such as: weld start/stops, variations in weld groove width, and weld repairs. As discussed earlier, the magnitude of the effects of variations that affect the total transverse weld shrinkage increase with the frequency of variation around the circumference. Since these details are not available in the fabrication records, we have conservatively assumed the length of variation to be about 3% of the circumference (this corresponds to a stress zero to peak to zero separation distance of ~17 in.). Similarly, we have conservatively calculated the peak stress due to ovality during fabrication. The fabrication records indicate that the shroud cylinder near H4 was fabricated to within the ID specification of 176 ±0.5 in.. The peak stress at the H4 weld HAZ was determined by assuming that the largest diameter (176.5 in.) of the top cylinder was matched with the smallest diameter (175.5 in.) of the bottom cylinder. We postulated that the two cylinders were jacked into a round configuration and subsequently welded. The resulting peak stress is given in Table 3-1. This stress is believed to be conservative because the more likely scenario would have been that P.F. Avery matched the two largest diameters (since these met the specification) and minimized the need for jacking. This approach would have resulted in much less stress than for the case which was calculated.

The results of the applied stress intensity factor calculation are given in Figure 3-3. The flaw depth that results in 10 ksi √in. can be calculated as follows:

$$a = \frac{1}{\pi} \left( \frac{K_I}{1.12 \sigma} \right)^2$$

	<u>Upper Bound Stress</u>	<u>Mean Stress</u>
ID crack:	$a_{ID} = 0.013 \text{ in.}$	$a_{ID} = 0.044$
OD crack:	$a_{OD} = 0.045 \text{ in.}$	$a_{OD} = 0.533$

Since the plant records show that a dye penetrant inspection was performed on weld H4 during fabrication, it is unlikely that flaw depths exceed 0.01 in.. Since the OD flaw would have to be substantially greater than the upper bound for dye penetrant inspection (0.01 in.) for SCC crack initiation to occur, it is unlikely that a crack would initiate on the OD surface unless a flaw deeper than 0.010 in. went undetected. The only exception to this conclusion would be fabrication practices that induced higher OD surface stresses than those considered in the model, or other events, such as contaminant attack of the HAZ of the H4 weld which would lower  $K_{ISCC}$  from the assumed value of 10 ksi √in.. For a 0.01 in. flaw to initiate at the OD, assuming the upper bound stress level of 23.7 ksi,  $K_{ISCC}$  would have to be 4.7 ksi √in.. However, there is no indication in the NMP-1 plant records of any fabrication anomalies that would influence weld H4 crack initiation and no evidence of SCC attack due to contaminants prior to operation.



Nevertheless, the results of a recent inspection at Oyster Creek shows that OD cracks have initiated. Therefore, crack growth simulations were performed to assess the impact of OD initiated cracks on structural integrity (see Section 5).

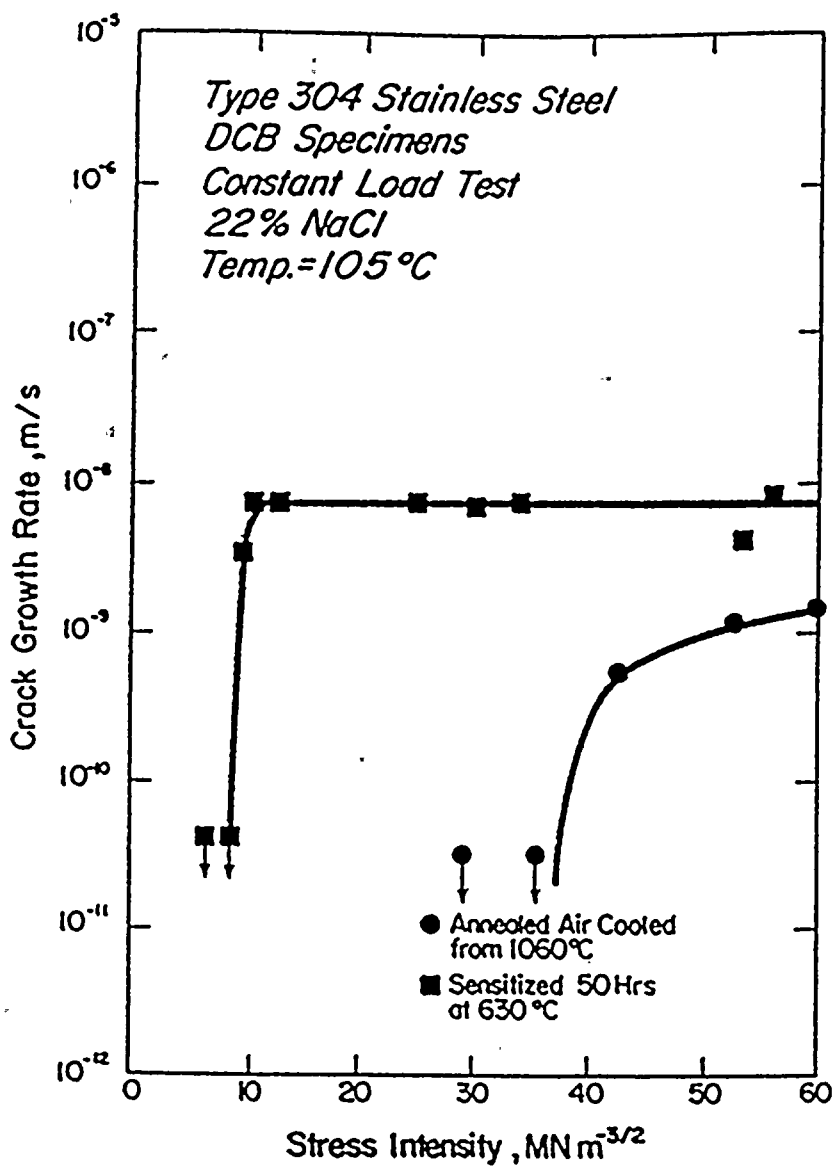
With regard to ID crack initiation, we conclude that there is a reasonable probability of ID initiation. Whether the applied  $K_I$  is above  $K_{ISCC}$  depends sensitively on the depth of postulated flaw. Therefore, to ensure that throughwall cracking will not occur through the end of cycle 11, crack growth calculations have been performed and these results are discussed in Section 5.



Table 3-1 Weld H4 HAZ Surface Stresses

Stress Contribution	Calculated Stress (ksi)	
	ID Surface	OD Surface
Stress After Welding at Operating Temperature	24.0	6.9
Peak Stress Due to Circumferential Variation in Transverse Weld Shrinkage	±8.4	±5.4
Peak Stress Due to Weld Groove Radial Mismatch During Fabrication	±11.4	±11.4
Total	4.2 to 43.8	-9.9 to 23.7





**Figure 3-1** Effect of Stress Intensity of Stress Corrosion Cracking (SCC) Velocity for Solution Annealed and Sensitized Type 304 SS in 22% NaCl Solution at 105°C [Sp81]



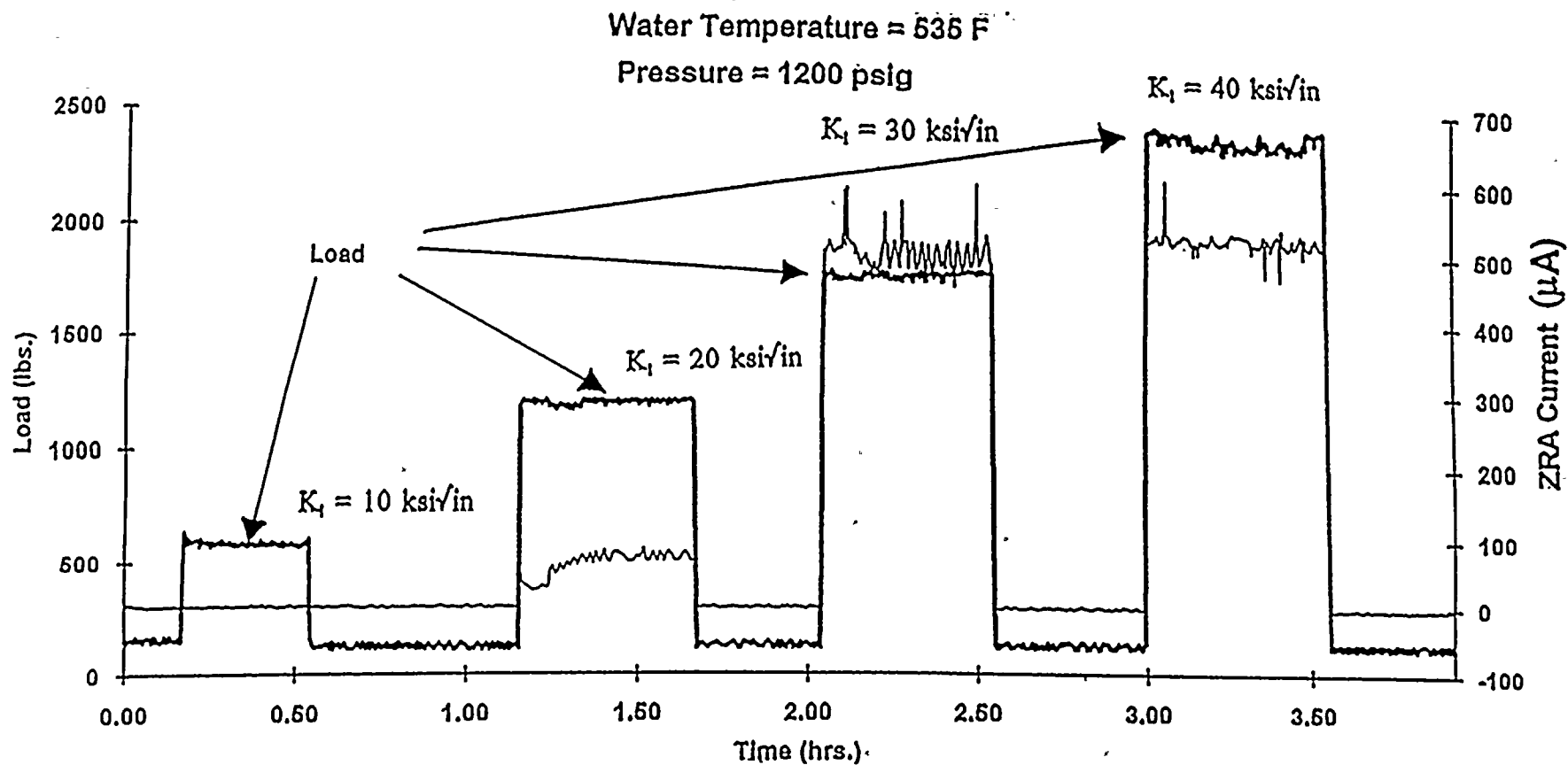


Figure 3-2 Load and ZRA Current Versus Time for Multiple Loading/Unloading Cycles to Various K<sub>1</sub> Levels



1954

1955

1956

1957

1958

1959

1960

1961

1962

1963

1964

1965

1966

1967

1968

1969

1970

1971

1972

1973

1974

1975

1976

1977

1978

1979

1980

1981

1982

1983

1984

1985

1986

1987

1988

1989

1990

1991

1992

1993

1994

1995

1996

1997

1998

1999

2000

2001

2002

2003

2004

2005

2006

2007

2008

2009

2010

2011

2012

2013

2014

2015

2016

2017

2018

2019

2020

2021

2022

2023

2024

2025



# COMPARISON OF APPLIED $K_I$ TO $K_{ISCC}$

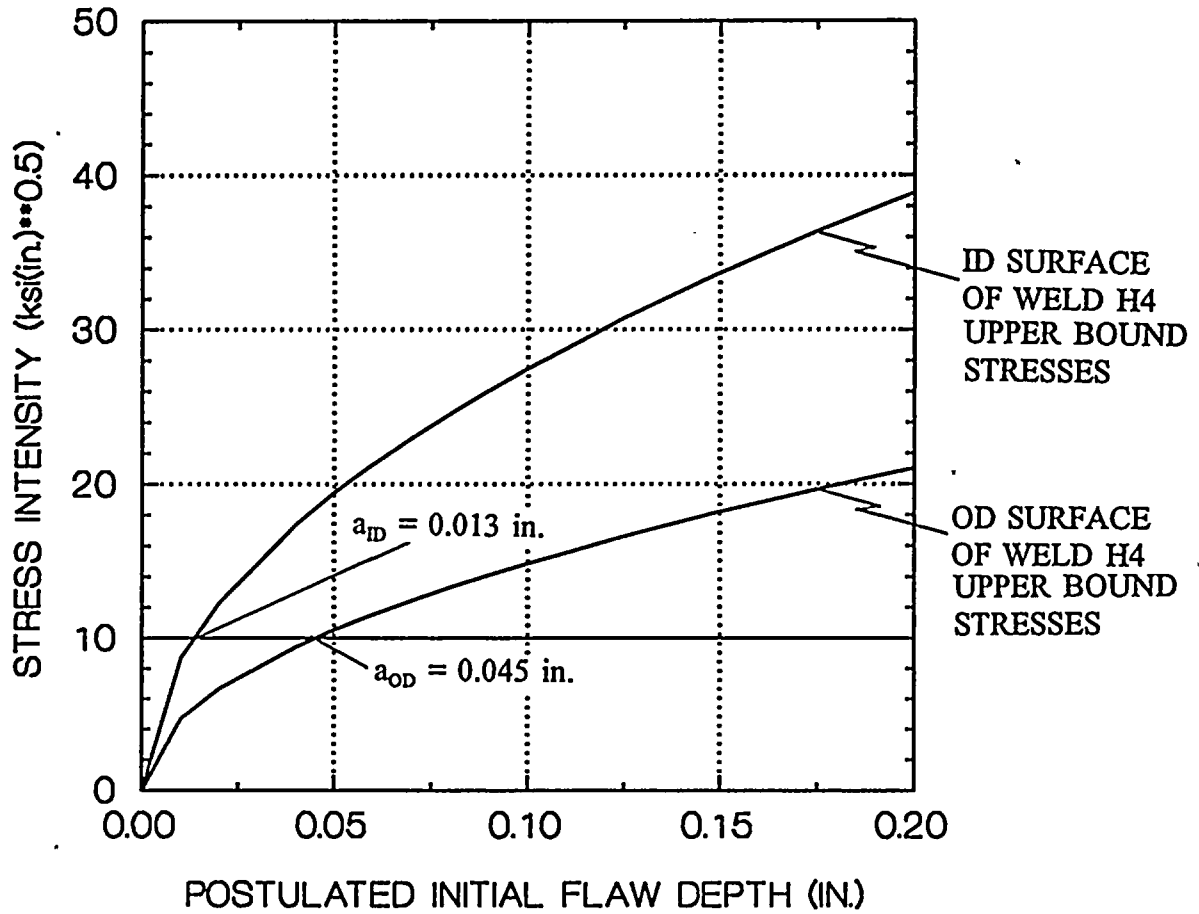


Figure 3-3 Comparison of Applied  $K_I$  to  $K_{ISCC} = 10$  ksi√in. for ID and OD of Weld H4 Assuming Upper Bound Stresses



## 4.0 Fluence at H4 Weld

Analyses were performed to determine the peak fast neutron fluence ( $E > 1\text{MeV}$ ) at the NMP-1 shroud weld H4 at the end of cycle 11 and to characterize the azimuthal variation of the fluence. These fluences were compared with the GE irradiation assisted stress corrosion cracking (IASCC) threshold fluences given in Reference [Ca94] to determine if radiation effects in the base material and/or weld HAZ are expected to affect crack initiation and/or crack growth.

### 4.1 Fluence Characterization

Discrete Ordinates Transport (DOT) calculations have been performed for NMP-1 and Oyster Creek as part of the pressure vessel surveillance capsule analysis for these plants. The results of these calculations are reported in References [Ma85] and [St84]. The internal vessel structures and model geometry used in these calculations are shown in Figures 4-1 and 4-2. As a result of octally symmetric fuel loading, transport calculations were performed in the first octant which is measured from the defined plant  $0^\circ$  line. The internal geometric arrangement for the two plants is very similar with one notable exception: Oyster Creek has more peripheral bundles in the  $30^\circ$  to  $60^\circ$  azimuthal region. This results in a higher peak flux for Oyster Creek at the vessel wall ID surface as shown in Figure 4-3. The Oyster Creek flux is approximately 1.36 times higher than the NMP-1 flux at the vessel ID surface. Also, the Oyster Creek vessel surface flux peaks at  $43.5^\circ$  as compared with that at NMP-1 which peaks at  $15.6^\circ$ .

The NMP-1 DOT output (Reference [Bat84]) was used to determine the peak flux, the azimuthal variation of flux, and the fluence at the NMP-1 shroud H4 weld. The data given in Reference [In94] indicate that the axial peaking at H4 is only  $\approx 2\%$  higher than the core average power (which corresponds to the location where the R- $\theta$  transport calculation was performed). Therefore, the R- $\theta$  transport data were multiplied by 1.02 to obtain the flux at weld H4. This approach is expected to provide a reasonable approximation of an R-Z transport calculation, particularly since the axial power variation near the top of the active fuel is not large and the distance from the outer bundle to the shroud ID surface is relatively short. The flux and fluence data at the end of cycle 11 are summarized in Table 4-1, and plots are provided in Figures 4-4 and 4-5. The flux distribution through the shroud at weld H4 is given in Table 4-2 at the peak flux angle. The flux at the shroud ID surface is roughly twice that at the OD surface.

The Reference [Wa94] letter reported GE estimates of the flux at several NMP-1 shroud welds. Since GE did not have access to plant-specific transport data, they scaled the KKM reactor shroud flux to obtain the estimate of the NMP-1 peak flux of  $1.0 \times 10^{12}$  n/cm<sup>2</sup>/sec. This flux was then adjusted according to the Peach Bottom 2 axial profile to obtain the estimated H4 ID surface flux of  $7.8 \times 10^{11}$  n/cm<sup>2</sup>/sec. This estimate by GE is in good agreement with the Battelle DOT shroud mid-wall results (Table 4-2) which were calculated on a plant-specific basis.

### 4.2 Fluence Effects on Crack Behavior

Reference [Ca94] indicates that GE has concluded that a fluence effect on cracking susceptibility (IASCC) can occur at fluences above the range of  $3.0\text{-}5.0 \times 10^{20}$  n/cm<sup>2</sup> for 304 SS. Part of the justification for the GE defined fluence threshold is given in Figure 4-6. GE also

1. The first part of the document discusses the importance of maintaining accurate records of all transactions. It emphasizes that proper record-keeping is essential for the integrity of the financial system and for the ability to detect and prevent fraud.

2. The second part of the document outlines the various methods used to collect and analyze data. It describes the use of statistical techniques to identify trends and anomalies in the data, and the importance of using reliable sources of information.

3. The third part of the document discusses the role of the auditor in the process. It highlights the need for the auditor to maintain independence and objectivity, and to follow established standards and procedures in conducting the audit.

4. The fourth part of the document discusses the importance of communication in the audit process. It emphasizes the need for the auditor to communicate clearly and effectively with the client, and to provide a clear and concise report of the findings of the audit.

5. The fifth part of the document discusses the importance of the audit process in the overall financial system. It highlights the role of the audit in providing assurance to investors and other stakeholders, and in promoting the transparency and accountability of the financial system.

noted in [Ca94] that a synergistic interaction of fluence and intergranular stress corrosion cracking (IGSCC) in sensitized 304 SS material is expected at fluences above about  $1 \times 10^{19}$  n/cm<sup>2</sup>. We conclude from the plant-specific transport data that IASCC is not a significant concern (through the end of cycle 11) for the non-sensitized regions of the NMP-1 shroud near weld H4 since the fluences at the shroud in the beltline region will not exceed the GE defined IASCC threshold over large azimuthal regions. Even if IASCC initiation had occurred after ~10 effective full power years (EFPY) in localized regions, there would not be significant crack extension through the end of cycle 11.

In light of the GE information reported in [Ca94], the sensitized HAZ material near weld H4 may experience fluence effects which would increase the crack growth rate. This effect must be accounted for in the crack growth model. GE indicates that sensitized 304 SS may experience fluence effects at relatively low fast neutron fluences ( $\sim 1 \times 10^{19}$  n/cm<sup>2</sup>) based on electrochemical potentiokinetic reactivation (EPR) data [Ca94]. EPR data is used to measure the degree of sensitization (DOS). As shown in Reference [Ca94], there is an upward trend in EPR with increase in fluence for fluences above  $\sim 1 \times 10^{19}$  n/cm<sup>2</sup>. However, for fluences less than approximately  $5 \times 10^{20}$  n/cm<sup>2</sup>, the effect of neutron fluence on EPR is not significant. In particular, assuming the GE data trend is applicable to the sensitized NMP-1 H4 weld material, the EPR at the end of cycle 11 is expected to rise to only 18 C/cm<sup>2</sup> from the estimated unirradiated value of 15 C/cm<sup>2</sup>. Nevertheless, this effect will be accounted for in the plant-specific crack growth rate since crack growth data in sensitized 304 SS which was measured in the core and recirculation line at NMP-1 have been used in the model development. Further details on the crack growth model are given in Section 5.



**Table 4-1 Flux and Fluence at the End of Cycle 11 at NMP-1 Shroud Weld H4**

<b>Azimuthal Angle (Degrees)</b>	<b>Flux (n/cm<sup>2</sup>/sec)</b>	<b>Fluence at the End of Cycle 11<sup>a</sup> (n/cm<sup>2</sup>)</b>
1.74	3.8352x10 <sup>11</sup>	1.8462x10 <sup>20</sup>
5.22	4.3452x10 <sup>11</sup>	2.0910x10 <sup>20</sup>
8.70	5.1816x10 <sup>11</sup>	2.4990x10 <sup>20</sup>
12.18	6.0282x10 <sup>11</sup>	2.9070x10 <sup>20</sup>
15.66	7.3440x10 <sup>11</sup>	3.5394x10 <sup>20</sup>
19.14	7.4154x10 <sup>11</sup>	3.5700x10 <sup>20</sup>
22.35	5.6610x10 <sup>11</sup>	2.7234x10 <sup>20</sup>
25.04	4.5492x10 <sup>11</sup>	2.1930x10 <sup>20</sup>
27.28	3.6822x10 <sup>11</sup>	1.7748x10 <sup>20</sup>
29.15	2.9886x10 <sup>11</sup>	1.4382x10 <sup>20</sup>
30.85	2.4786x10 <sup>11</sup>	1.1934x10 <sup>20</sup>
32.72	2.1012x10 <sup>11</sup>	1.0118x10 <sup>20</sup>
34.96	1.7136x10 <sup>11</sup>	8.2722x10 <sup>19</sup>
37.65	1.4994x10 <sup>11</sup>	7.2216x10 <sup>19</sup>
40.59	1.3464x10 <sup>11</sup>	6.5076x10 <sup>19</sup>
43.53	1.3056x10 <sup>11</sup>	6.2934x10 <sup>19</sup>

a) Fluence calculated through the end of cycle 11 (15.28 EFPY)



1. The first part of the document discusses the importance of maintaining accurate records of all transactions. It emphasizes that this is essential for ensuring the integrity of the financial statements and for providing a clear audit trail.

2. The second part of the document outlines the various methods used to collect and analyze data. It describes how different types of information are gathered and how they are processed to identify trends and anomalies.

3. The third part of the document focuses on the results of the analysis. It presents the findings in a clear and concise manner, highlighting the key areas of concern and the recommended actions to address them.

4. The final part of the document provides a summary of the overall findings and conclusions. It reiterates the importance of ongoing monitoring and the need for continuous improvement in the data collection and analysis process.



**Table 4-2 Flux Distribution Through Shroud Weld H4 at Peak Flux Azimuthal Position**

<b>Radial Position (R) Measured From Shroud ID Normalized by Shroud Thickness (t) (R/t)</b>	<b>Peak Flux at H4 Weld (n/cm<sup>2</sup>/sec)</b>
0	9.14x10 <sup>11</sup>
0.17	8.73x10 <sup>11</sup>
0.50	7.34x10 <sup>11</sup>
0.83	5.55x10 <sup>11</sup>
1.0	4.92x10 <sup>11</sup>



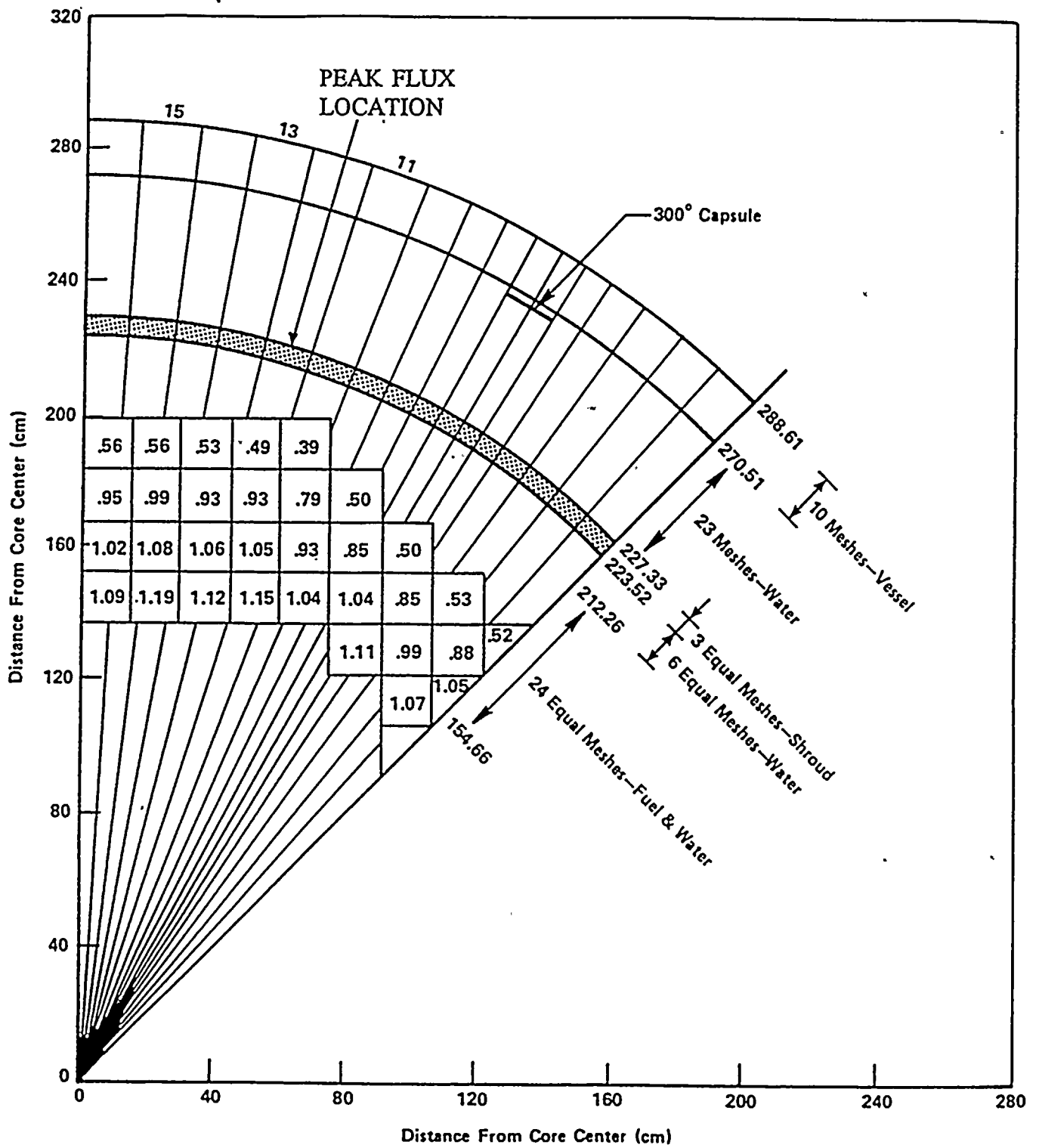


Figure 4-1 Nine Mile Point Unit 1 Internal Vessel Structures and Vessel Wall Geometry Used in Neutron Transport Calculation [St84]



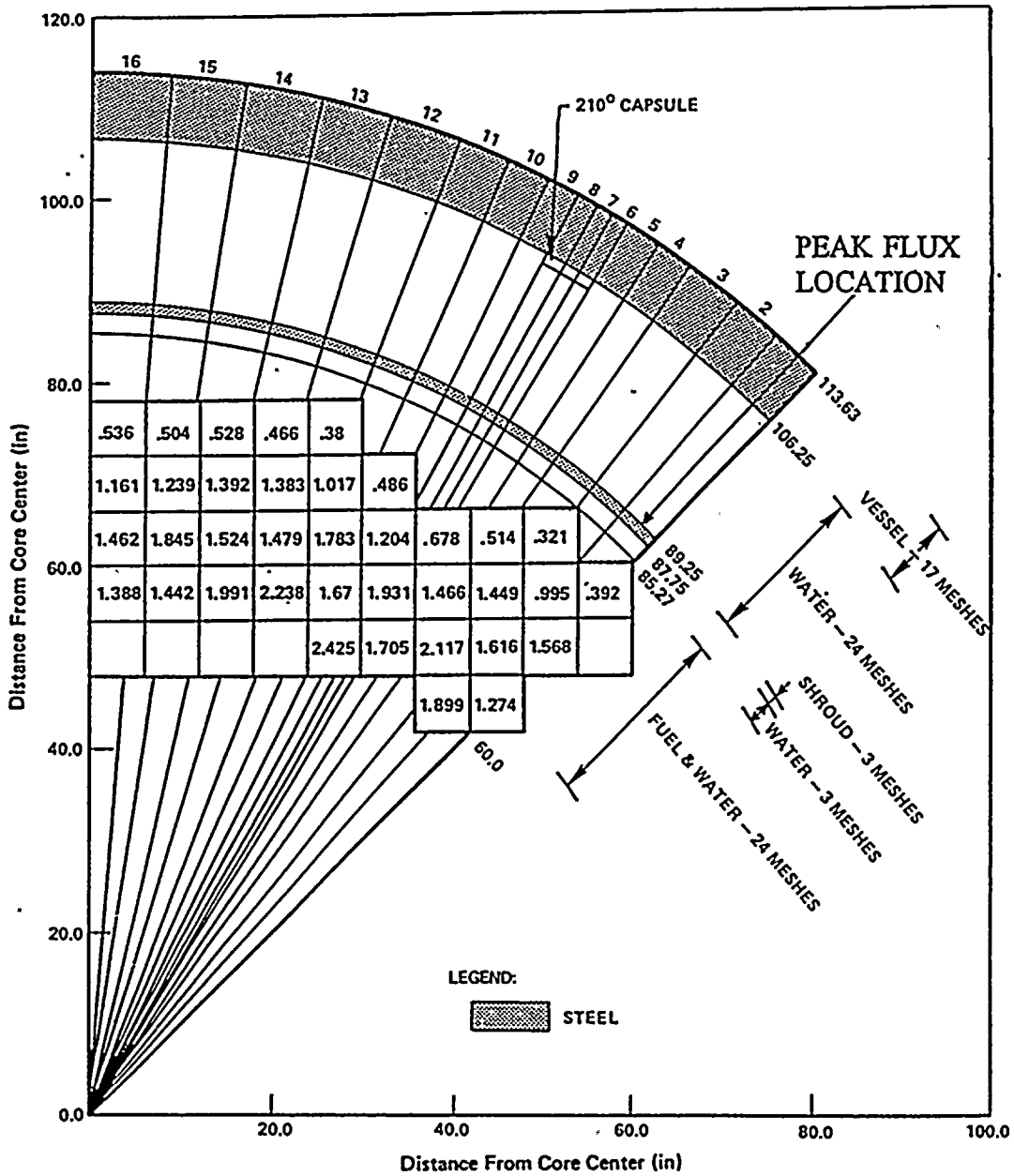


Figure 4-2 Oyster Creek Internal Vessel Structures and Vessel Wall Geometry Used in Neutron Transport Calculation [Ma85]



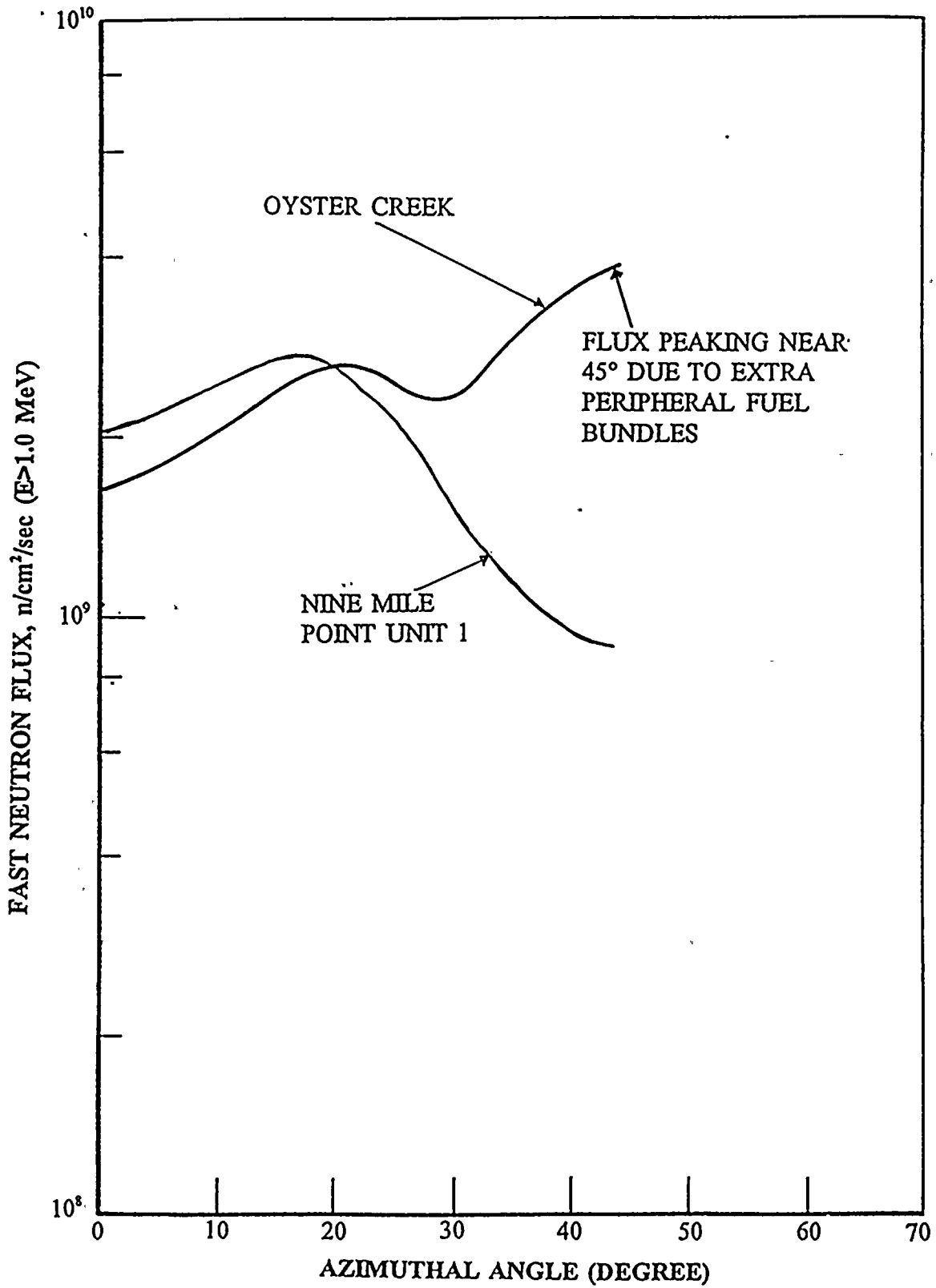


Figure 4-3 Flux at Pressure Vessel Inner Wall Surface as a Function of Azimuthal Angle for Nine Mile Point Unit 1 and Oyster Creek [Data From [Ma85 and St84]]



# Nine Mile Point Unit 1 Flux at Shroud Weld H4

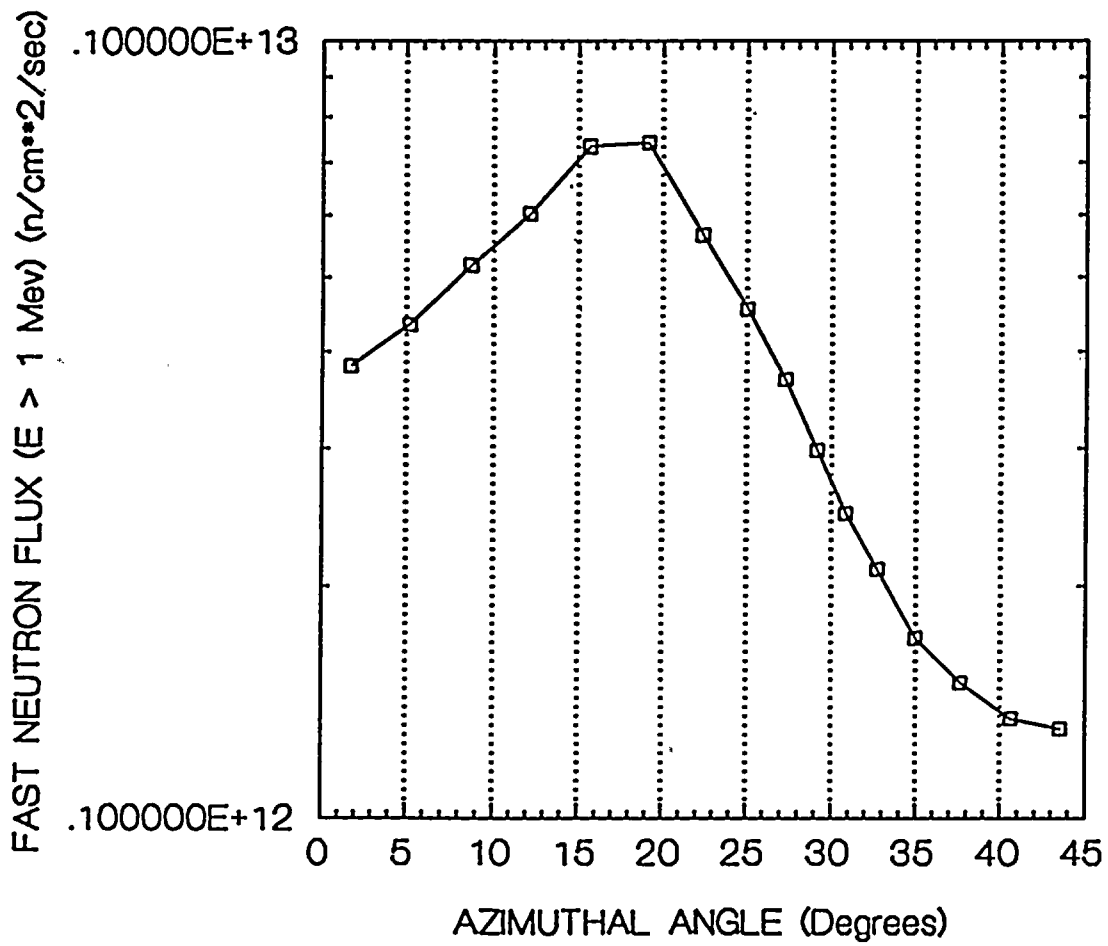


Figure 4-4 Azimuthal Variation of Flux at NMP-1 Shroud Weld H4



# Nine Mile Point Unit 1 Fluence at Shroud Weld H4

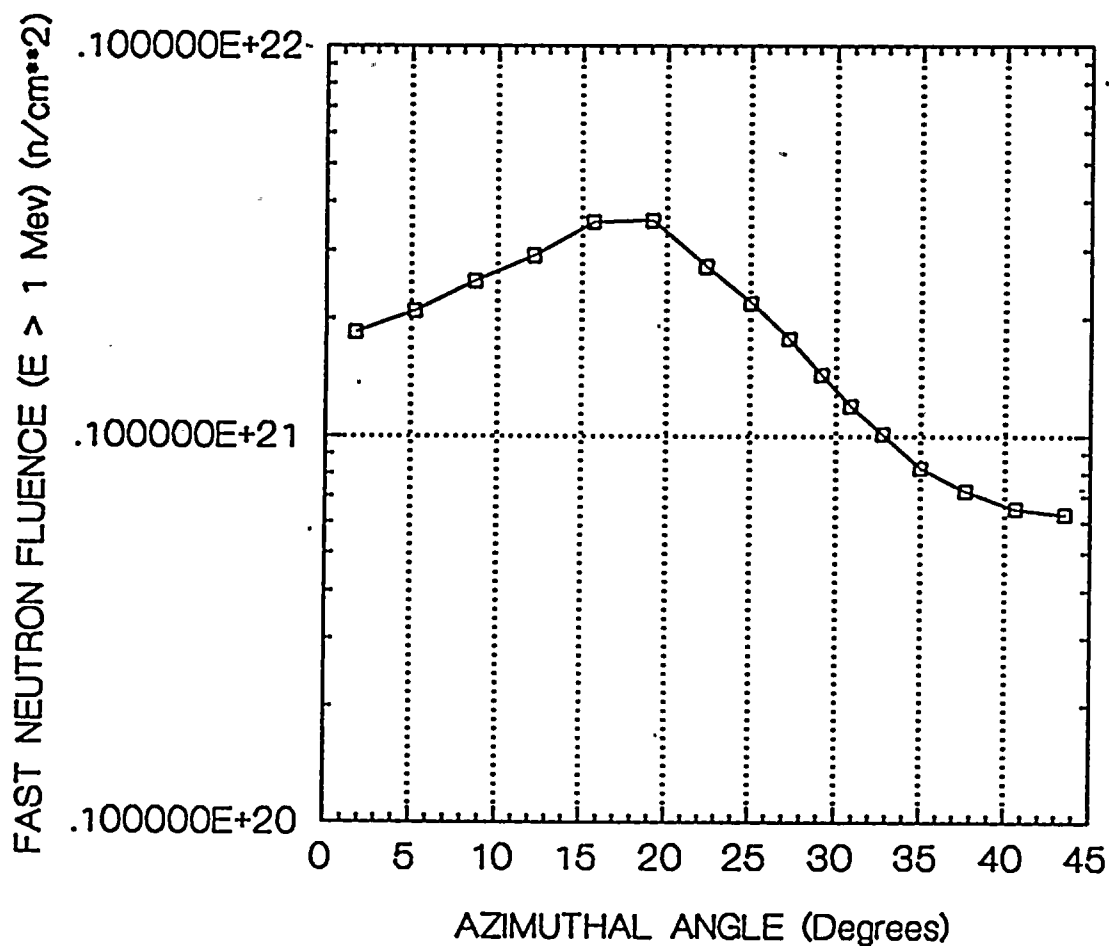


Figure 4-5 Azimuthal Variation of Fluence at NMP-1 Shroud Weld H4



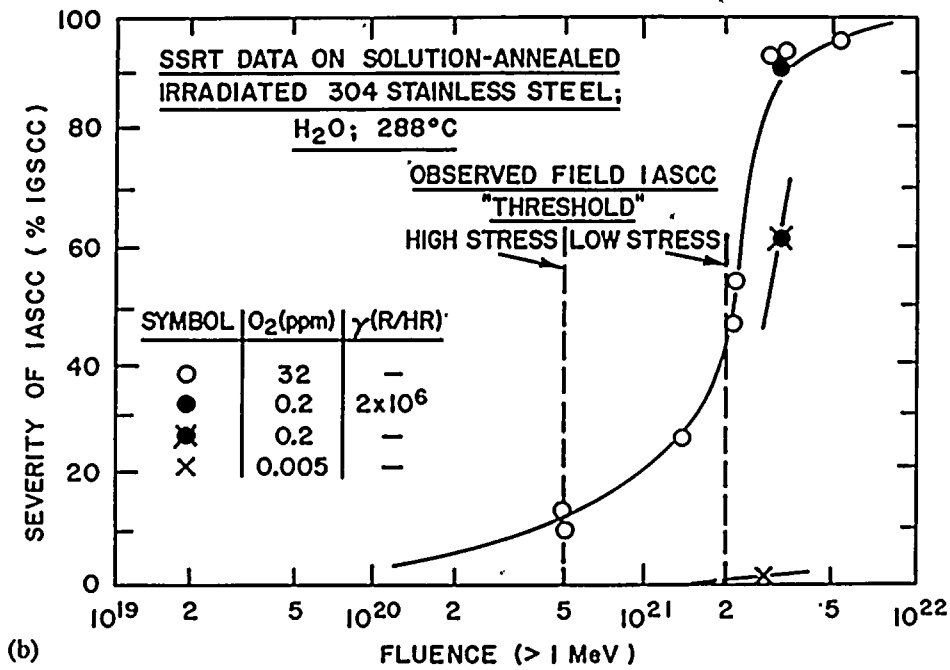
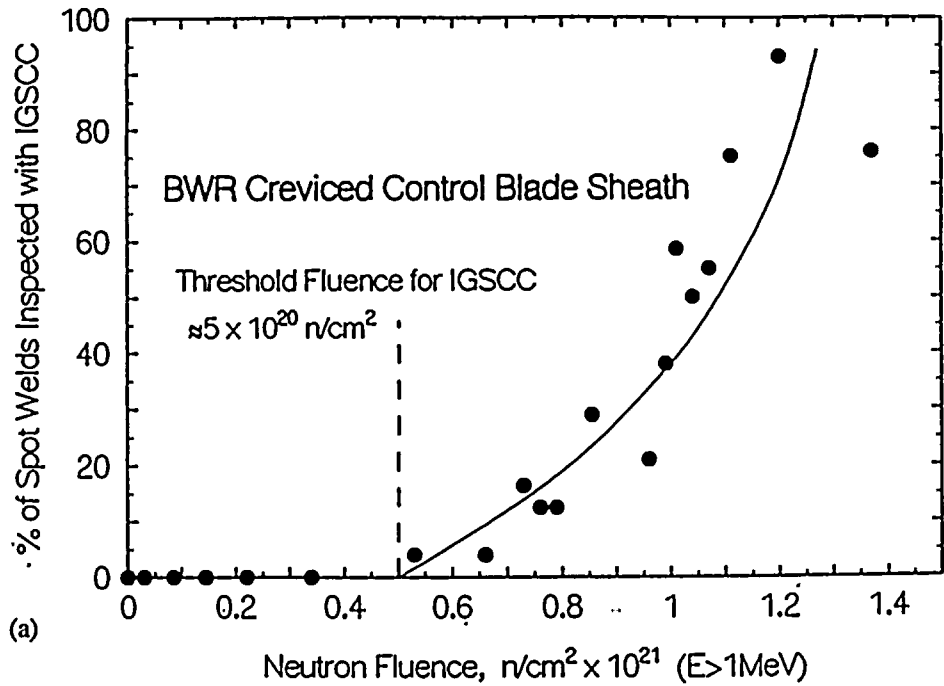


Figure 4-6 Dependence of IGSCC on Fast Neutron Fluence for (a) Creviced Control-Blade Sheath in High Conductivity BWRs [Go90] and (b) as Measured in Slow-Strain-Rate Tests at  $3.7 \times 10^{-7}/\text{s}$  on Pre-Irradiated Type 304 SS in  $288^\circ\text{C}$  ( $550^\circ\text{F}$ ) Water [Ja86]. The Effect of Corrosion Potential via Changes in Dissolved Oxygen is Shown at a Fluence of Approximately  $2 \times 10^{21} \text{ n/cm}^2$



## 5.0 Crack Growth Calculations

As discussed in Section 3, there is a reasonable probability that cracking would initiate on the ID surface of the shroud in the HAZ of weld H4. Although OD crack initiation is unlikely for the fabrication and operating stresses considered, it is possible that initiation could occur if very high, very localized stresses were induced, for example by a weld repair, or if a deeper flaw than has been postulated was not detected during construction. Accordingly, crack growth calculations for OD initiated cracks were also performed. A plant-specific crack growth rate model has been developed for use in the NMP-1 crack growth simulation. Finally, the results obtained using the NMP-1 model developed during this study have been qualitatively compared with the cracking observations from Oyster Creek and Brunswick Unit 2. On a qualitative basis, the model can be used to explain the cracking seen in these plants. Plant-specific analyses using the actual welding details, dimensions, and loads would be needed to provide quantitative results for these plants.

### 5.1 Plant-Specific Crack Growth Rate Model

The NRC crack growth rate model for sensitized 304 SS in low radiation BWR water chemistry environments (described in Reference [NUREG0313]) is written as a power law expression:

$$\frac{da}{dt} = 3.59 \times 10^{-8} K_I^{2.161} \text{ (in./hr.)}$$

where,

$$\frac{da}{dt} = \text{crack growth rate (in./hr.)}$$

$$K_I = \text{applied stress intensity (ksi } \sqrt{\text{in}})$$

A plot of the NRC model is compared with 304 SS crack growth data in Figure 5-1. The NRC model bounds most of the data shown in the figure. The NMPC water chemistry (Table 5-1) is representative of the data given in Figure 5-1 and is common to operating BWRs. Also, crack growth rates were measured in the recirculation line of NMP-1 using statically loaded double-cantilever beam (DCB) specimens. These data are given in Figure 5-2. The measured crack growth is ~3 times lower than that calculated using the NRC model. Therefore, the NRC crack growth rate model is believed to be a conservative representation of crack growth in NMP-1 sensitized 304 SS material which is located in low radiation regions of the primary system.

In order to account for radiation effects on crack initiation and growth, consideration must be given to neutron damage in the steel and to gamma induced radiolytic decomposition of the water. As discussed earlier, IASCC is not an important concern in the H4 non-sensitized 304 SS because the fluences through the end of cycle 11 are not expected to reach threshold levels over significant azimuthal regions in the beltline. However, GE has suggested [Ca94] that there may be an effect on the sensitized material (such as the HAZ of H4) at fast neutron fluences above  $\sim 1 \times 10^{19}$  n/cm<sup>2</sup>. Through the end of cycle 11, the GE data imply a neutron induced increase in the EPR level of about 20%. This possible effect on grain boundary sensitization,



in addition to the acceleration of crack growth due to radiolytic decomposition of water (higher levels of  $O_2$  and  $H_2O_2$ ), are accounted for through the development of a plant-specific crack growth rate model.

As shown in Figures 5-3 and 5-4, plant-specific crack growth rate data for NMP-1 have been measured in the core and in the recirculation line. The location for the in-core measurement is shown in Figure 5-5. As summarized in Table 5-2, the in-core crack growth rate is ~10 times higher than the recirculation line crack growth rate. The fast neutron flux (assumed to attenuate in a qualitatively similar fashion as for gamma radiation) attenuation (Table 5-2) of two orders of magnitude from the core to the shroud indicates that the crack growth rate at the H4 weld is lower than that in the core since there is less radiolysis at the H4 location. Therefore, the plant-specific crack growth rates were interpolated using electrochemical corrosion potential (ECP) data. The use of ECP as an interpolation parameter is reasonable since water radiolysis creates non-equilibrium concentrations of electroactive species ( $O_2$ ,  $H_2$ ,  $H_2O_2$ ,  $O_2^-$ ,  $OH$ , etc.). These species result in a potential drop across the metal-solution interface (referred to as a mixed potential). Thus, the ECP is a useful measure of the corrosion potential and can be used to interpolate crack growth data in cases where the water chemistry is equivalent but the gamma field is different.

Reference [Be93] made use of available thermohydraulic data and radiolysis data reported in Reference [EPRI89] to calculate corrosion potential maps for 8 BWRs. The results for NMP-1 are summarized in Table 5-2 and are plotted in Figure 5-6. These data were used to interpolate the NMP-1 plant-specific ECP measurements to obtain ECP data at the ID and OD surfaces of the H4 weld. The interpolated crack growth data were then obtained using the measured ECP data as the interpolation parameter. The results are summarized in Table 5-2. The crack growth rate model was obtained using the functional form of the NRC crack growth rate formula with the pre-multiplier constant adjusted so that the curve passes through the interpolated crack growth rates. The resulting models are as follows:

Crack Growth From the ID Surface at H4

$$\frac{da}{dt} = 7.690 \times 10^{-8} K_I^{2.161} \quad (\text{in./hr.})$$

Crack Growth From the OD Surface at H4

$$\frac{da}{dt} = 6.489 \times 10^{-8} K_I^{2.161} \quad (\text{in./hr.})$$

The data and models are plotted in Figure 5-7.



## 5.2 Crack Growth Simulation at ID Surface of H4

As described in Section 2, finite element calculations were performed to determine  $K_I$  vs. crack length ( $a$ ) for the loading case of welding residual stresses and operating loads. These results are shown in Table 5-3 as "Load Case 1". The LEM module of pc-CRACK [PCCRACK] was used for the crack growth simulation. The conservatively estimated peak stresses due to circumferential variation in weld shrinkage were also included. This stress distribution is a linearly varying stress field with 8.4 ksi tension on the ID surface and 5.4 ksi tension on the OD surface. Also, the maximum stresses due to ovality (largest diameter of top cylinder welded to smallest diameter of bottom cylinder with jacking) were superimposed on top of the peak weld shrinkage variation stresses. The ovality stresses were +11.4 ksi at the ID varying to -11.4 ksi at OD. These stress fields are shown schematically in Figure 5-8. The  $K_I$  vs. crack length data for the axial shrinkage and ovality stress fields were calculated using a pc-CRACK model for a circumferentially cracked cylinder. The results of these calculations are shown in Table 5-3 as Load Cases 2 and 3.

The crack growth simulation results are shown in Figure 5-9. The initial crack growth is very rapid due to the high stresses at small crack lengths. However, at a flaw length of ~0.4 in., the crack is shown to arrest in the large compressive stress field. Crack arrest in this context is defined as a decrease in the crack growth to a very low rate. As shown in Figure 5-9, there may be a small amount of crack extension after the end of cycle 11, but this small amount of crack growth is negligible. Therefore, we conclude that initiation of an ID surface crack at the weld H4 HAZ will not result in throughwall cracking. The depth of circumferential cracking is expected to be ~0.4 in. when crack arrest occurs.

## 5.3 Comparison With Observation at Other BWRs

It is reasonable to ask whether the model reported here is capable of predicting the cracking observed in the shrouds of other BWRs (such as Oyster Creek and Brunswick Unit 2). Crack initiation and propagation depend strongly on three key variables: stress state, water chemistry, and component material. Even in cases where the water chemistry and materials are similar, the cracking response can be quite different due to differences in stress state which result from geometric, loading, and/or fabrication practice differences. Therefore, each of the shroud girth welds (H1 through H8) must be considered on an individual basis. Further, each weld should be analyzed on a plant-specific basis, particularly when there are detailed fabrication and operating history data available. The more detailed the available data, more quantitative crack growth predictions can be made. In cases where detailed information is not available, bounding analyses must be performed and only qualitative interpretations are possible. This latter approach has been employed in the interpretation of the Oyster Creek and Brunswick Unit 2 cracking data at weld H4.

### 5.3.1 Characterization of the Oyster Creek and Brunswick Unit 2 ID Cracking

The data from the June, 1994, Brunswick Unit 2 weld H4 inspection and similar data from the October, 1994, Oyster Creek inspection are summarized as polar crack maps in Figures 5-10 and 5-11. These maps depict the deepest top or bottom weld crack detected over a given



1. The first part of the document discusses the importance of maintaining accurate records of all transactions. This is essential for ensuring the integrity of the financial data and for providing a clear audit trail.

2. The second part of the document outlines the various methods used to collect and analyze data. These methods include direct observation, interviews, and the use of specialized software tools.

3. The third part of the document describes the results of the data collection and analysis. It shows that there are significant differences in the way that different groups of people interact with the system.

4. The fourth part of the document discusses the implications of these findings for the design and implementation of the system. It suggests that the system should be designed to accommodate the needs of all users.

5. The fifth part of the document concludes the study and provides a summary of the key findings. It also offers some suggestions for further research in this area.

azimuthal range. These maps are schematic representations of cracking location and maximum depth, and are not intended to represent the actual crack morphology. An important obvious difference between the two plants is the fact that the Brunswick Unit 2 cracking was predominantly along the ID, whereas the Oyster Creek cracks were located both at the ID and at the OD. Further, the OD cracks found at Oyster Creek were exclusively along the bottom side of the weld. This is qualitatively explained by the model and further discussion follows. The Brunswick Unit 2 crack depths along the ID surface ranged from 0.10 in. to 0.85 in. deep, with an average depth per indication of 0.53 in.. These data are in qualitative agreement with the calculations for NMP-1 given in Section 5.2. There is documentation of surface grinding at Brunswick Unit 2 which introduced high surface stresses in localized areas. This would explain regions of relatively long shallow cracks. With regard to the Oyster Creek ID cracking, the ID crack lengths ranged from 0.15 in. to 0.9 in., with an average depth per indication of 0.363 in.. This is also in agreement with the NMP-1 plant-specific crack growth calculations. In Reference [GE94], GE attributed the H4 cracking at the ID surface of the Brunswick Unit 2 shroud to IGSCC possibly assisted by an IASCC mechanism. GE stated that crack initiation was accelerated due to localized high weld residual stresses and grinding which resulted from a weld repair.

### 5.3.2 Fabrication History

A comparison of the shroud fabrication details for NMP-1, Oyster Creek, and Brunswick Unit 2 are given in Table 5-4. Although NMP-1 and Oyster Creek are of similar design and were fabricated in the same time period, there are some significant differences between these plants in terms of shroud fabrication. The Oyster Creek shroud fabrication was completed by P. F. Avery several months prior to completion of the NMP-1 shroud. Examination of the fabrication records indicates several significant deviations from specification which would contribute to shroud ovality and misalignment of the Oyster Creek shroud. It is likely that lessons learned during the Oyster Creek shroud fabrication were incorporated into the NMP-1 shroud fabrication. Two significant deviations of the Oyster Creek shroud which may have directly affected SCC at weld H4 are: a variation of the shroud diameter between the central ring and the lower ring from a minimum diameter of 176 1/4 in. to a maximum diameter of 176 23/32 in., and the evidence of contaminant related SCC attack of sensitized materials inside the vessel (safe ends, stub tubes, and lower ring). It is possible that SCC initiated cracks existed (in the HAZ) at the ID and OD surfaces of weld H4 prior to initial startup.

### 5.3.3 Qualitative Interpretation of Oyster Creek OD Cracking

As described in Section 2.0, out-of-round mismatch prior to welding at H4 can produce large bending stresses on the OD surface of weld H4 for NMP-1 and Oyster Creek. The proximity of the central ring causes an upward axial shift in the bending stress inflection point at weld H4. The net effect of this upward shift is to add more stress at the bottom of the weld than at the top. Since the OD cracking at the Oyster Creek weld H4 occurred only at the bottom of the weld, it appears that ovality (or a more general out-of-round condition) induced stresses were involved in the OD crack initiation and propagation. This type of stress peaking on the underside of weld H4 would not be expected to occur at Brunswick Unit 2 because the H4 weld at that plant is 36 in. below the central ring, and the out-of-round stresses would therefore be about the same for both HAZs. It is also likely that ovality related stresses would be less at



NMP-1 since most of the shroud rings and cylinders were within specified tolerances. There is no evidence that an OD surface flaw in excess of 0.010 in. (dye penetrant inspection) deep was present at NMP-1. Also, there was no evidence at NMP-1 of contaminant intrusion (no stub tube leakage during initial startup). Since NMP-1 is not located near the ocean, the possibility of introduction of ocean water salts is much lower than that for Oyster Creek and Brunswick Unit 2.

Examination of the Oyster Creek OD cracking data given in Figure 5-11 suggests an eight cycle stress peak periodicity. Since the Oyster Creek cylinder was out-of-round below the H5 weld (see Table 5-4), we postulate that the top and bottom cylinders were fit together as best as possible with the two major diameters coincident. This approach was probably followed since the lower cylinder was out-of-round but within tolerance. It is also assumed that the two generally oval top and bottom cylinders would require special aligning procedures prior to the submerged arc girth welding. For an 8 cycle periodicity with an assumed 0.1 in. misfit, the calculated stress (see Section 2) field at the bottom HAZ is a linearly varying field from 5.5 ksi at the OD to -5.5 ksi at the ID. The best estimate of the effect of variations in weld shrinkage is a linearly varying stress field with 0 ksi on the OD surface and 4.8 ksi on the ID surface (see Section 2). These assumed stress distributions are shown in Figure 5-12. Since the effect due to the weld shrinkage variation is small at the OD surface for small cracks, these stresses were not included in the analysis.

The crack growth simulation for Oyster Creek was performed using the OD surface crack growth model developed for NMP-1 (See Section 5.1). The results of the Oyster Creek crack growth simulation are summarized in Table 5-5. The calculations were performed at various postulated initial flaw depths for the cases where the weld residual stresses (with operating stresses) are applied separately (Case 1) and with the out-of-round induced stresses (Case 2). Since there was evidence of contaminant intrusion at Oyster Creek, it is possible that  $K_{ISCC}$  was reduced below 10 ksi  $\sqrt{\text{in.}}$ . For Case 1, an initial flaw depth in the range of 0.02 in. to 0.025 in. results in calculated crack depths which are consistent with those observed at Oyster Creek. However, throughwall cracking occurs for postulated flaws of slightly larger size. At this level of initial flaw depth,  $K_I$  is well below 10 ksi  $\sqrt{\text{in.}}$ . For Case 2, an initial flaw depth of a few mils would result in throughwall cracking and  $K_I$  is also much less than 10 ksi  $\sqrt{\text{in.}}$  for this case.

It is important to note that the OD initiated cracks do not arrest and will eventually go throughwall. The crack growth predictions depend strongly on whether radiation effects on crack growth are included and whether out-of-round stresses are included. Since the Oyster Creek measured OD crack lengths are less than 0.68 in., the results in Table 5-5 show that  $K_{ISCC}$  would have to be  $\sim 3$  ksi  $\sqrt{\text{in.}}$  for the cracks to have initiated in the first cycle of operation and not gone throughwall. Even if the crack growth rate were reduced to a rate which is consistent with the NMP-1 recirculation line measurements (i.e., no radiation enhancement) the  $K_{ISCC}$  would still need to be below 10 ksi  $\sqrt{\text{in.}}$ . Therefore, in lieu of sufficient data to perform a plant-specific analysis of the Oyster Creek OD cracking, we conclude that either contaminant related crack initiation occurred, or high localized stresses caused initiation, or crack growth initiation was delayed.

The cases analyzed (Table 5-5) demonstrate that the model is capable of bounding the actual cracking behavior observed at Oyster Creek. If more information on the fabrication and initial flaw sizes were available, a more accurate quantitative assessment could be performed.



1. The first part of the document discusses the importance of maintaining accurate records of all transactions. It emphasizes that this is crucial for ensuring the integrity of the financial statements and for providing a clear audit trail.

2. The second part of the document outlines the various methods used to collect and analyze data. It describes how different types of information are gathered and how they are processed to identify trends and anomalies.

3. The third part of the document focuses on the results of the analysis. It provides a detailed breakdown of the findings, highlighting key areas of concern and suggesting potential solutions to address these issues.

4. The final part of the document concludes with a summary of the overall findings and a recommendation for further action. It stresses the need for ongoing monitoring and reporting to ensure that the system remains effective and secure.



The actual crack depths observed were most likely driven by stresses which are between those postulated. Given the sensitivity to stress state and initial flaw size, it is concluded that the model should only be used for bounding calculations at NMP-1.

#### 5.4 NMP-1 OD Crack Growth Calculations

As discussed earlier, accurate initiation and crack growth prediction over 15 years of operation is difficult because the predicted crack growth depends very sensitively on the stresses, initial flaw depth, crack growth rate, and crack morphology during growth. Therefore, given the uncertainty concerning initial flaw size and peak fabrication stresses, it is only meaningful to perform bounding calculations for NMP-1. Of course, after the weld H4 inspection (scheduled for February, 1995), the model can be used to accurately calculate further crack extension if cracks are detected.

The crack growth calculations were performed using the welding residual, operating, circumferential shrinkage variation, and out-of-round stresses described in Section 5.2. A plot of the stress distributions are given in Figure 5-13. The results of the calculations are summarized in Table 5-6. The calculations show small crack depths (~0.03 in.) at the end of cycle 11 when only the weld residual stresses and operating stresses are applied. Postulated initial flaw lengths of up to 0.01 in. were considered in the calculations.

There is a probability of localized throughwall cracking when the circumferential variation and out-of-round stresses are added to the welding residual and operating stresses. For the case where an elliptical surface crack with small surface length ( $L$ ) to depth ( $a$ ) ratio is used in the crack growth simulation ( $L/a=2$ ), the postulated OD flaw requires a full 11 fuel cycles to grow throughwall (assuming an arrested ID crack of 0.4 in. deep opposite the OD flaw). However, for an  $L/a$  ratio of 5, localized throughwall penetration results after about 35,000 hours of hot operation, thus allowing time for circumferential crack growth to occur. We therefore conclude that the possibility of throughwall cracking must be considered in the structural assessment. These analyses are described below.

#### 5.5 NMP-1 Worst Case Cracking Behavior

The following approach was used to bound the NMP-1 cracking behavior. Even with conservative estimates of axial shrinkage variation induced stresses and radial mismatch induced stresses added to the welding and operating stresses, peak outer surface HAZ axial stresses for realistic initial flaw sizes ( $<0.010$  in.) result in  $K_I$  less than  $K_{ISCC}$ . It was therefore concluded that for a crack to initiate at the outer surface some rather localized anomalous conditions must exist. Two cases for crack initiation and growth at the outer surface are used to explore this possibility. In both cases, non-axisymmetric stresses and non-axisymmetric crack growth behavior are considered.

In the first case, it is assumed that sufficient conditions exist for initiation at sixteen evenly spaced locations around the circumference. Since the anomalous conditions are assumed to be localized, it is further assumed that the crack initiation results in a crack surface length to depth ratio of 2 (i.e., circular crack front shape). This small ratio is considered to be reasonable



based on the assumed localized nature of the anomalous conditions, the fact that the combined stresses initially increase with distance from the outer surface, and the fact that the stresses at the ends of semi-elliptical flaws tend to be smaller than those at the deepest point thus promoting a circular crack shape. Using the computed welding residual and operating stresses, plus worst case estimates for stresses due to circumferential variation in axial shrinkage and radial mismatch, a crack growth analysis was performed and the results are given in Table 5-6. The cracks are predicted to grow to a depth of 1.086 in.. At this depth the cracks were growing very slowly and appeared to be essentially arrested. However, these cracks will essentially be throughwall since an ID crack is assumed to have propagated to a depth of 0.4 inches and arrested.

In the second case, non-axisymmetric stresses and crack growth behavior are again considered. It is again assumed that sufficient conditions exist for initiation at sixteen evenly spaced locations around the circumference. The difference from the first case is that the cracks are assumed to have a surface length to depth ratio of 5. Using the computed welding residual and operating stresses, plus worst case estimates for stresses due to circumferential variation in axial shrinkage and radial mismatch, the crack growth model predicts these semi-elliptical flaws will grow throughwall in 35,740 hours. At this point, it is further assumed that ID cracks have already grown to a depth of 0.4 in. and arrested at all points on the circumference. The circumferential length of the throughwall OD cracks is therefore 5.5 in. at the time they meet the arrested ID cracks.

It is then assumed that these throughwall cracks propagate circumferentially for the remaining time of 98,113 hours to the end of cycle 11. Since the stresses driving these cracks vary through the thickness thus making a rigorous calculation tedious, an upper bound crack growth rate of  $5.0 \times 10^{-5}$  in/hr is assumed based on the work of GE [GE94]. In the remaining time, the 5.5 in. cracks grow to a final length of 15.3 in.. This leaves remaining ligaments between the 16 cracks of 19.6 in. each. At the time the OD crack grew throughwall, the total uncracked ligament was 62% of the original cross-section and 70% of the cracked area was due to the ID cracking. After the circumferential growth, the uncracked ligament is 41% of the total cross-section and the ID cracking accounts for 45% of the total cracked area. These results are summarized in Table 5-7. Based on the GE calculations reported in [GENE523], the 41% remaining ligament is more than sufficient to ensure structural integrity.

[Faint, illegible text, possibly bleed-through from the reverse side of the page]



Table 5-1 NMP-1 Recirculation Line Water Chemistry and Fluence

Operating Cycle	Mean Value Conductivity ( $\mu\text{S}/\text{cm}$ )	Chloride (ppb)
1	0.432	30
2	0.525	46
3	0.591	58
4	0.445	44
5	0.291	33
6	0.225	27
7	0.181	26
8	0.133	25
9	0.087	18
10	0.082	1
11	0.084	1

ECP                       $\sim 70 \text{ mV}_{\text{SHE}}$

pH                         $\sim 6.6$

O<sub>2</sub>                         $\sim 250 \text{ ppb}$



Table 5-2 Crack Growth Rate as a Function of ECP for Nine Mile Point Unit 1

Plant Location	Fast Neutron Flux (n/cm <sup>2</sup> /sec)	ECP (mV <sub>SHE</sub> )		Crack Growth Rate (in/hr)
		measured	calculated <sup>b</sup>	
In-Core	4.85 x 10 <sup>13</sup> (see e)	250 <sup>a</sup>	247	1.42 x 10 <sup>-4</sup> (see a)
Shroud Weld H4 ID	8.97 x 10 <sup>11</sup>	167 <sup>c</sup>	217	8.07 x 10 <sup>-5</sup> (see d)
Shroud Weld H4 OD	4.82 x 10 <sup>11</sup>	150 <sup>c</sup>	211	6.81 x 10 <sup>-5</sup> (see d)
Recirculation Line	low	75 <sup>a</sup>	184	1.27 x 10 <sup>-5</sup> (see a)

- a) Measured data reported in [ESEERCO88]
- b) Reported in [Be93]
- c) Interpolated using calculated ECP data
- d) Calculated using measured ECP data
- e) The calculated flux is in good agreement with the 3D MONICORE code computations performed using 1993 in-core measurements. These calculations resulted in a flux of 4.77 x 10<sup>13</sup> n/cm<sup>2</sup>/sec at local power range monitor (LPRM) number 19.



1  
 2  
 3  
 4  
 5  
 6  
 7  
 8  
 9  
 10  
 11  
 12  
 13  
 14  
 15  
 16  
 17  
 18  
 19  
 20  
 21  
 22  
 23  
 24  
 25  
 26  
 27  
 28  
 29  
 30  
 31  
 32  
 33  
 34  
 35  
 36  
 37  
 38  
 39  
 40  
 41  
 42  
 43  
 44  
 45  
 46  
 47  
 48  
 49  
 50  
 51  
 52  
 53  
 54  
 55  
 56  
 57  
 58  
 59  
 60  
 61  
 62  
 63  
 64  
 65  
 66  
 67  
 68  
 69  
 70  
 71  
 72  
 73  
 74  
 75  
 76  
 77  
 78  
 79  
 80  
 81  
 82  
 83  
 84  
 85  
 86  
 87  
 88  
 89  
 90  
 91  
 92  
 93  
 94  
 95  
 96  
 97  
 98  
 99  
 100



Table 5-3 Stress Intensity Factors for Crack Growth From the ID Surface of H4

Crack Length (in.)	$K_I$ (ksi $\sqrt{\text{in}}$ )			
	Load Case 1	Load Case 2	Load Case 3	Total
	After Welding and at Operating Temperature	Peak $K_I$ Due to Circumferential Variation in Weld Shrinkage	Peak $K_I$ Due to Ovality During Fabrication	
0	0.0	0.0	0.0	0
0.01	4.8	1.6	2.2	8.6
0.02	6.7	2.3	3.1	12.1
0.031	7.0	2.9	3.9	13.8
0.094	5.6	5.1	6.4	17.1
0.156	3.5	6.6	8.0	18.1
0.219	-2.7	7.9	9.2	14.4
0.281	-11.5	9.2	10.1	7.8
0.344	-18.3	10.4	10.9	3.0
0.406	-23.6	11.7	11.6	-0.3
0.469	-28.5	13.1	12.2	-3.2
0.531	-32.6	14.6	12.9	-5.1
0.594	-36.7	16.2	13.5	-7.0
0.656	-41.4	17.9	14.0	-9.5
0.719	-42.4	19.7	14.3	-8.4



**Table 5-4 Comparison of Shroud Fabrication Details for NMP-1, Oyster Creek, and Brunswick Unit 2**

Item	NMP-1	Oyster Creek	Brunswick
Shroud ID (wall thickness) Specified	176±0.5 (1.5 in.)	176±0.5 (1.5 in.)	174.5 (1.5 in.)
H4 Distance Below Central Ring	18.5 in.	18.5 in.	36 in.
H4 Weld Sequence	-6 root passes ID -followed by Balance ID -followed by 6 root passes OD -followed by Balance OD	-6 root pass ID -followed by Balance ID -followed by 6 root passes OD -followed by Balance OD	-ID welding completed first in 5 passes -OD welding was then completed in 5 additional passes
Shroud Plate Material	304 SS (0.042-0.056 wt%C)	304 SS (0.042-0.056 wt%C)	304 SS (0.049-0.060 wt%C)
H4 Weld	double-J, submerged arc, 308 SS, last weld	double-J, submerged arc, 308 SS, last weld	double-J, 308L SS, one of two last welds
Shroud Fabrication	P.F. Avery	P.F. Avery	Sun Shipbuilding and Dry Dock Fabrication
Date of H4 Weld	2/6/67 - 2/13/67	10/17/66 - 11/3/66	June 1971
Reported Deviations Related to Shroud Ovality	-zone D-9 (180±1/4 in. diameter) varies from 179 27/32 in. to 180 14/32 in.  -zone F-7 (162± 1/16 in. diameter) varies from 161 24/32 in. to 162 4/32 in.  -weld H5 was ≈3/32 in. undersized at 200° azimuth for ≈ three feet. (weld repaired)	-the four notches on the core support ring were significantly out of specification. (Special field alignment practices were followed)  -zone F-11 (174± 1/8 in. diameter) varies from 173 12/16 in. to 173 14/16 in.  -zone F-11 (177± 1/8 in. diameter) varies from 176 25/32 in. to 176 28/32 in.  -zone E-11 (176± 1/2 in. diameter) varies from 176 1/4 in. to 176 23/32 in.  -contaminant caused safe ends, stub tubes, and shroud lower ring cracking	-adjustable spiders were used for fit-up  -repair welds were performed  -surface grinding was done  -hydraulic jacking and jacking pads were used during installation  -indentations from jacking heads observed on ID surface



**Table 5-5 Crack Growth Simulation For Oyster Creek Weld H4 OD Cracking**

Postulated Initial Flaw Depth (in.)	Calculated Final Crack Depth at 15 EFPY (in.)			
	Case 1		Case 2	
	Weld Residual and Operating Stresses		Weld Residual, Operating, and Out-of-Round Stresses	
	With Radiation Effects on Crack Growth Rate	Without Radiation Effects on Crack Growth Rate	With Radiation Effects on Crack Growth Rate	Without Radiation Effects on Crack Growth Rate
0.001	0.0011	---	0.0018	---
0.002	0.0028	---	0.0358	---
0.003	0.0055	---	>1.2	---
0.004	0.0114	---		---
0.005	0.0196	---		---
0.006	0.0281	---		---
0.007	0.0366	---		---
0.008	0.0444	---		---
0.009	0.0516	---		---
0.010	0.0583	---		0.0304
0.020	0.1595	---		0.0640
0.025	0.3483	---		0.0820
0.030	>1.2	0.0421		0.1015
0.050		0.0721		0.2170
0.075		0.1167		1.0683
0.10		0.1811		>1.2
0.15		0.7361		
0.20		>1.2		



Table 5-6 NMP-1 Bounding Crack Growth Calculations

Postulated Initial Flaw (in.)	Calculated Final Flaw Depth (in.)				
	Welding Residual/ Operating Stresses <sup>a</sup>	Welding Residual/Operating, Circumferential Variation, and Out-of-Round Stresses <sup>b</sup>			
		Large L/a Model <sup>c</sup>	L/a=2 Model <sup>d</sup>	L/a=5 Model <sup>e</sup>	L/a=10 Model <sup>f</sup>
0.001	0.0023	1.0597	>1.2 (at 59,320 hrs)	>1.2 (at 41,480 hrs)	>1.2 (at 35,490 hrs)
0.002	0.0049	1.0753	---	---	---
0.003	0.0075	1.0795	---	---	---
0.004	0.0102	1.0816	---	---	---
0.005	0.0130	1.0829	---	---	---
0.006	0.0159	1.0838	---	---	---
0.007	0.0188	1.0844	---	---	---
0.008	0.0217	1.0850	---	---	---
0.009	0.0246	1.0854	---	---	---
0.010	0.0277	1.0857	>1.2 (at 35,740 hrs)	>1.2 (at 22,900 hrs)	>1.2 (at 18,990 hrs)

- a These stresses include the welding residual stresses and stresses due to operating loads.
- b These stresses include the welding residual stresses, stresses due to operating loads, peak circumferential welding variation stresses, and stresses due to fit-up to correct for out-of-roundness.
- c Circumferential crack in a cylinder model. The surface length of the flaw is large compared to its depth.
- d Elliptical surface crack in a plate with surface length (L) to crack depth (a) equal to 2. Crack arrest was apparent from the crack depth vs. time plot.
- e Elliptical surface crack in a plate with surface length (L) to crack depth (a) equal to 5. Although the fracture mechanics model limits were exceeded, crack arrest prior to throughwall propagation was apparent from the crack depth vs. time plot.
- f Elliptical surface crack in a plate with surface length (L) to crack depth (a) equal to 10.



Table 5-7 Worst Case Cracking Behavior Summary

ASSUMPTIONS

1. Assume ID flaws propagate to 0.4 in. depth then arrest (full 360 degrees)
2. Assume OD flaws initiate at 16 locations on the circumference and propagate throughwall with aspect ratios of 5 (initial circumferential length =  $(1.5 - 0.4)(5) = 5.5$  in.)
3. Assume 1 and 2 occurs within 35,740 hours from start up (based on crack growth analysis with worst case stresses due to welding, axial shrinkage variations, and radial mismatch)
4. Assume throughwall OD cracks propagate circumferentially according to GE's bounding crack growth rate of  $5.0 \times 10^{-5}$  in/hr.

REMAINING LIGAMENT

Shroud mean circumference: 558 in.

Total shroud load carrying area: 836 in<sup>2</sup>

Cracked area at 35,740 hours:

ID Crack:	$(88.0 + 88.4)\pi(0.4) = 222$ in <sup>2</sup>
OD Cracks:	$(5.5)(1.5 - 0.4)(16) = 97$ in <sup>2</sup>
Total Cracked Area:	319 in <sup>2</sup>
Total Uncracked Area:	517 in <sup>2</sup>
Percent Uncracked Area:	62%

Circumferential growth starting at 35,740 hours and ending at 133,853 hours:

One Crack Tip:	$(5.0 \times 10^{-5})(98,113) = 4.9$ in.
Two Crack Tips:	$(2)(4.9) = 9.8$ in.
Final Crack Length:	$5.5 + 9.8 = 15.3$ in.
Uncracked Circumference:	$558 - (16)(15.3) = 313$ in.
Uncracked Ligament Sizes:	$313/16 = 19.6$ in.

Remaining ligament at 133,853 hours:

ID Crack:	$(88.0 + 88.4)\pi(0.4) = 222$ in <sup>2</sup>
OD Cracks:	$(15.3)(1.5 - 0.4)(16) = 269$ in <sup>2</sup>
Total Cracked Area:	491 in <sup>2</sup>
Total Uncracked Area:	345 in <sup>2</sup>
Percent Uncracked Area:	41%



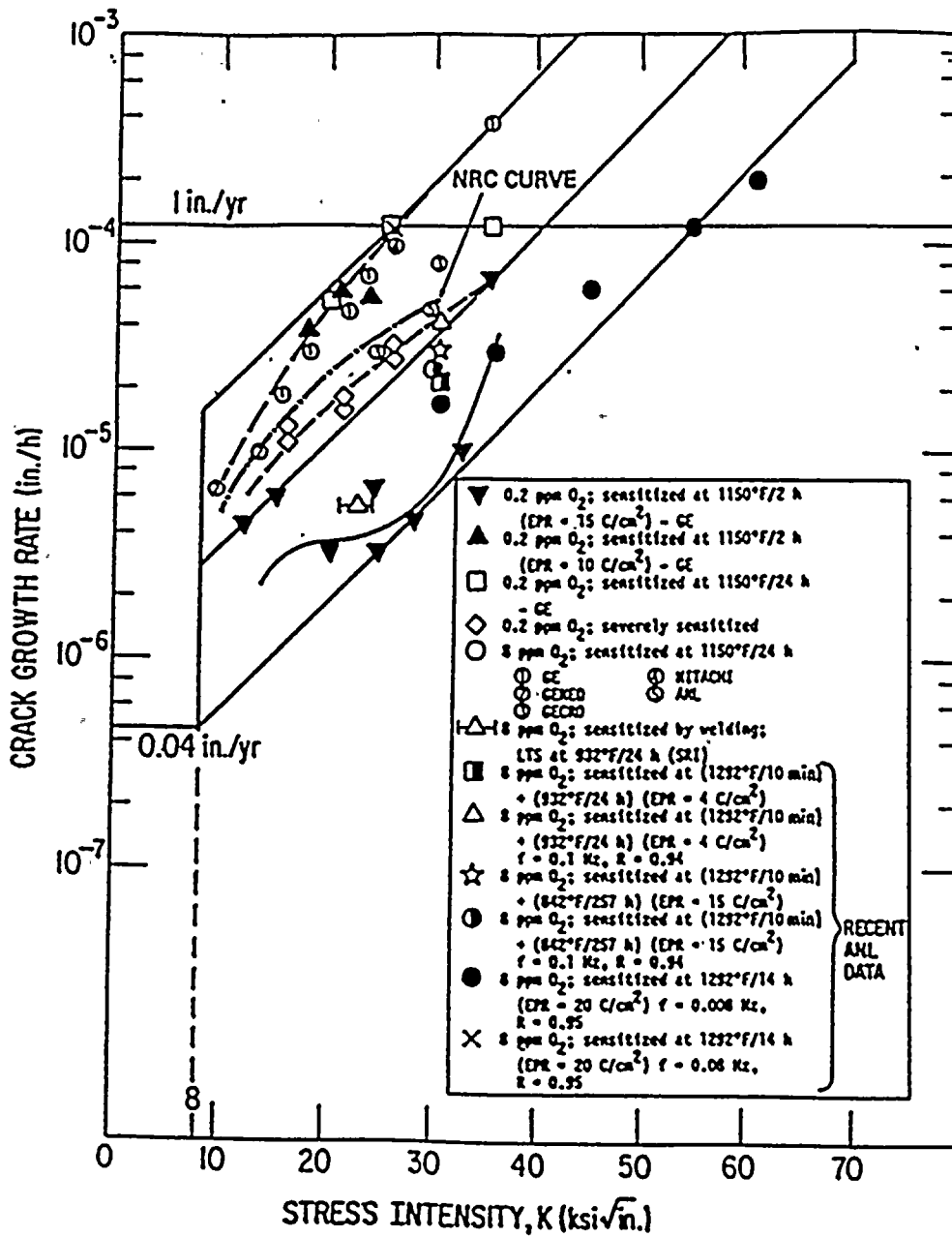


Figure 5-1 Plot of NRC Crack Growth Rate Model and 304 SS Data



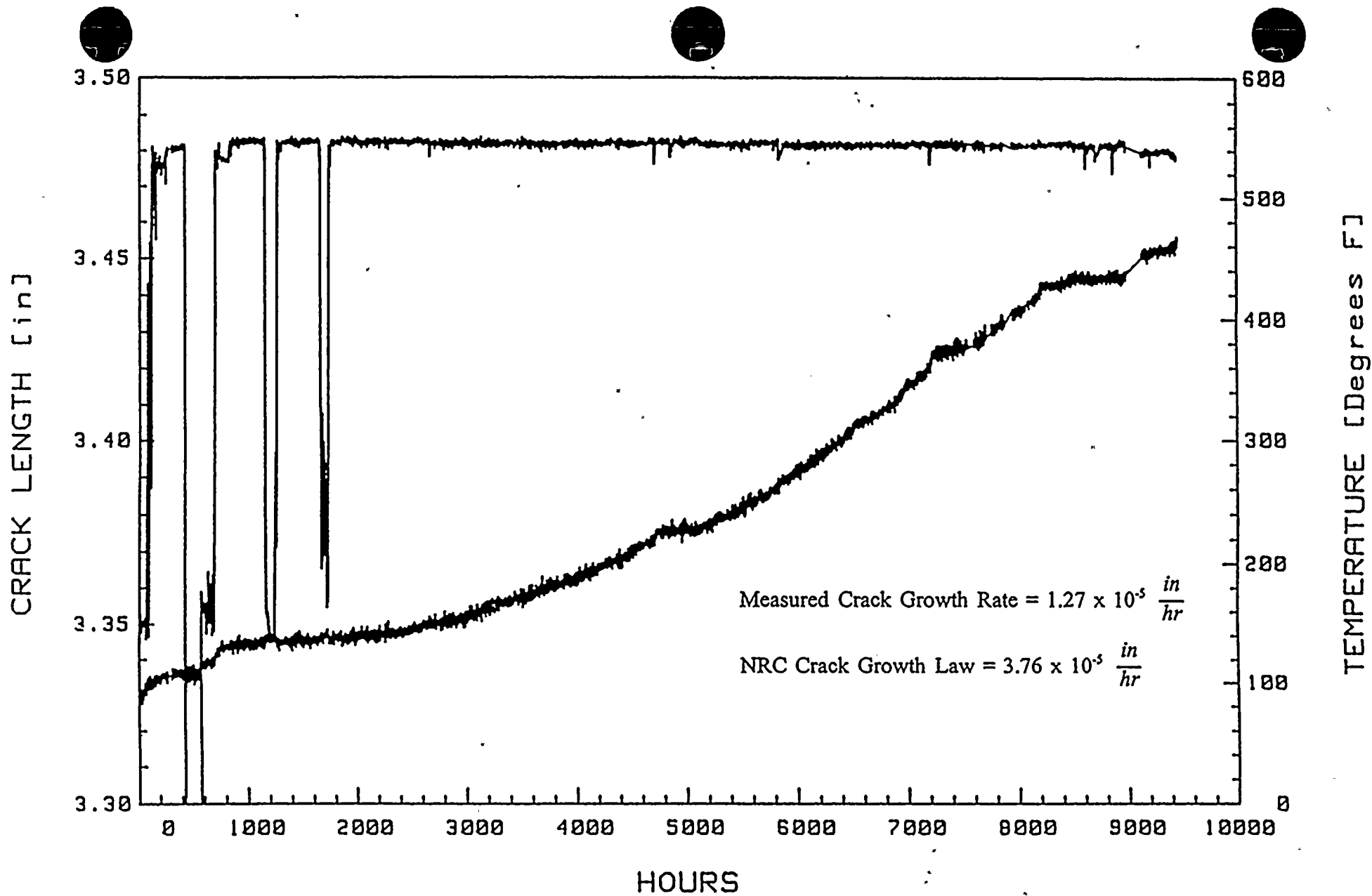


Figure 5-2 Sensitized Type 304 SS in NMP-1 Recirculation Water Piping [ESEERCO88]



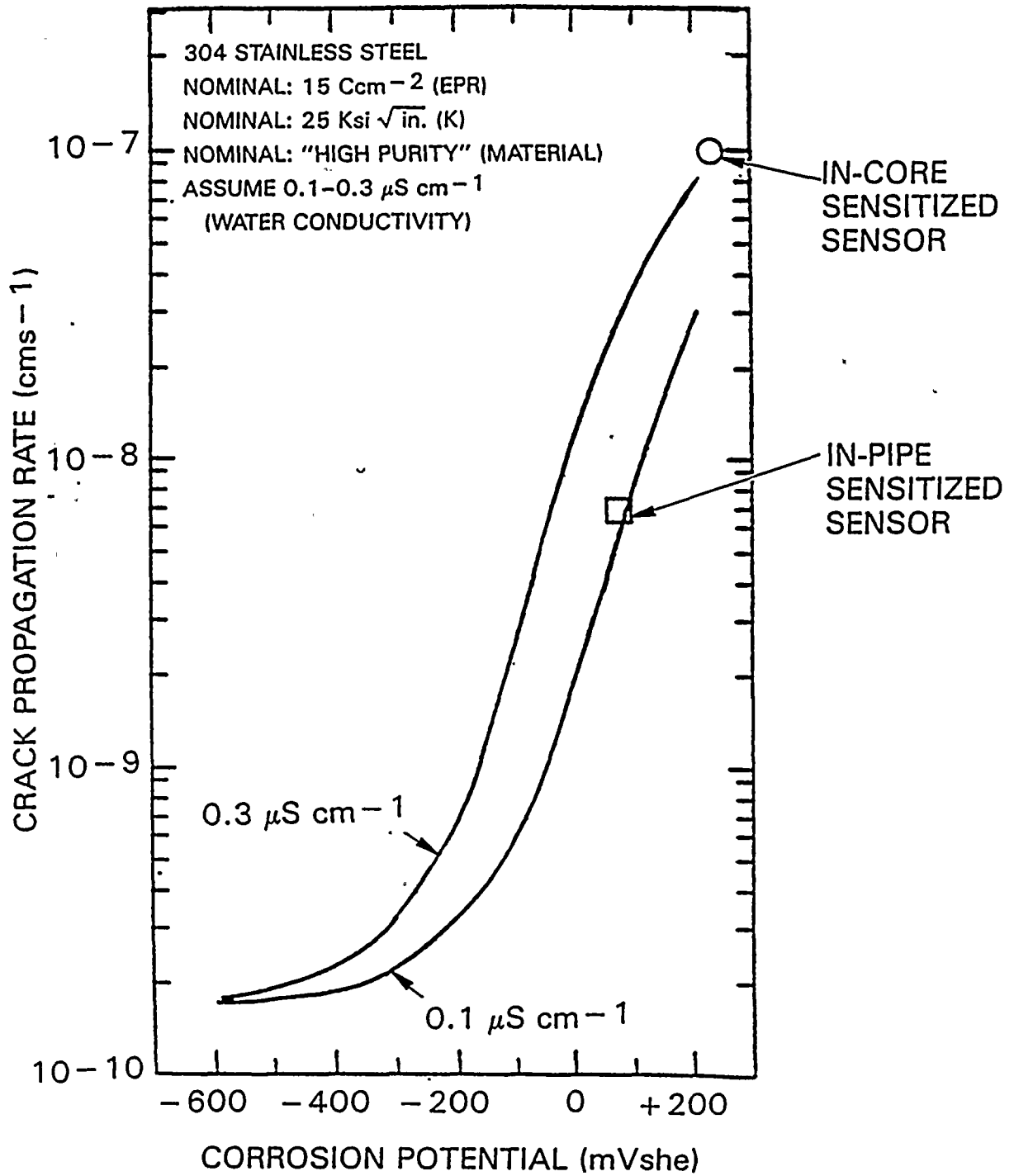


Figure 5-3 Observed vs. Theoretical Predicted Crack Growth Rates for Sensitized Stainless Steel Sensors [ESEERCO88]



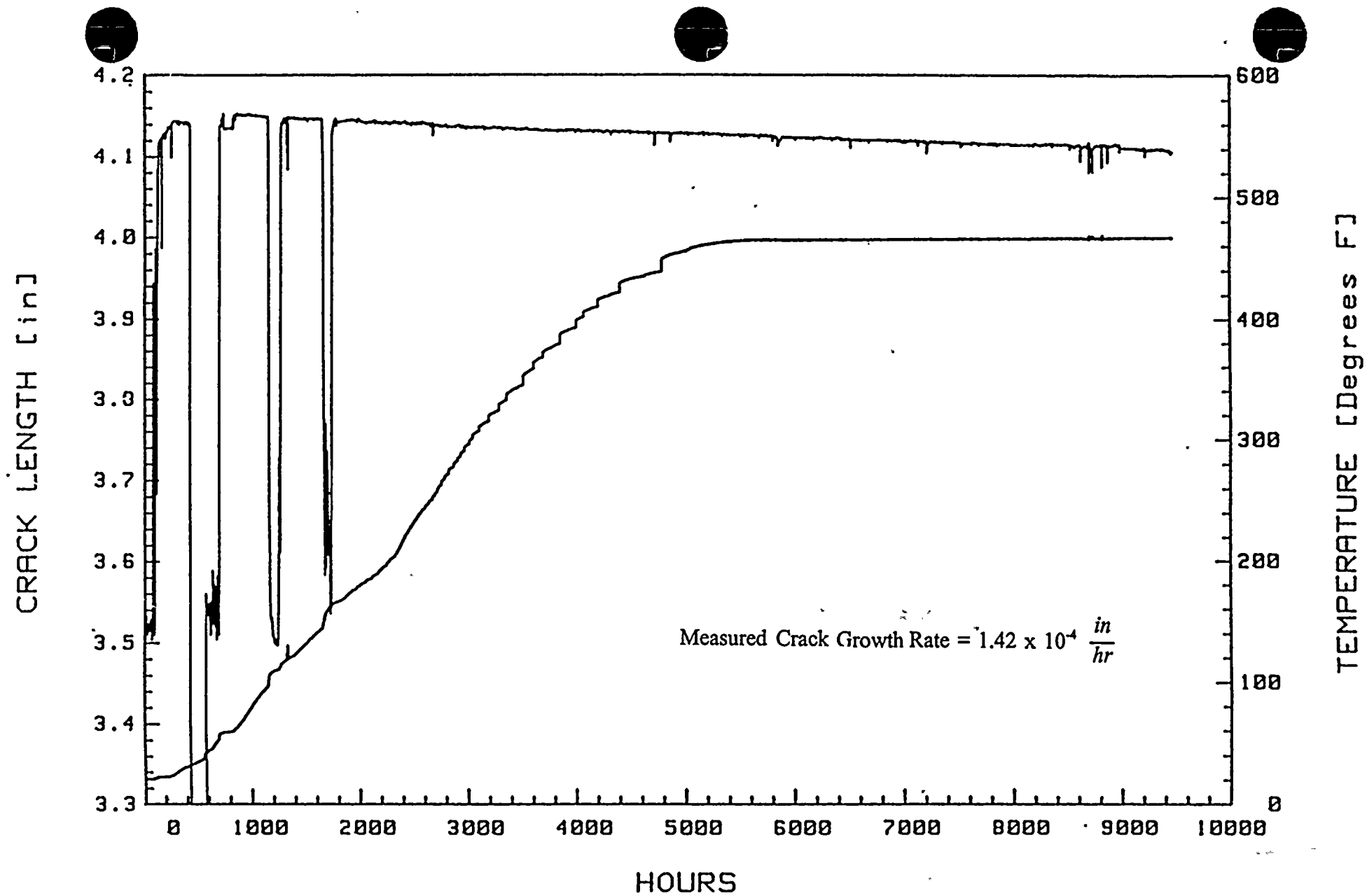


Figure 5-4 Sensitized Type 304 SS in NMP-1 Core [ESEERC088]



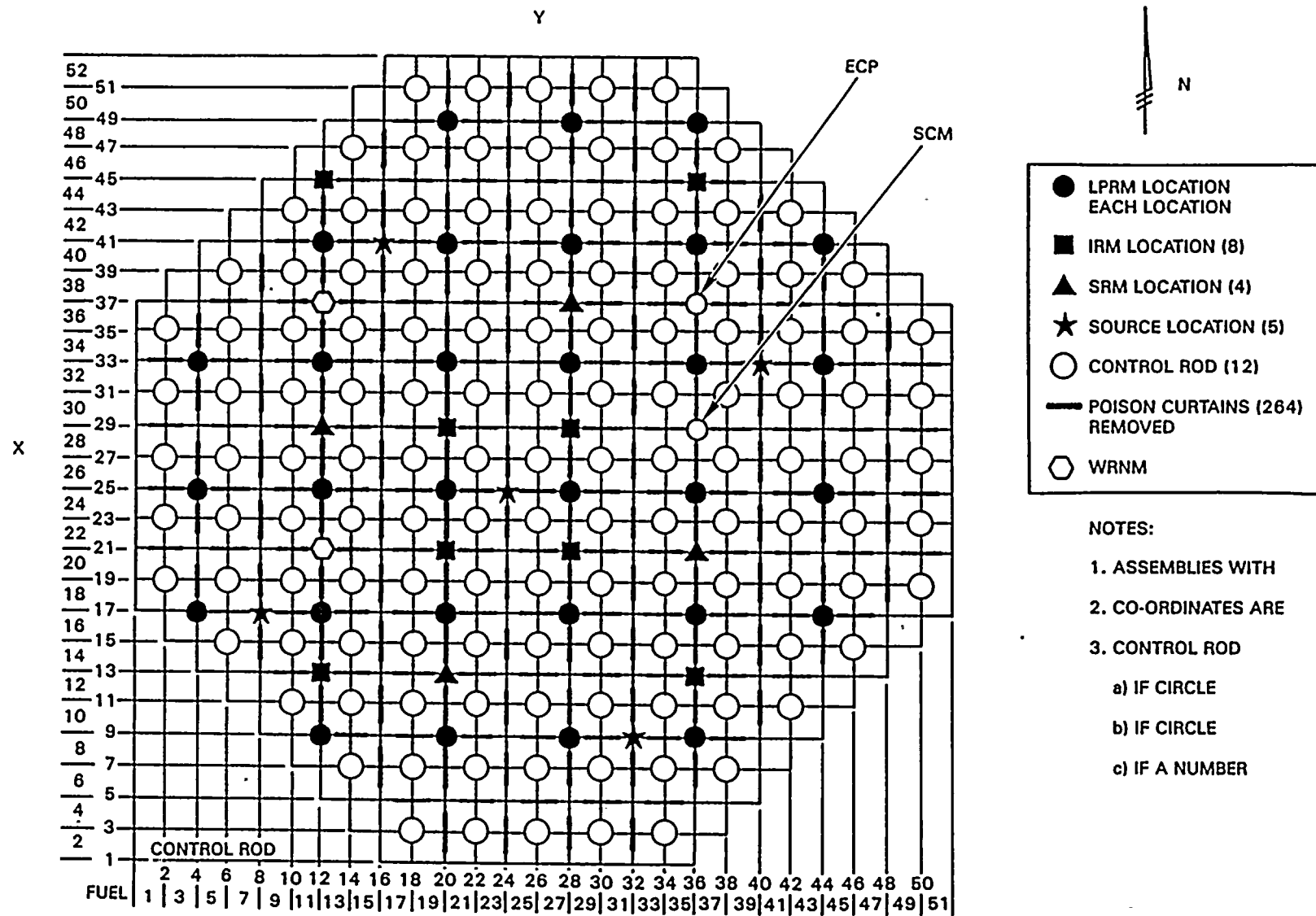


Figure 5-5 Location of the NMP-1 In-Core Stress Corrosion Monitor (Designated SCM) [ESEERCO88]



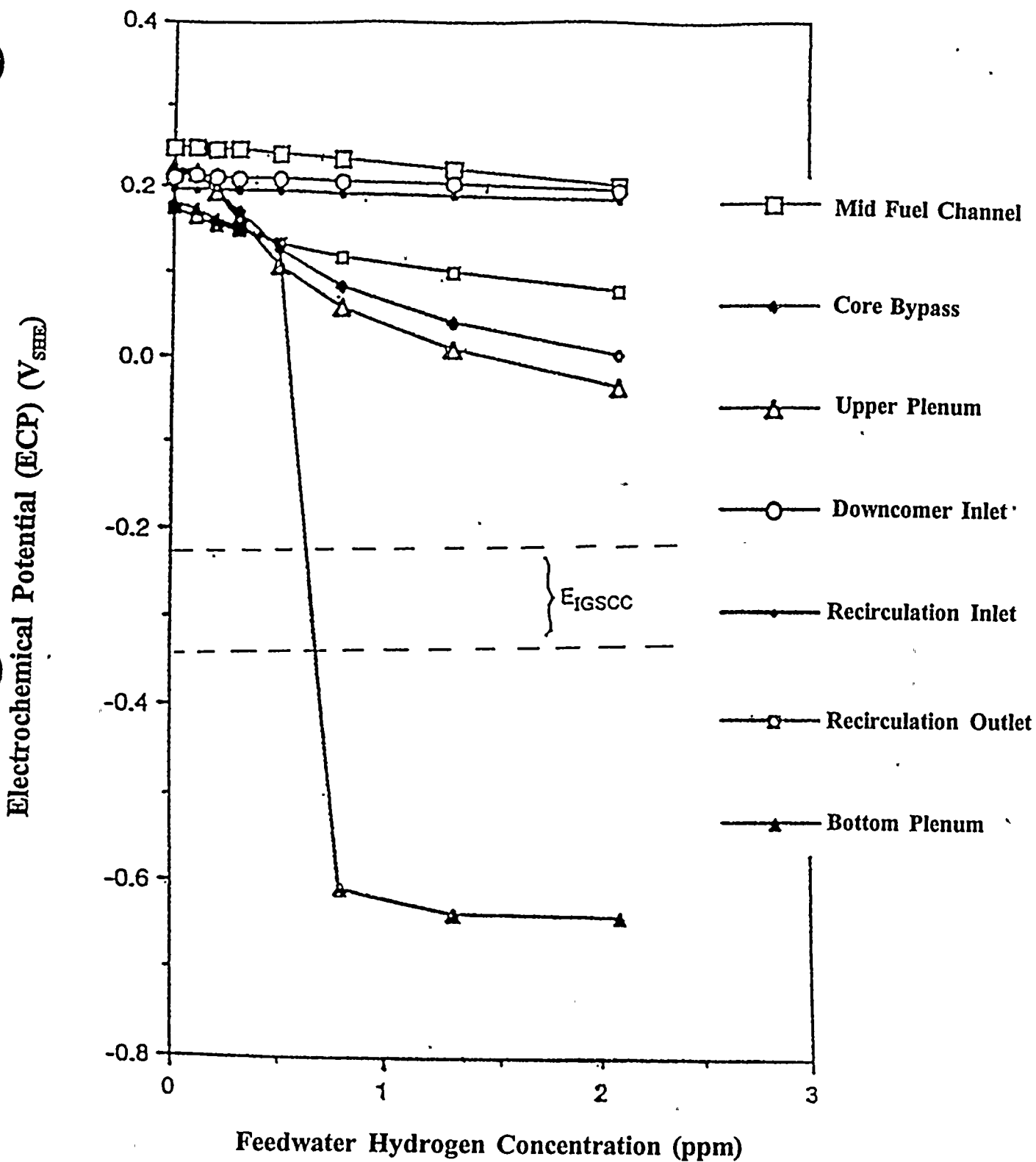


Figure 5-6 Electrochemical Corrosion Potential as a Function of Feedwater Hydrogen Concentration for NMP-1



# NMP-1 Plant-Specific Crack Growth Model

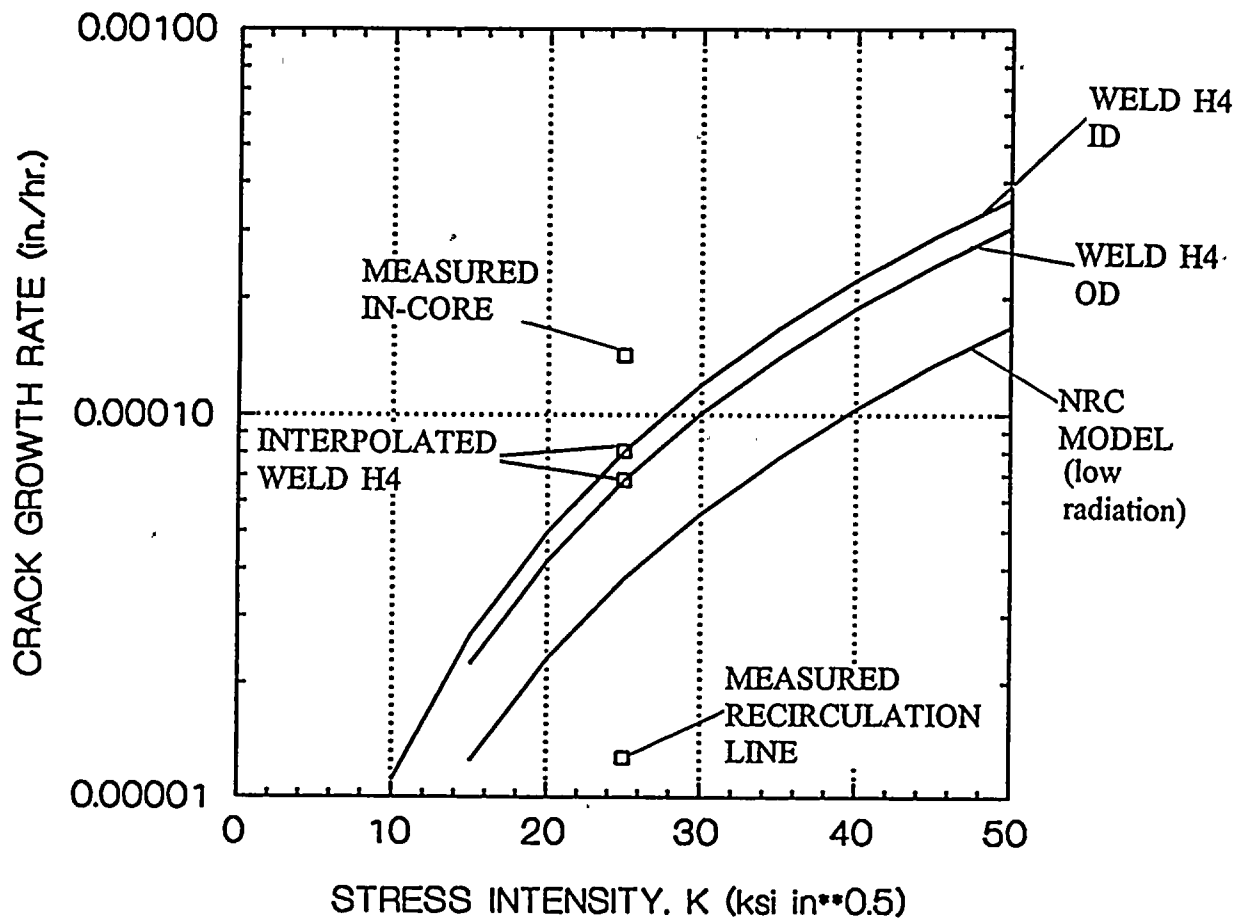


Figure 5-7 Plant-Specific Crack Growth Rate Model for NMP-1 Weld H4



# Axial Stress Distribution for NMP-1 Crack Growth Simulation

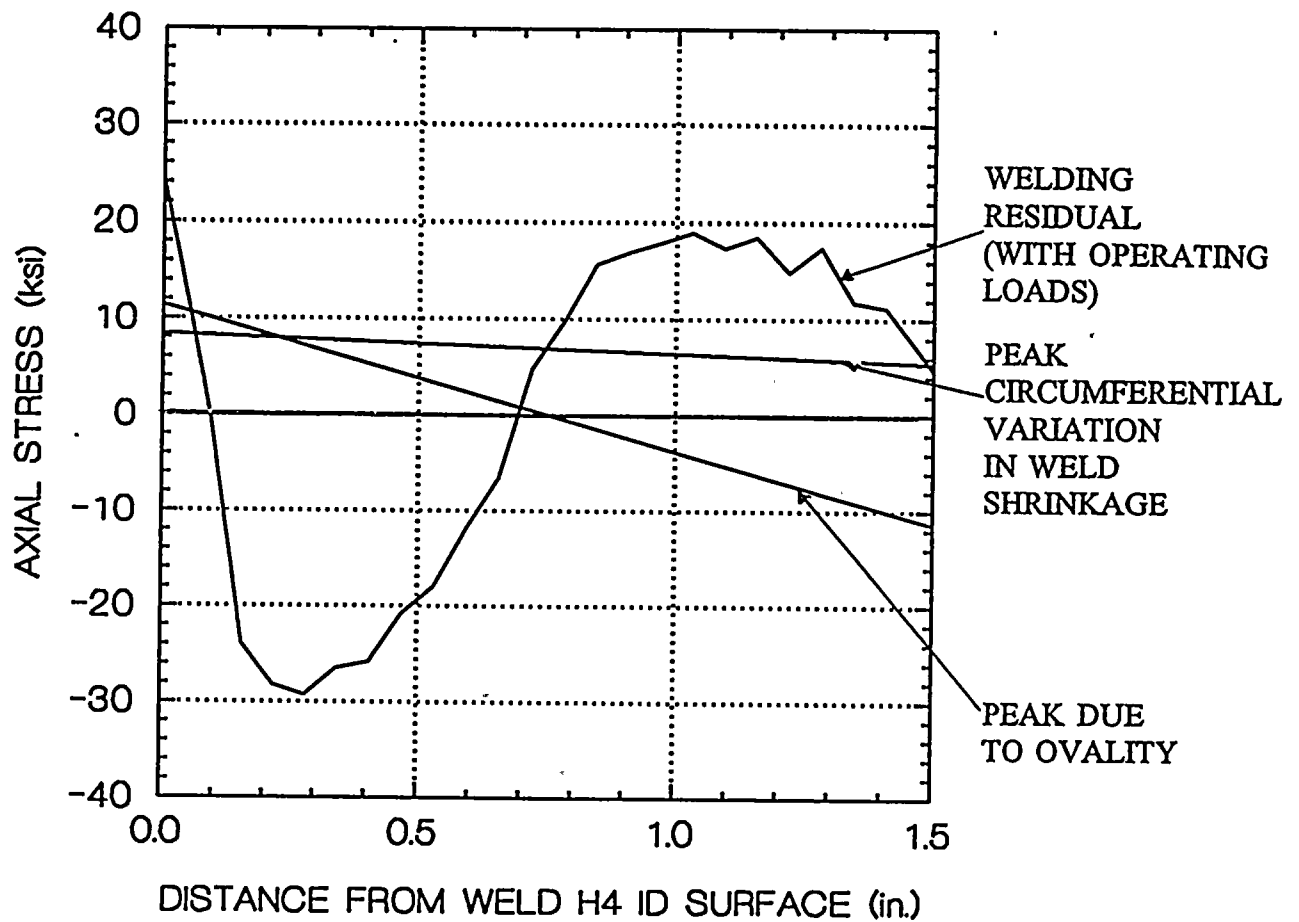
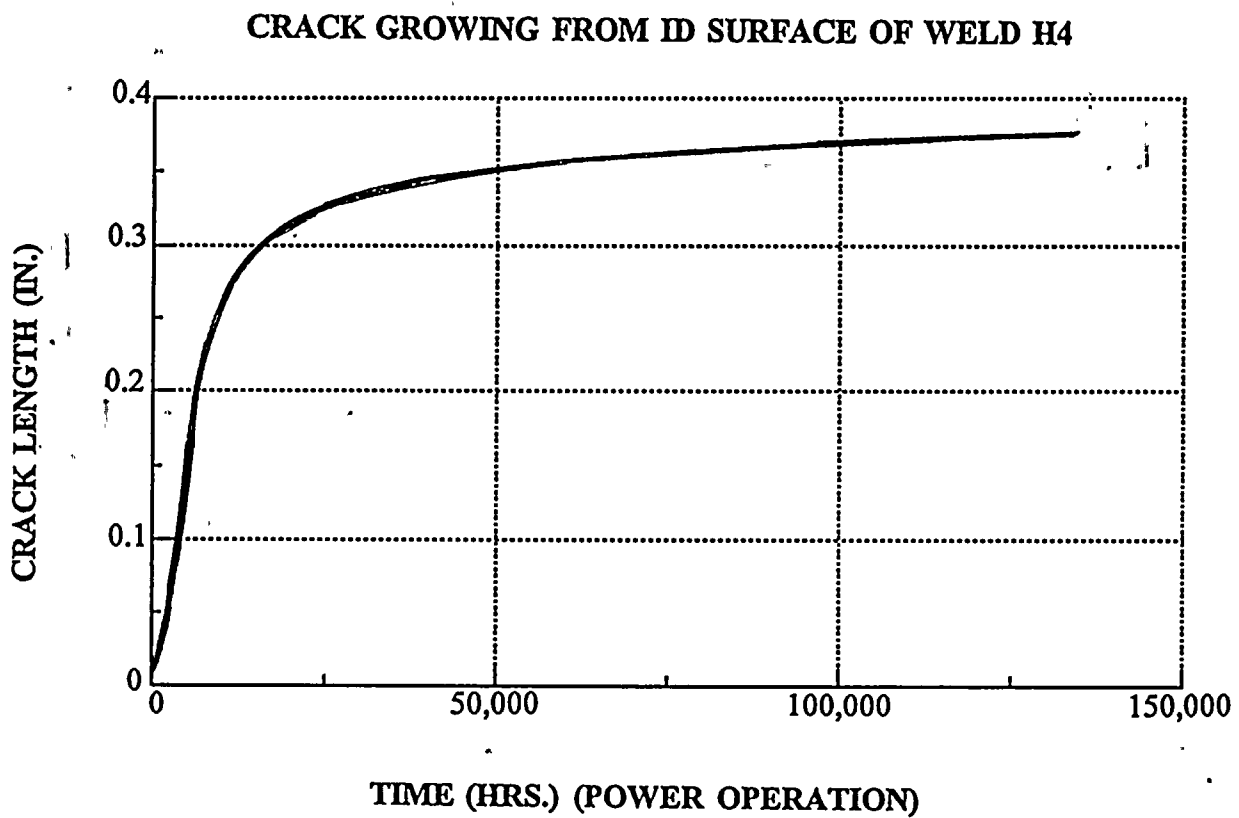


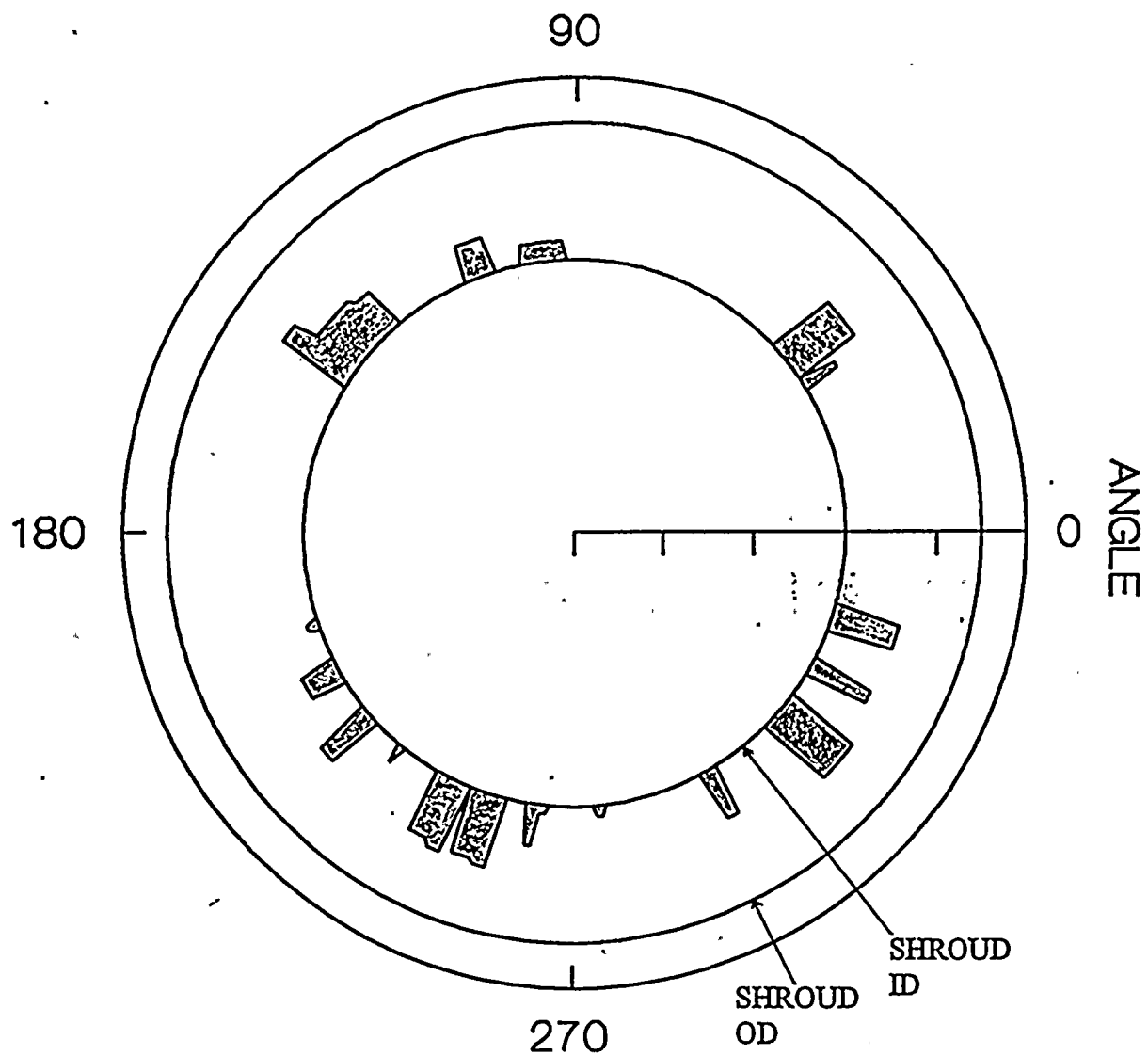
Figure 5-8 Schematic Representation of Peak Stress Field at ID Surface of Weld H4





**Figure 5-9** Calculated Crack Length as a Function of Operating Time to the End of Cycle 11—Crack From ID Surface of Weld H4—Initial Flaw Size of 0.01 in.





OD CRACKING - NO CRACKS OBSERVED

ID CRACKING - BOTH LOWER AND UPPER SIDE OF WELD

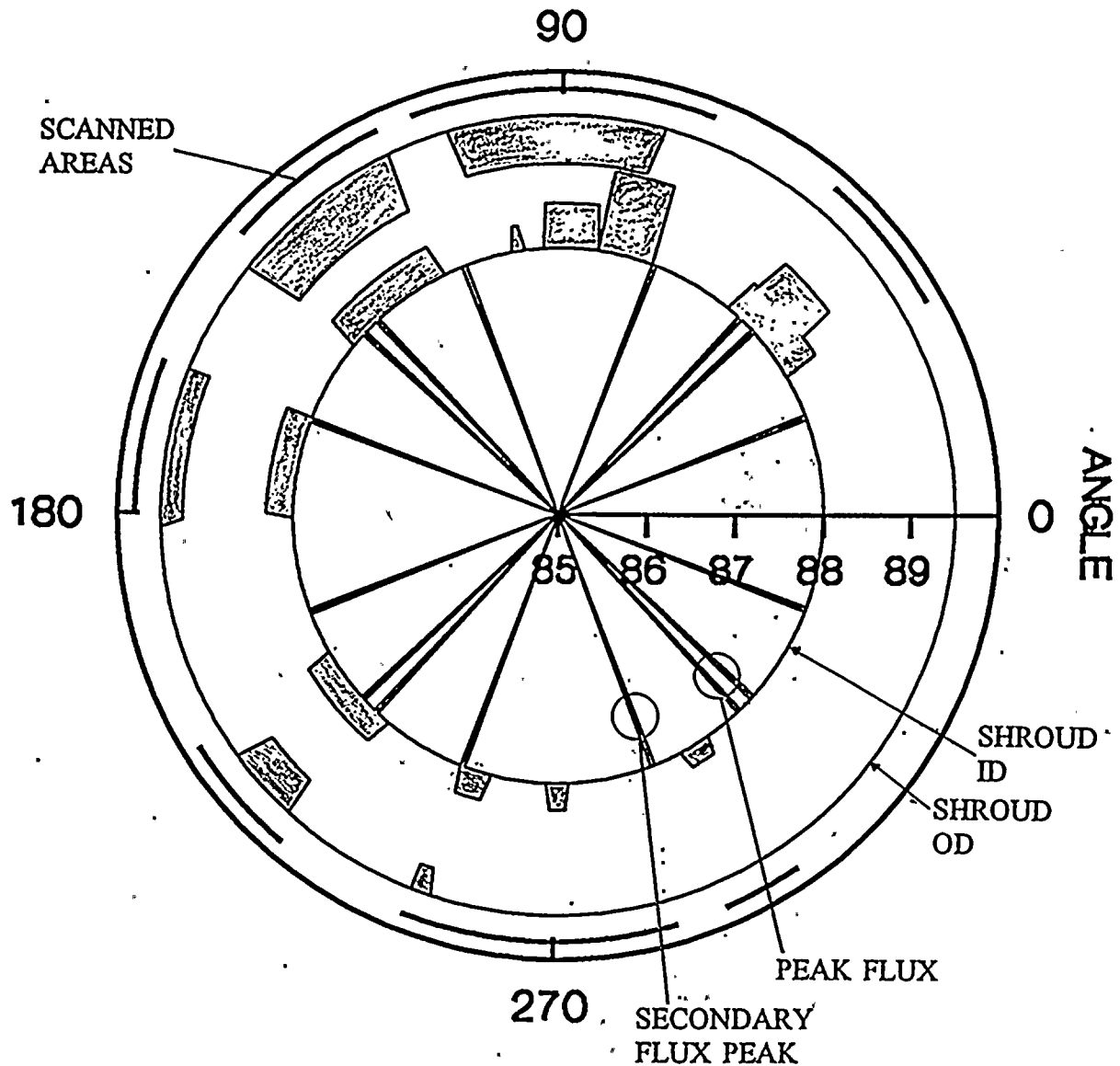
NOTE: The crack depth and circumferential length were measured during UT examination. The crack shapes shown here are schematic and do not represent the actual crack morphology.

Figure 5-10 Brunswick Unit 2 H4 Weld Cracking Map Showing Deepest Detected Flaws as a Function of Azimuthal Angle (UT indications are shown as shaded areas)



441326

1952



- OD CRACKING - ALL ON LOWER SIDE OF WELD
- ID CRACKING - BOTH LOWER AND UPPER SIDE OF WELD

NOTE: The crack depth and circumferential length were measured during UT examination. The crack shapes shown here are schematic and do not represent the actual crack morphology.

**Figure 5-11 Oyster Creek H4 Weld Circumferential Cracking Map Showing Deepest Detected Flaws as a Function of Azimuthal Angle (UT indications are shown as shaded areas)**



# Stress Distribution for Oyster Creek OD Cracking Analysis

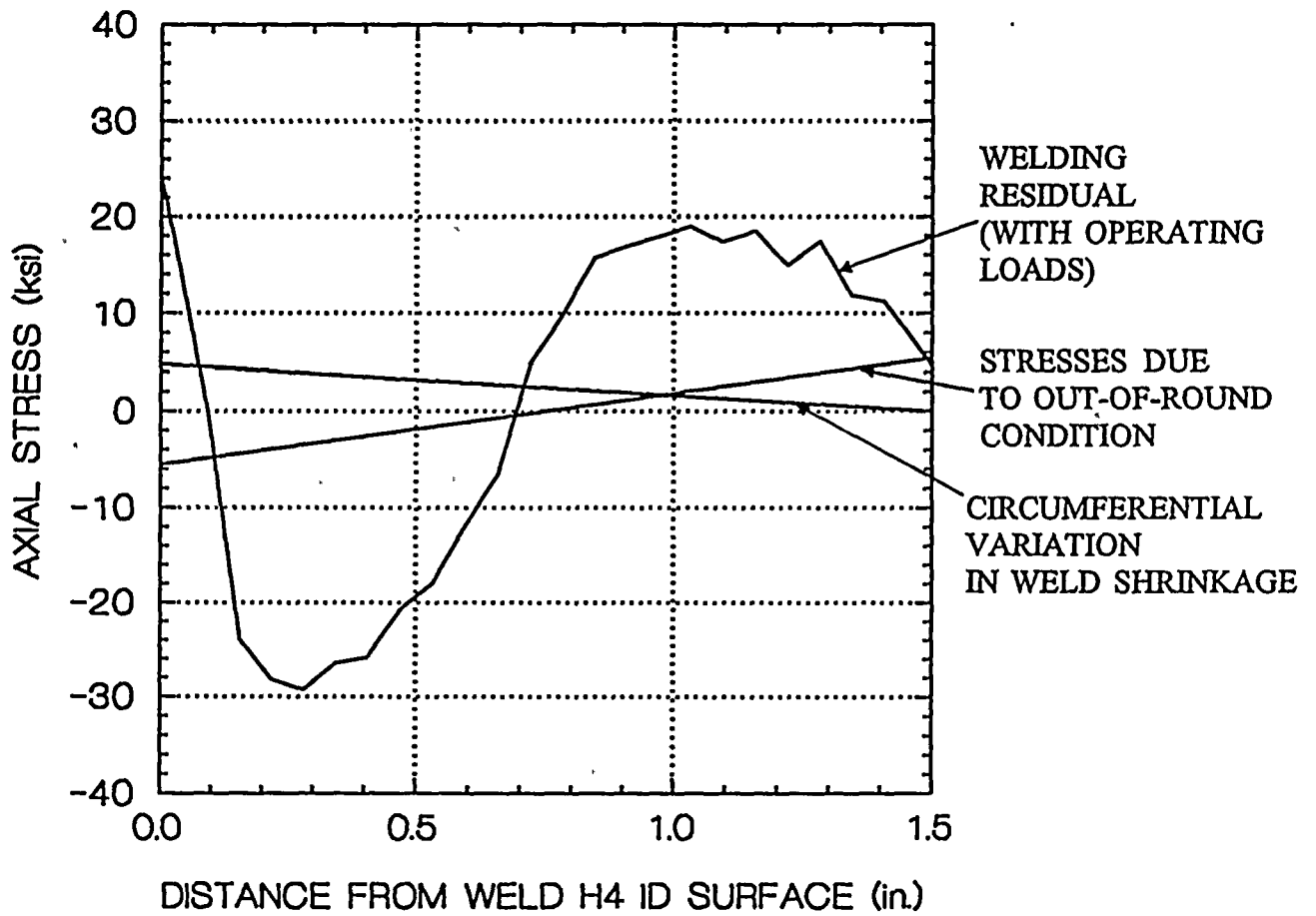


Figure 5-12 Welding Residual Stress Field (With Operating Loads) and Best Estimate Weld Variation and Out-of-Round Induced Stresses for Oyster Creek Crack OD Growth Analysis



## Stress Distribution for NMP-1 Bounding Analysis

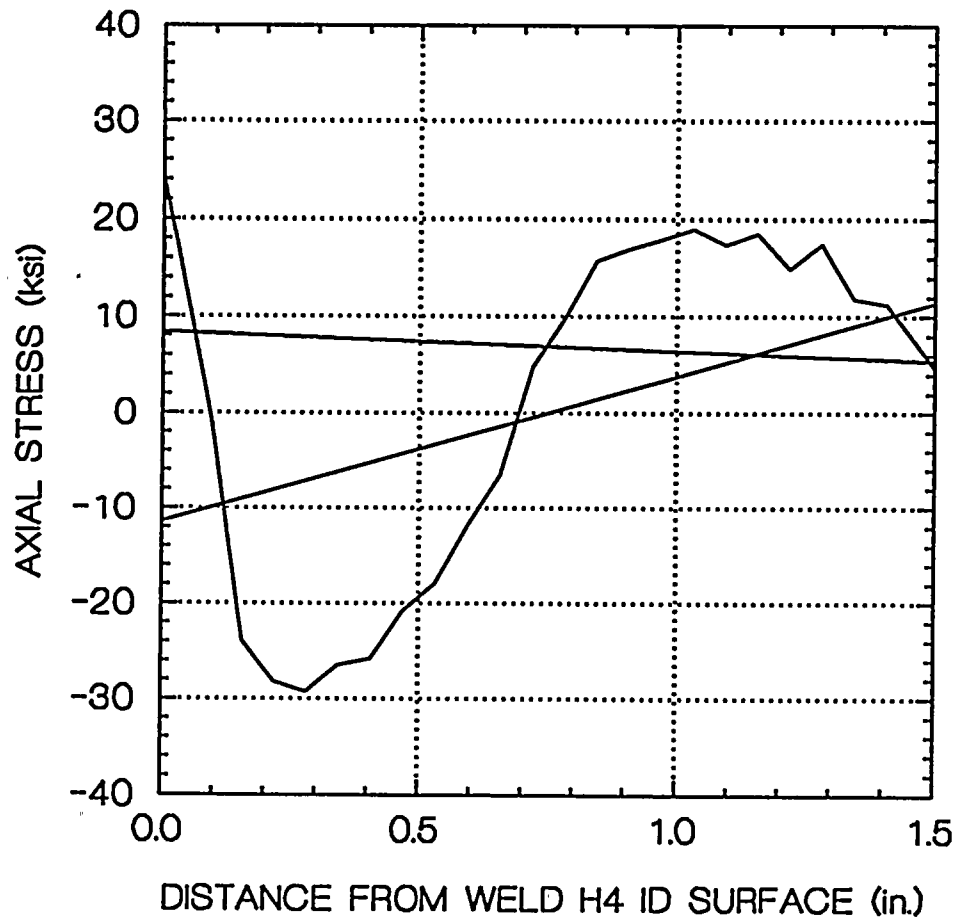


Figure 5-13 Stress Distributions Used for NMP-1 Bounding OD Crack Growth Simulation



## 6.0 Summary and Conclusions

A fracture mechanics assessment of the NMP-1 shroud weld H4 has been performed to determine whether or not throughwall cracking is expected before the end of cycle 11. This assessment included a finite element weld pass simulation to determine the residual stress distribution present after welding. The circumferential variation in the weld HAZ axial stresses was estimated to account for weld starting and stopping, variations in weld groove width, and weld repair. Calculations were also performed to determine the effects of ovality and jacking to correct for out-of-round conditions during welding of the top and bottom cylinders at H4. The calculated stresses were used to determine  $K_I$  which was compared to  $K_{ISCC}$ . Since it is possible that crack initiation has occurred on the ID surface of the H4 weld, crack growth simulations were performed and it was shown that any cracks which initiate on the ID surface of weld H4 will arrest before propagating throughwall.

The applied  $K_I$  at the OD surface of NMP-1 weld H4 is approximately half  $K_{ISCC}$  for a postulated 0.01 in. flaw. Although initiation is unlikely for the fabrication and operating stresses considered in the analysis, it is possible that initiation could have occurred if localized stresses higher than those considered were induced near the HAZ of weld H4, or if a deeper flaw than has been postulated was present after construction. A crack growth calculation has shown that if an OD flaw is initiated, it can grow throughwall in a localized region. However, it has been shown that even if localized throughwall cracking from the OD is conservatively assumed to occur at 16 locations around the circumference, in addition to assuming a 0.4 in. deep 360 degree ID crack, a 41% uncracked area would remain at the end of cycle 11.

In summary, based on the shroud fabrication records, plant operating experience, and the fracture mechanics assessment reported herein, the following conclusions have been made:

- With regard to ID cracking, there is a reasonable probability of SCC crack initiation. However, there is no doubt that an ID initiated crack would arrest before propagating throughwall. This conclusion holds for conservatively postulated stresses and a conservative crack growth model. The welding residual stresses were calculated using a multipass finite element simulation. The root passes were specified in the P. F. Avery weld design and the fabrication records show that the entire ID side of the double-J groove was completed prior to OD side welding. The number of passes after the root pass was calculated from the specified mid-range heat input per pass. Circumferential variations in the axial stresses were also estimated to account for differences in axial weld shrinkage (weld starting/stopping, repairs, variations in weld groove width). In addition, circumferential variations due to out-of-roundness of the cylinders above and below H4 were calculated. Although the surface stresses are high enough to initiate a small defect, the large compressive field just beneath the surface has been shown to arrest a propagating crack.
- The welding procedure which was followed for H4 resulted in low OD surface stresses. The weld passes for the double-J groove at H4 were



completed at the ID first, followed by welding at the OD. The radial weld shrinkage during the final passes results in a substantial lowering of the OD surface stresses. Even when the effects of circumferential variation in weld shrinkage and ovality are conservatively included in the calculation, the stress intensity is less than one-half of  $K_{ISCC}$  for a postulated 0.010 in. flaw. Since a dye penetrant inspection was performed, the postulated 0.010 in. flaw is considered to be an upper bound. Therefore, crack initiation along most of the OD surface of H4 is considered unlikely. The possibility of OD initiation in localized regions due to very localized high stresses and/or where there were undetected deep initial surface flaws must be considered in light of recent inspection results.

- Although initiation along most of the OD surface is unlikely, the possibility of some localized crack initiation and propagation cannot be ruled out. Therefore, crack growth simulations were performed to assess the impact of OD initiated cracks. These calculations showed small crack depths (~0.03 in.) at the end of cycle 11 when only the weld residual stresses and operating stresses were applied. Postulated flaw lengths of up to 0.01 in. were considered in the calculations.

There is a probability of localized throughwall cracking when the circumferential variation and out-of-round stresses are added to the welding residual and operating stresses. For the case where an elliptical surface crack with small surface length (L) to depth (a) ratio is used in the crack growth simulation ( $L/a=2$ ), the postulated OD flaw requires a full 11 fuel cycles to grow throughwall (assuming an arrested ID crack of 0.4 in. deep opposite the OD flaw). However, for an L/a ratio of 5, localized throughwall penetration results after about 35,000 hours of hot operation, thus allowing time for circumferential crack growth to occur. In order to characterize the effects of localized throughwall penetration, a model was developed to conservatively account for the circumferential crack propagation which would follow radial throughwall cracking. The model, which includes a 0.4 in. deep 360 degree ID crack, conservatively shows that 41% of the section would remain uncracked at the end of cycle 11.

- Analysis of plant-specific neutron data has shown that IASCC is not a significant concern (through the end of cycle 11) for the non-sensitized regions of the NMP-1 shroud near weld H4 since the fluences at the shroud in the beltline region will not exceed the GE defined IASCC threshold over large azimuthal regions. Even if IASCC initiation were to occur after ~10 EFPY (incubation dose), there would not be significant crack extension through the end of cycle 11. With regard to neutron damage effects in sensitized material at fluences between  $1 \times 10^{19}$  n/cm<sup>2</sup>/sec and  $3 \times 10^{20}$  n/cm<sup>2</sup>/sec, the EPR is expected to rise to ~18 C/cm<sup>2</sup> from the estimated unirradiated value of 15 C/cm<sup>2</sup>. This effect, which is small, has been accounted for through the use of plant-specific crack growth rate data.



Based on the shroud fabrication records, plant operating experience, and the fracture mechanics assessment of weld H4 reported herein, MPM Research & Consulting has concluded that there are adequate margins of safety through the end of cycle 11 to ensure continued safe operation at NMP-1.



## 7.0 References

- [Aero] Aerospace Metals Handbook, 1991 Edition.
- [ALT3D] ALT3D, Version 2.0, Software for the Analysis of Cracks in Complex 3D Geometries Using the Finite Element Alternating Method, Computational Mechanics, Inc., 1994.
- [Bat84] Battelle Computer Output Listing Entitled, "DOT Run for Nine Mile Point 300 Degree Capsule", May 16, 1984.
- [Be93] A. Bertuch, et al., "Modelling the Corrosion Behaviors of the Heat Transport Circuits of Light Water Nuclear Reactors", Sixth International Symposium on Environmental Degradation in Nuclear Power Systems, August, 1993.
- [Ca94] T.A. Caine, H.S. Mehta, "BWR Core Shroud Inspection and Flaw Evaluation Guidelines", Report No. GENE-523-113-0894, prepared for the BWR Vessel and Internals Project Assessment Subcommittee, September, 1994.
- [EP1743] "Effect of Weld Parameters on Residual Stresses in BWR Piping Systems", Report Prepared by Battelle Columbus Laboratories, EPRI NP-1743-, March, 1981.
- [EPRI89] C.P. Ruiz, et al., "Modelling Hydrogen Water Chemistry for BWR Applications", EPRI Report NP-6386, 1989.
- [ESEERCO88] GE Nuclear Energy, "In-Reactor Stress Corrosion Monitor Prototype Development, Installation, and Operation", Final Report to ESEERCO, Research Report E85-37, February, 1988).
- [GE771] Shroud Fabrication and Operational History Data, Nine Mile Point 1, GE Nuclear Energy Report, GENE 771-28-0494, June, 1994.
- [GE94] M.L. Herrera, G. Eckert, A. Baker., B. Gordon, "BWR Core Shroud Evaluation", Report No. GE-NE-523-148-1193, prepared for the BWR Owners' Group, April, 1994.
- [GENE523] B.J. Branlund and B.M. Gordon, "Structural Evaluation and Justification of the Nine Mile Point 1 Core Shroud for Continued Operation", GE Nuclear Energy Report No. GENE-523-A161-1094.



- [Go90] G.M. Gordon and K.S. Brown, "Dependence of Creviced BWR Component IGSCC Behavior on Coolant Chemistry", in Proceedings of the 4th International Conference of Environmental Degradation of Materials in Nuclear Power Systems--Water Reactors, National Association of Corrosion Engineers, 1990, p. 14-46 to 14-62.
- [In94] Private Communication From G. Inch to M. Manahan, "NMP-1 Core Axial Power Distribution", October 20, 1994.
- [Int] "Mechanical and Physical Properties of the Austenitic Chromium-Nickel Stainless Steels at Elevated Temperatures", Section I, Bulletin B, Chromium Nickel Stainless Steel Data, The International Nickel Company, Inc.
- [IRW57] G.R. Irwin, "Analysis of Stresses and Strains Near the End of a Crack Traversing a Plate", Journal of Applied Mechanics, 24, pp. 361-364, 1957.
- [Ja86] A.J. Jacobs, D.A. Hale, and M. Siegler, Unpublished Data, GE Nuclear Energy, San Jose, CA, January, 1986.
- [Ma85] M.P. Manahan, L.M. Lowry, M.P. Landow, et al., "Examination, Testing, and Evaluation of Specimens From the 210-Degree Irradiated Pressure Vessel Surveillance Capsule for the Oyster Creek Nuclear Generating Station", Final Report to GPU Nuclear, August 30, 1985.
- [Ma94] M.P. Manahan, Sr., D.D. Macdonald, A.J. Peterson, Jr., "Determination of the Fate of the Current in the Stress-Corrosion Cracking of Sensitized Type 304 SS in High Temperature Aqueous Systems", Corrosion Science, October, 1994.
- [NRC94] NRC Generic Letter 94-03, "Intergranular Stress Corrosion Cracking of Core Shrouds in Boiling Water Reactors,"
- [NUREG0313] "Technical Report on Material Selection and Processing Guidelines for BWR Coolant Pressure Boundary Piping", U.S. Nuclear Regulatory Commission, NUREG-0313, Rev. 2, January, 1988.
- [PCCRACK] "pc-CRACK: Fracture Mechanics Software for Personal Computers", Version 2.1, Structural Integrity Associates, Inc., 1991.
- [RYB81] E.F. Rybicki, R.B. Stonesifer, R.J. Olson, "Stress Intensity Factors Due to Residual Stresses in Thin-Walled Girth-Welded Pipes", Journal of Pressure Vessel Technology, 103, pp. 66-75, 1981.
- [Sp81] M. Speidel, Metallurgical Transactions, Vol. 12A, p. 779 (1981).



[St84]

D. Stahl, M.P. Manahan, et al., "Examination, Testing and Evaluation of Irradiated Pressure Vessel Surveillance Specimens From the Nine Mile Point Nuclear Power Station", Final Report No. BCL-585-84-6 to Niagara Mohawk Power Corporation, July 18, 1984.

[Te94]

Letter from C.D. Terry to U.S. NRC regarding Nine Mile Point Unit 1 Docket No. 50-220, DPR-63, "Response to Generic Letter 94-03," Intergranular Stress Corrosion Cracking of Core Shrouds in Boiling Water Reactors, August 23, 1994.

[TPI73]

H. Tada, P.C. Paris, G.R. Irwin, "The Stress Analysis of Cracks Handbook", Del Research Corporation, Hellertown, PA, 1973.

[Wa94]

Letter From S. Wang (GE) to K. Kotak, "Estimated Fast Neutron Fluence at Nine Mile Point 1 Shroud Welds", GENE 771-28-0494, Revision 0, June 28, 1994.

[WEL3]

"WELD3 Version 2.2", Computer Software for Incremental, Thermal, Elastic-Plastic Finite Element Analysis, Computational Mechanics, Inc., 1992.

[WELV]

"WELD3 Verification Manual, Version 2.2", Computational Mechanics, Inc., 1992.



## 8.0 Nomenclature

H4	Shroud Girth Weld Joining the Upper and Central Mid Cylinders
2D	Two-Dimensional
3D	Three-Dimensional
a	Crack Length
BWR	Boiling Water Reactor
BWROG	BWR Owners Group
C(T)	Compact Type Specimen
CTE	Coefficient of Thermal Expansion
DCB	Double Cantilever Beam
DOS	Degree of Sensitization
DOT	Discrete Ordinates Transport
ECP	Electrochemical Corrosion Potential
EPFY	Effective Full Power Years
EPR	Electrochemical Potentiokinematic Reactivation
EPRI	Electric Power Research Institute
FEM	Finite Element Method
$G_I$	Mode I Energy Release Rate
$G_{II}$	Mode II Energy Release Rate
GE	General Electric
GPUNC	GPU Nuclear Corporation
HAZ	Heat Affected Zone
IASCC	Irradiation Assisted Stress Corrosion Cracking
ID	Inner Diameter
IGSCC	Intergranular Stress Corrosion Cracking
$K_I$	Mode I Stress Intensity Factor
$K_{II}$	Mode II Stress Intensity Factor
$K_{ISCC}$	SCC Threshold Stress Intensity Factor
LEFM	Linear Elastic Fracture Mechanics
LPRM	Local Power Range Monitor
NMP-1	Nine Mile Point Unit 1
NMPC	Niagara Mohawk Power Corporation
NRC	Nuclear Regulatory Commission
OD	Outer Diameter
PTFE	Polytetrafluoroethylene
R/t	Radius to Thickness Ratio





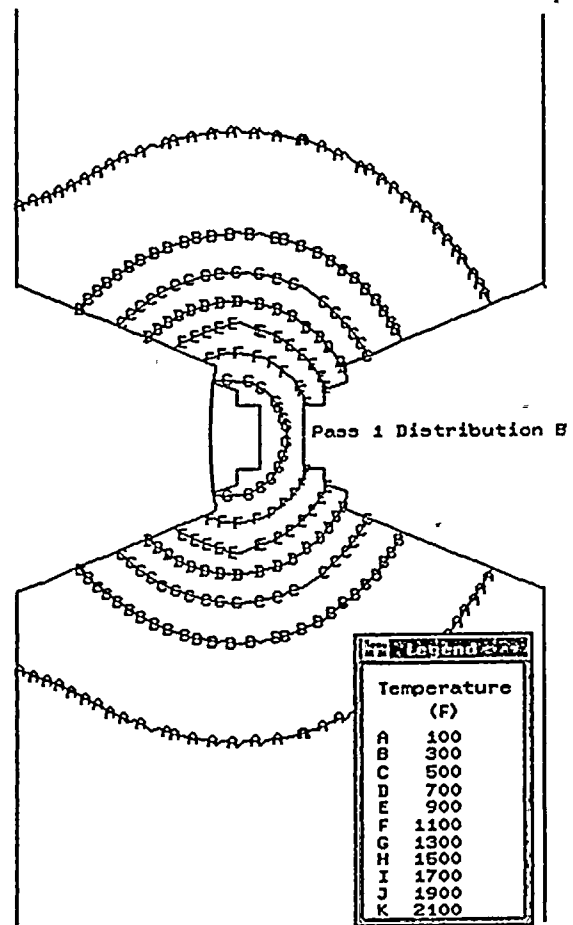
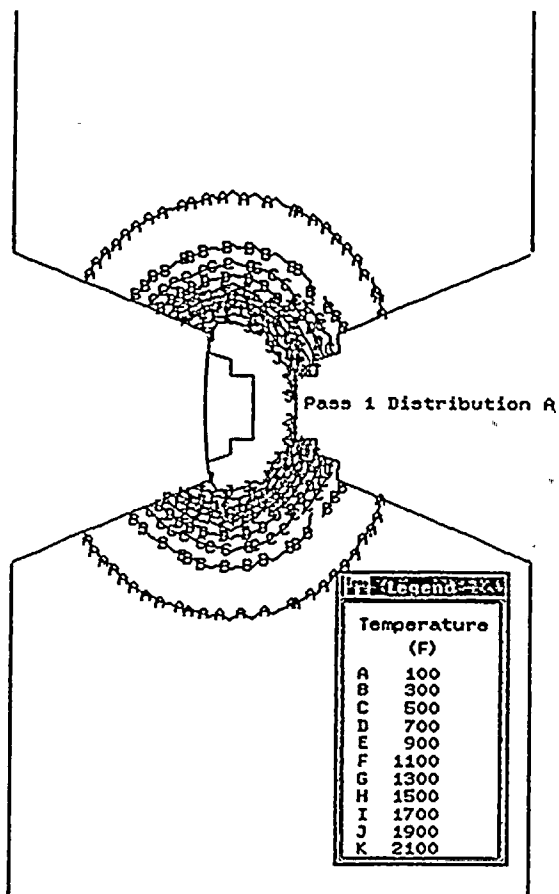
SCC	Stress Corrosion Cracking
SEC	Single Edge Crack
SS	Stainless Steel
ZRA	Zero Resistance Ammeter



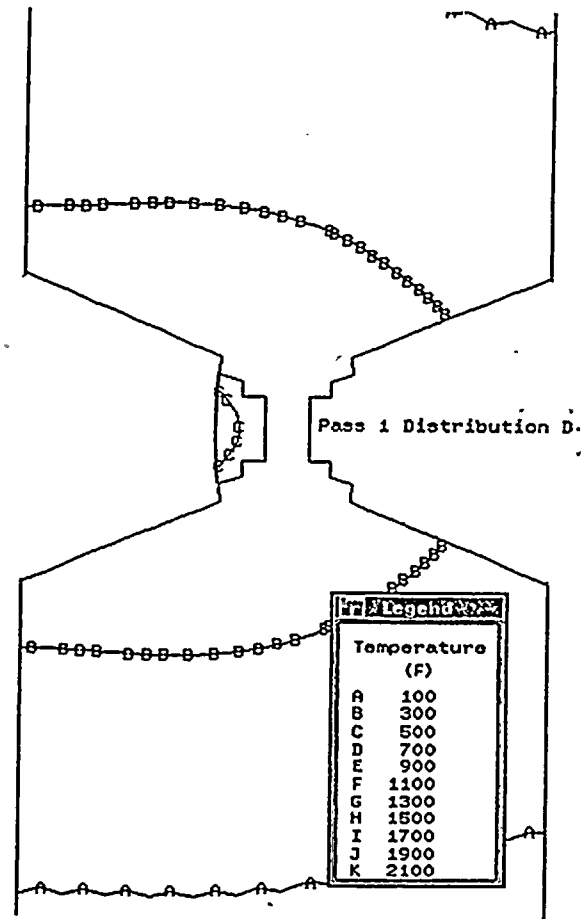
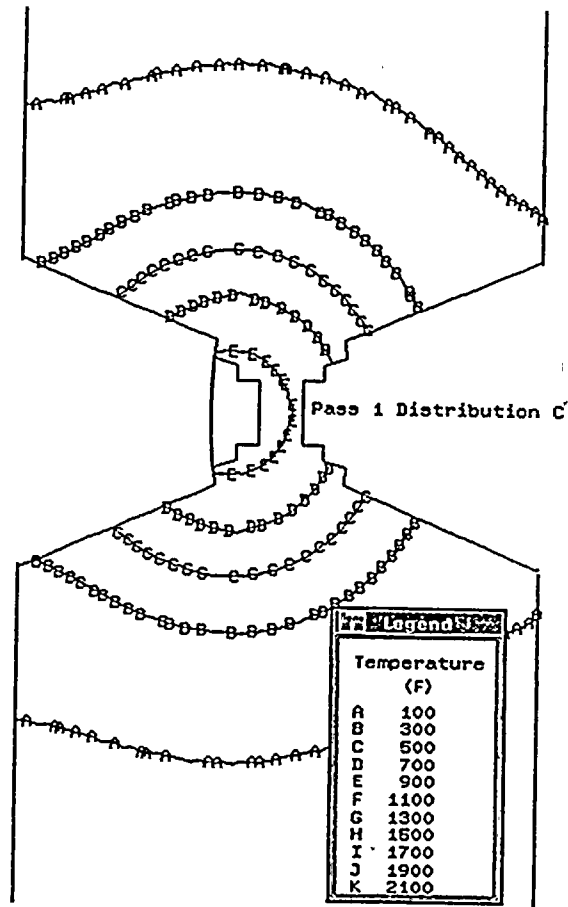
Appendix A

**Example Isotherm Plots**

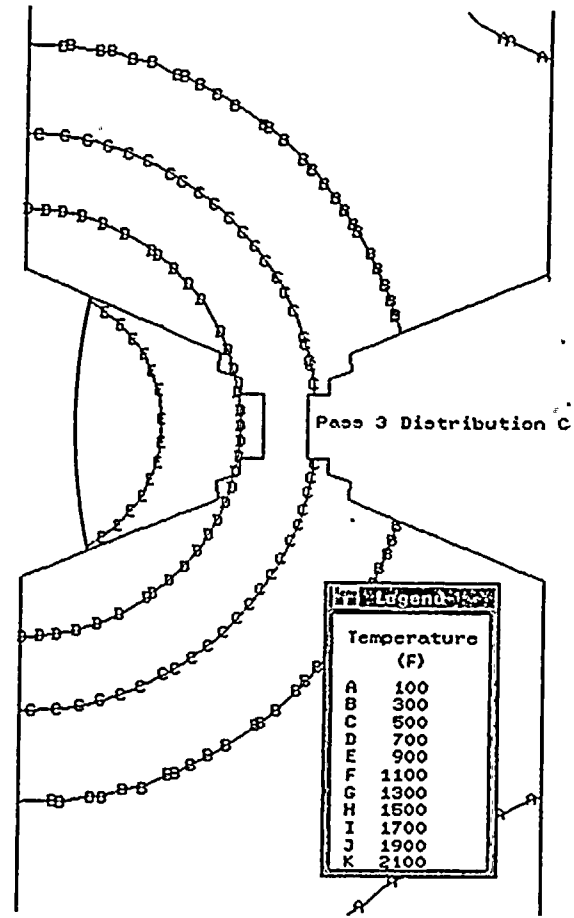
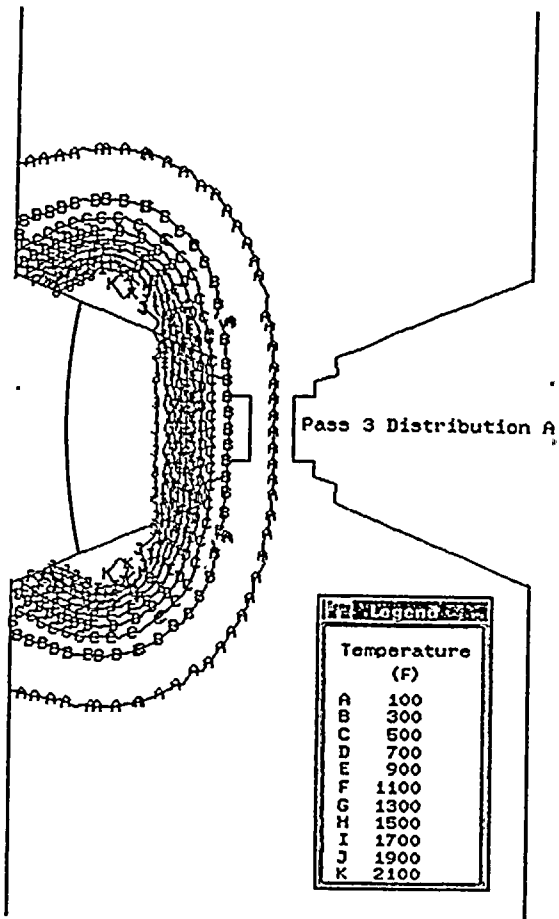




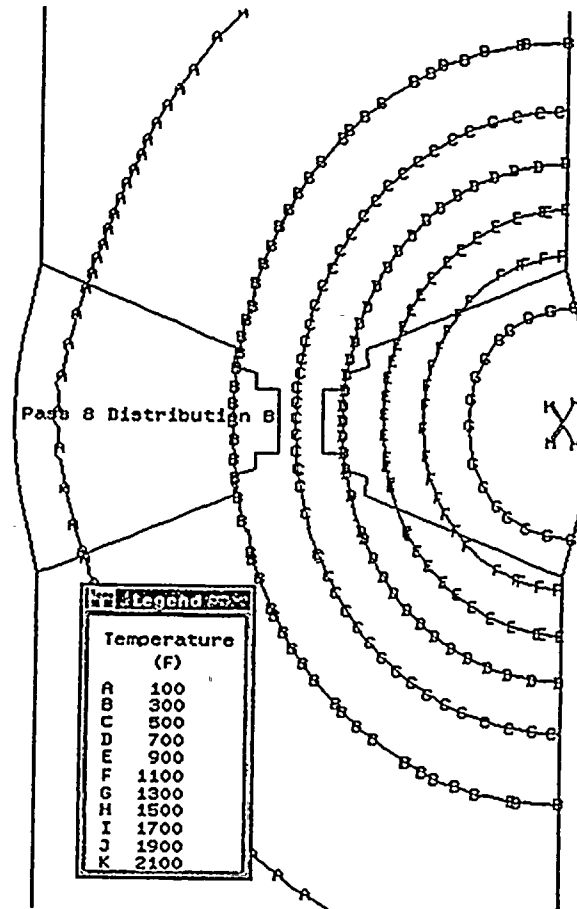
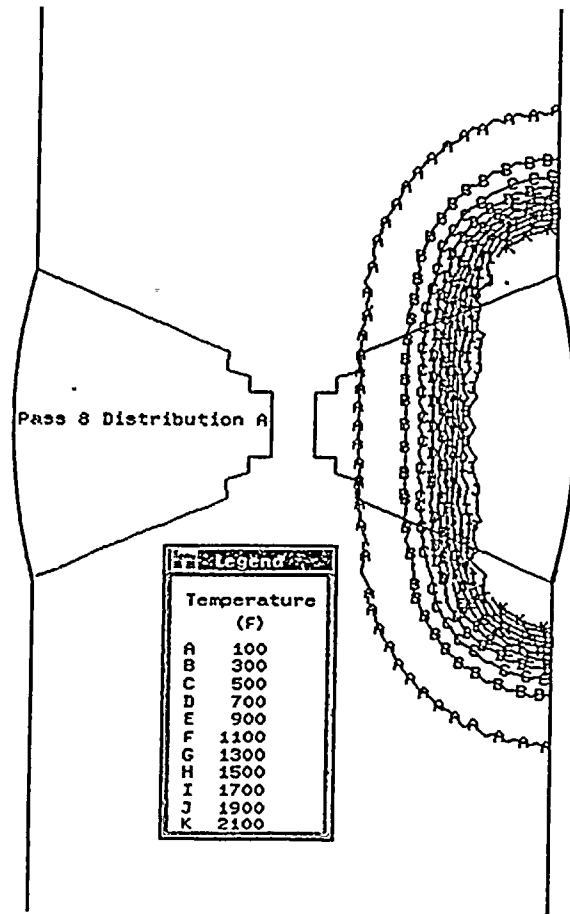














**ATTACHMENT 3**

**NINE MILE POINT UNIT 1  
DOCKET NO. 50-220  
LICENSE NO. DPR-63**

**GENERIC LETTER 94-03  
SUPPLEMENTAL INFORMATION**

**SPECIAL OPERATING PROCEDURE  
N1-SOP-2, "UNEXPLAINED REACTOR  
POWER CHANGE," REVISION 5**

SECRET

SECRET

NIAGARA MOHAWK POWER CORPORATION  
NINE MILE POINT NUCLEAR STATION UNIT 1  
SPECIAL OPERATING PROCEDURE

N1-SOP-2

REVISION 05

UNEXPLAINED REACTOR POWER CHANGE

TECHNICAL SPECIFICATION REQUIRED

Approved By:  
N. L. Rademacher

\_\_\_\_\_  
Manager Operations - Unit 1

\_\_\_\_\_  
Date

FOR INFO. ONLY

Effective Date: \_\_\_\_\_

PERIODIC REVIEW DUE DATE \_\_\_\_\_



LIST OF EFFECTIVE PAGES

Page No.   Change No.

Page No.   Change No.

Page No.   Change No.



SPECIAL OPERATING PROCEDURE

PROCEDURE NO. N1-SOP-2

UNEXPLAINED REACTOR POWER CHANGE

A. EVENT DESCRIPTION

Unexplained change in Reactor Power as indicated by ANY of the following:

- Power oscillations OR periodic LPRM upscale / downscale alarms. (periodic - constant frequency)
- Unexplained change of more than 2% (35-40 MWth) Reactor Power.
- Inadvertant entry into "RESTRICTED ZONE" (see Figure 2.1, Page 6)
- Power fails to increase as expected with a increase in Recirc flow.

B. OPERATOR ACTIONS

Perform actions in accordance with SOP-2 Flowchart starting on page 2.



# N1-SOP-2 UNEXPLAINED REACTOR POWER CHANGE

## EVENT DESCRIPTION

Unexplained change in Reactor Power as indicated by ANY of the following:

- Power oscillations OR periodic LPRM upscale / downscale alarms. (periodic - constant frequency)
- Unexplained change of more than 2% ( 35-40 MWth) Reactor Power
- Inadvertent entry into "RESTRICTED ZONE" (see Figure 2.1, Page 6)
- Power fails to increase as expected with a increase in recirc flow

↓

Activate Emergency Plan, if required, in accordance with EPIP-EPP-18.

↓

Continuously monitor LPRMs and APRMs for thermal hydraulic instability, as indicated by ANY of the following:

- Power oscillations (APRM chart recorders or meters)
- Periodic LPRM upscale alarms.
- Periodic LPRM downscale alarms WITH local flux oscillations.

↓

**CAUTIONS:** 1. Entry into the Restricted Zone may cause Reactor Power oscillations.  
2. Starting a Recirc. pump to increase recirculation flow is prohibited.

### While executing the following steps:

IF	THEN
1. "RESTRICTED ZONE" is entered,	a. Exit "RESTRICTED ZONE" by performing one of the following: <ul style="list-style-type: none"> <li>• IF.... Recirculation pumps are operating, AND.... plant conditions permit, THEN.... increase Recirc. Pump speed to increase recirc. flow</li> <li style="text-align: center;">OR</li> <li>• Lower Reactor Power by inserting "CRAM" rods per N1-OP-43A, Reactivity Control.</li> </ul> b. Inform Reactor Engineering Supervisor
2. Thermal hydraulic instability is detected, OR Scram Zone entered, OR NO Recirc pumps running,	Manually scram the reactor AND enter SOP-1.

↓

Unexplained Rx Power Change continued page 3.



Unexplained Rx Power Change continued .

While executing the following steps:	
IF	THEN
1. "RESTRICTED ZONE" is entered,	Perform Override on page 2.
2. Thermal hydraulic instability is detected, OR Scram Zone entered, OR NO Recirc pumps running,	

IF	THEN
Loss of FW heating has occurred, which causes a decrease in FW temp. entering the reactor,	Enter N1-OP-16, Sec. H (Loss of FW Htrs), and execute concurrently.
Loss of feedwater heating is greater than 100°F,	Scram the Reactor, enter SOP-1 and execute concurrently.

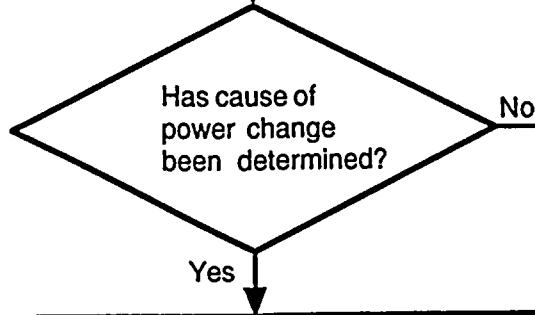
Observe the following parameters to determine cause of power change:

PARAMETERS	IF	THEN
Control Rod Position	Control Rod out of position	Enter N1-OP-5, Sec H (Mispositioned Control Rod), and execute concurrently.
Recirculation Flow	Recirc. flow malfunction ( change in total / individual pump flow)	Enter N1-OP-1, Sec H, and execute concurrently.
Reactor Pressure	Pressure changes or oscillations observed	Check for misoperation of: <ul style="list-style-type: none"> <li>• turbine control valves</li> <li>• turbine bypass valves</li> <li>• verify stable recirc flow</li> </ul> <ul style="list-style-type: none"> <li>• EPR or MPR</li> <li>• ERV(s)</li> </ul>
Steam Flow	Steam flow changes observed,	Check for changes in: <ul style="list-style-type: none"> <li>• Total stm flow vs. turbine stm flow</li> <li>• Mismatch stm flow vs. feedwater flow</li> </ul>
Turbine-Generator Load	Turbine-Generator load has changed,	Check: <ul style="list-style-type: none"> <li>• Condenser vacuum</li> <li>• Control valve position</li> <li>• Bypass valve position</li> <li>• Circ. Wtr inlet temperature</li> </ul> <ul style="list-style-type: none"> <li>• EPR / MPR</li> <li>• Feedwater heating</li> <li>• Reheater parameters</li> </ul>
Feedwater Flow	Feedwater flow changes observed,	Check: <ul style="list-style-type: none"> <li>• FW flow vs. STM flow</li> <li>• Control or Bypass valves</li> </ul> <ul style="list-style-type: none"> <li>• FW FCV position</li> <li>• Primarysys leak</li> </ul>

Unexplained Rx Power Change continued page 4.



Unexplained Rx Power Change continued .



Depending on plant response or conditions discovered,  
Perform appropriate procedure OFF NORMALS and  
Annunciator Responses.

Contact Reactor Engineering for assistance.

Suspend ANY planned power changes.

**NOTE:** Indications of Shroud cracking OR displacement will vary depending on location and severity of crack..

Determine if any of the following parameter changes occurred concurrent with the unexplained power change.

PARAMETERS	Rx Power	Recirc Suc Temp	Rod Line	Total Core Flow	Core d/p
Above top Guide	↓	↑	↓	↑	
Between Top Guide and Core Plate	↓	↑	↓		
Below Core Plate	↓		↓	↑	↓
Minimum detectable	35-40 MWth	>4°F	2%		

Unexplained Rx Power Change continued page 5.



Unexplained Rx Power Change continued .

IF	THEN
Cracking or seperation suspected, at below core plate,	1. Maintrain Rx recirc flow . 2. Scram the reactor. 3. Concurrently: a. Enter N1-SOP-1 b. Slowly reduce Rx Recirc flow.
1. Cracking or seperation suspected, at Above top guide OR between top guide and Core plate  2. Reason for power change can <u>NOT</u> be determined,	Perform the following: 1. Commence Normal Rx S/D per N1-OP-43A. 2. During recirc flow reduction attempt to confirm cracking OR seperation by observing the following: • Rod Line recovery • Above noted abnormal parameter recovering towards normal

END

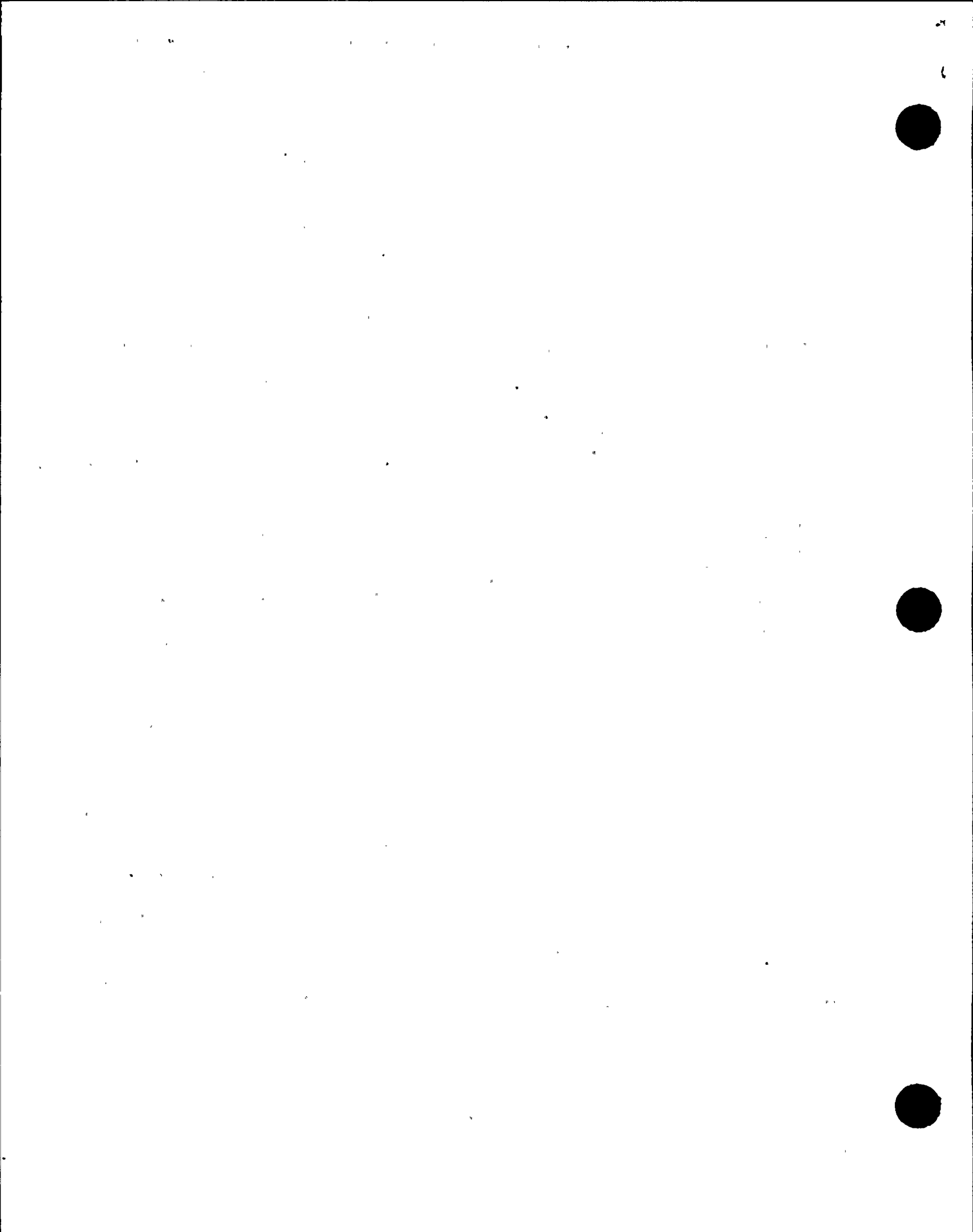
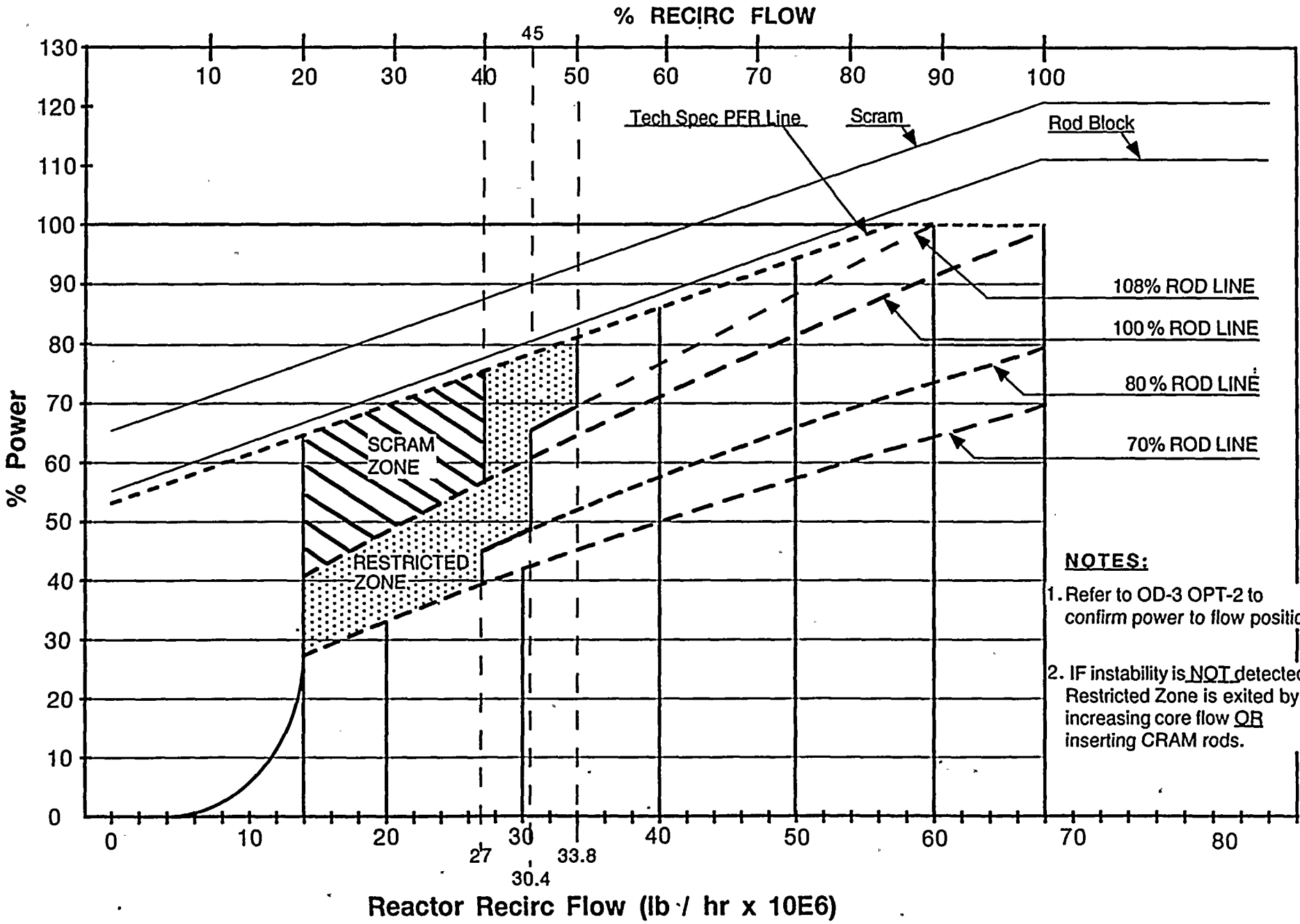


**FIGURE 2.1**  
**POWER FLOW OPERATING MAP**

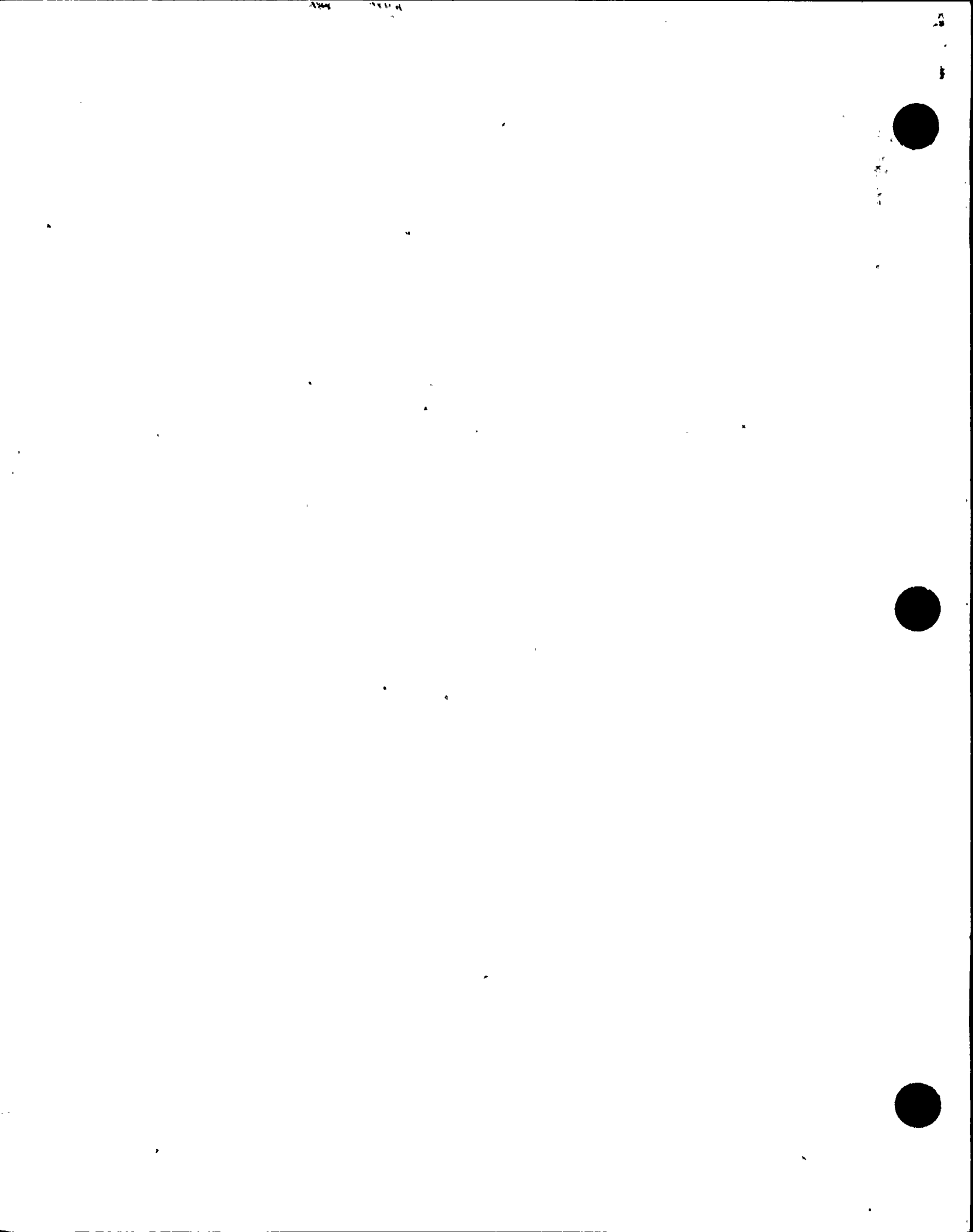


- NOTES:**
1. Refer to OD-3 OPT-2 to confirm power to flow position.
  2. IF instability is NOT detected, Restricted Zone is exited by increasing core flow OR inserting CRAM rods.



B. OPERATOR ACTIONS (Cont)

N1-SOP-2 page 7 is a full size flow chart located at the Control Room Print Table.



# N1-SOP-2 UNEXPLAINED REACTOR POWER CHANGE

## EVENT DESCRIPTION

Unexplained change in Reactor Power as indicated by ANY of the following:

- Power oscillations OR periodic LPRM upscale / downscale alarms. (periodic - constant frequency)
- Unexplained change of more than 2% (35-40 MWth) Reactor Power
- Inadvertent entry into "RESTRICTED ZONE" (see Figure 2.1)
- Power fails to increase as expected with a increase in recirc flow

Activate Emergency Plan, if required, in accordance with EPIP-EPP-18.

Continuously monitor LPRMs and APRMs for thermal hydraulic instability, as indicated by ANY of the following:

- Power oscillations (APRM chart recorders or meters)
- Periodic LPRM upscale alarms.
- Periodic LPRM downscale alarms WITH local flux oscillations.

**CAUTIONS:** 1. Entry into the Restricted Zone may cause Reactor Power oscillations.  
2. Starting a Recirc. pump to increase recirculation flow is prohibited.

While executing the following steps:

IF	THEN
1. "RESTRICTED ZONE" is entered,	a. Exit "RESTRICTED ZONE" by performing one of the following: • IF.... Recirculation pumps are operating, AND.... plant conditions permit, THEN.... increase Recirc. Pump speed to increase recirc. flow OR • Lower Reactor Power by inserting "CRAM" rods per N1-OP-43A, Reactivity Control. b. Inform Reactor Engineering Supervisor
2. Thermal hydraulic instability is detected, OR Scram Zone entered, OR NO Recirc pumps running,	Manually scram the reactor AND enter SOP-1.

IF	THEN
Loss of FW heating has occurred, which causes a decrease in FW temp. entering the reactor,	Enter N1-OP-16, Sec. H (Loss of FW Htrs), and execute concurrently.
Loss of feedwater heating is greater than 100°F,	Scram the Reactor, enter SOP-1 and execute concurrently.

Observe the following parameters to determine cause of power change:

PARAMETERS	IF	THEN
Control Rod Position	Control Rod out of position	Enter N1-OP-5, Sec H (Mispositioned Control Rod), and execute concurrently.
Recirculation Flow	Recirc. flow malfunction (change in total / individual pump flow)	Enter N1-OP-1, Sec H, and execute concurrently.
Reactor Pressure	Pressure changes or oscillations observed	Check for misoperation of: • turbine control valves • EPR or MPR • turbine bypass valves • ERV(s) • verify stable recirc flow
Steam Flow	Steam flow changes observed,	Check for changes in: • Total stm flow vs. turbine stm flow • Mismatch stm flow vs. feedwater flow
Turbine-Generator Load	Turbine-Generator load has changed,	Check: • Condenser vacuum • EPR / MPR • Control valve position • Feedwater heating • Bypass valve position • Reheater parameters • Circ. Wtr inlet temperature
Feedwater Flow	Feedwater flow changes observed,	Check: • FW flow vs. STM flow • FW FCV position • Control or Bypass valves • Primary sys leak

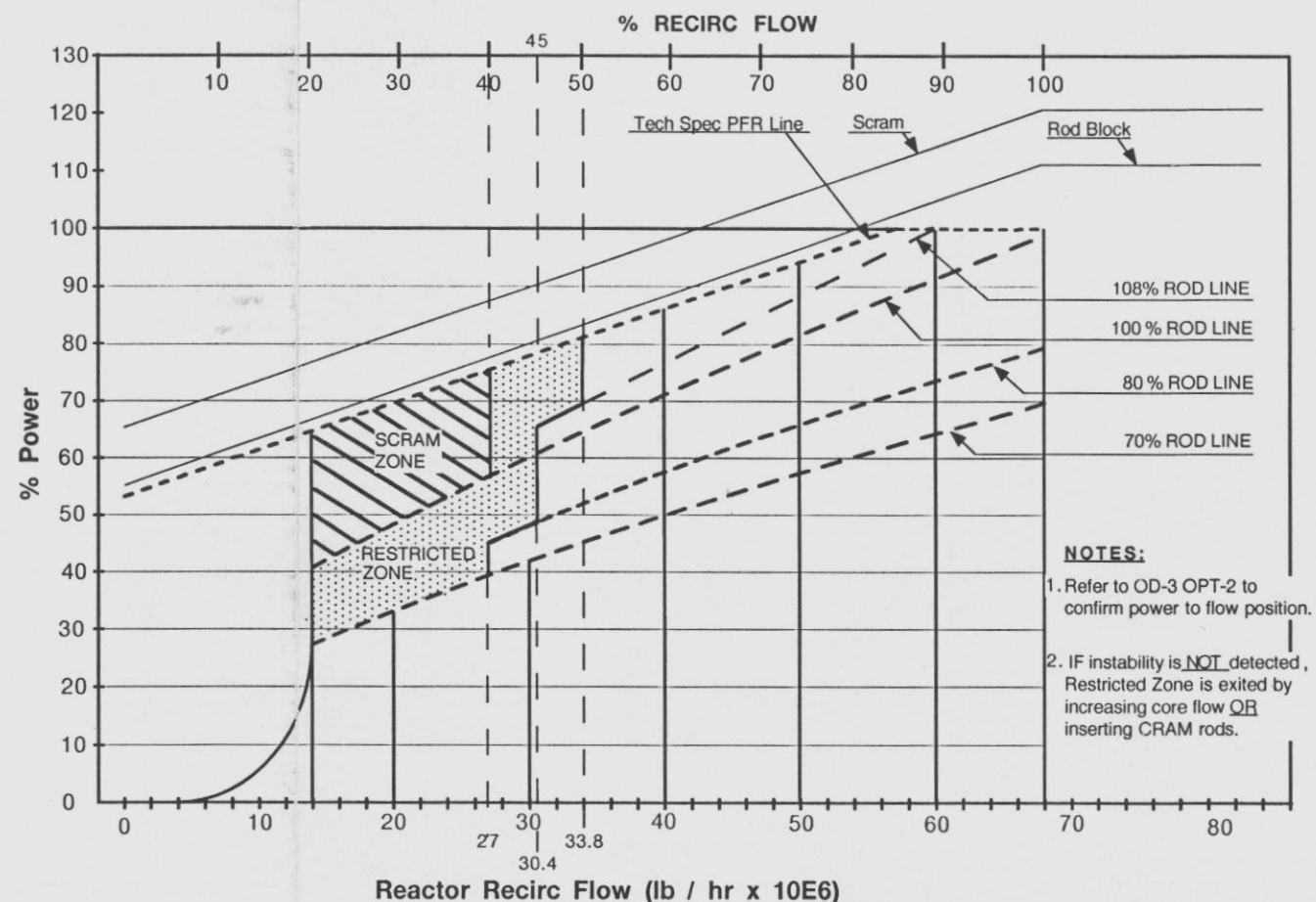
Has cause of power change been determined?

Yes

Depending on plant response or conditions discovered, Perform appropriate procedure OFF NORMALS and Annunciator Responses.

No

**FIGURE 2.1  
POWER FLOW OPERATING MAP**



### NOTES:

1. Refer to OD-3 OPT-2 to confirm power to flow position.
2. IF instability is NOT detected, Restricted Zone is exited by increasing core flow OR inserting CRAM rods.

Contact Reactor Engineering for assistance.

Suspend ANY planned power changes.

**NOTE:** Indications of Shroud cracking OR displacement will vary depending on location and severity of crack..

Determine if any of the following parameter changes occurred concurrent with the unexplained power change.

PARAMETERS	Rx Power	Recirc Suc Temp	Rod Line	Total Recirc. d/p	Core
Above top Guide	↓	↑	↓	↑	
Between Top Guide and Core Plate	↓	↑	↓		
Below Core Plate	↓		↓	↑	↓
Minimum detectable	35-40 MWth	>4°F	2%		

IF	THEN
Cracking or separation suspected, at below core plate,	1. Maintrain Rx recirc flow. 2. Scram the reactor. 3. Concurrently: a. Enter N1-SOP-1 b. Slowly reduce Rx Recirc flow.
1. Cracking or separation suspected, at Above top guide OR between top guide and Core plate 2. Reason for power change can NOT be determined,	Perform the following: 1. Commence Normal Rx S/D per N1-OP-43A. 2. During recirc flow reduction attempt to confirm cracking OR separation by observing the following: • Rod Line recovery • Above noted abnormal parameter recovering towards normal

ANSTEC  
APERTURE  
CARD

INFORMATION  
ONLY

NIAGARA MOHAWK POWER CORPORATION  
NINE MILE POINT NUCLEAR STATION UNIT 1  
SPECIAL OPERATING PROCEDURE

Procedure Number

N1-SOP-2

Page 7

Rev 05

9411160244-01

50-220  
9411160218  
11/4/94

C